

PRECISE MEASUREMENT OF DIMUON PRODUCTION CROSS-SECTIONS IN  $\nu_\mu\text{Fe}$   
AND  $\bar{\nu}_\mu\text{Fe}$  DEEP INELASTIC SCATTERING AT THE TEVATRON

BY

MAXIM T. GONCHAROV

B.S., MOSCOW INSTITUTE OF PHYSICS AND TECHNOLOGY, 1993

---

A DISSERTATION

SUBMITTED IN PARTIAL FULFILLMENT OF THE

REQUIREMENTS FOR THE DEGREE

DOCTOR OF PHILOSOPHY

DEPARTMENT OF PHYSICS

COLLEGE OF ARTS AND SCIENCES

KANSAS STATE UNIVERSITY

MANHATTAN, KANSAS

2001

Approved By:

Major Professor

Tim A. Bolton

# ABSTRACT

This dissertation presents the measurement of the semi-inclusive cross-sections for  $\nu_\mu$  and  $\bar{\nu}_\mu$ -nucleon deep inelastic scattering interactions with two oppositely charged muons in the final state. These events dominantly arise from production of a charm quark during the scattering process. The measurement is obtained from the analysis of 5102  $\nu_\mu$  induced and 1458  $\bar{\nu}_\mu$  induced events collected with the NuTeV detector exposed to a sign selected beam at the Fermilab Tevatron. A leading-order QCD analysis is used to predict charm production cross-section parameters such as the charm mass  $m_c$ , strange and anti-strange sea quark probability distribution functions  $s(x, q^2)$ , semi-leptonic charm decay branching ratio  $B_c$ , and charm fragmentation function parameter  $\epsilon$ . The result is presented as a nearly model-independent dimuon production cross-section table. I also extract cross-section measurements from a re-analysis of 5030  $\nu_\mu$  induced and 1060  $\bar{\nu}_\mu$  induced events collected from the exposure of the same detector to a quad-triplet beam by the CCFR experiment. The resulting cross-section tables are the most statistically precise measurements of neutrino-induced dimuon production cross-sections to date. These measurements should be of broad use to phenomenologists interested in the dynamics of charm production, the strangeness content of the nucleon, and the CKM matrix element  $V_{cd}$ .

# Contents

<b>List of Figures</b>	<b>iv</b>
<b>List of Tables</b>	<b>xi</b>
<b>1 Introduction</b>	<b>1</b>
1.1 Standard Model . . . . .	2
1.2 Asymptotic Freedom . . . . .	5
1.3 Deep Inelastic Scattering . . . . .	6
1.4 Dimuon production . . . . .	8
<b>2 Neutrino-Nucleon Scattering and Charm Production</b>	<b>11</b>
2.1 Charged Current Kinematics . . . . .	12
2.2 Charged-Current Cross Section . . . . .	14
2.3 The Parton Model . . . . .	15
2.4 Neutrino Scattering off a Real Target . . . . .	17
2.5 LO QCD Charm Production . . . . .	18
2.6 Next-to-Leading Order Charm Production . . . . .	19

<b>3</b>	<b>E815 Experimental Apparatus</b>	<b>21</b>
3.1	The Sign Selected Neutrino Beam . . . . .	21
3.2	Lab E Detector . . . . .	22
3.3	Calibration Beam . . . . .	25
<b>4</b>	<b>The Dimuon Data Sample</b>	<b>30</b>
4.1	Charged-current Data Selection . . . . .	30
4.2	Dimuon Data Selection . . . . .	31
<b>5</b>	<b>Monte Carlo Simulation</b>	<b>35</b>
5.1	Detector Simulation . . . . .	36
5.2	Neutrino Flux and Normalization . . . . .	43
<b>6</b>	<b>Dimuon Analysis Results</b>	<b>46</b>
6.1	General Fit Procedure . . . . .	46
6.2	NuTeV Leading Order QCD fits . . . . .	50
6.3	Systematic Errors . . . . .	51
6.4	Leading Order Fits To CCFR Data . . . . .	59
6.5	$V_{cd}$ Matrix Element . . . . .	61
6.6	The high $x$ region . . . . .	62
<b>7</b>	<b>Dimuon Cross-Section Tables</b>	<b>77</b>
7.1	Dimuon Cross-Section . . . . .	78
7.2	Data Unfolding . . . . .	79

7.3	Using The Table . . . . .	83
7.4	Validation of Cross Section Tables . . . . .	86
<b>8</b>	<b>Summary</b>	<b>93</b>
<b>A</b>	<b>Cross Section Tables</b>	<b>95</b>

# List of Figures

1.1	Gluon screening. . . . .	5
1.2	CC diagram $\nu\mu(\bar{\nu}_\mu)N \rightarrow \mu^-(\mu^+)X$ . . . . .	7
1.3	Typical CC event . . . . .	8
1.4	CC charm production $\nu\mu(\bar{\nu}_\mu)N \rightarrow \mu^-(\mu^+)X$ . . . . .	8
1.5	Typical dimuon event . . . . .	9
2.1	Kinematics of Neutrino Nucleon Scattering. . . . .	12
2.2	LO and NLO Feynmann diagrams. . . . .	20
3.1	The Fermilab Tevatron and neutrino-beamline. . . . .	26
3.2	The SSQT beamline. . . . .	27
3.3	Schematic diagram of beam timing structure . . . . .	27
3.4	The Lab E detector. . . . .	27
3.5	The NuTeV Testbeam spectrometer. . . . .	28
4.1	Total reconstruction efficiency as a function of second muon gener- ated energy. . . . .	34

5.1	Radiative correction diagrams. A) Boson loop correction. B) Boson radiation from final state quark. C) Box diagram. . . . .	36
5.2	The <i>Mean</i> (left) and the <i>Width</i> (right) of Gaussian fits (Fig.5.5) as functions of the generated hadron energy both for the test beam and Monte Carlo. The darker curves represent the test beam. . . .	38
5.3	The <i>Mean</i> (left) and the <i>Width</i> (right) of Gaussian fits (Fig.5.5) as functions of the generated muon energy both for the test beam and Monte Carlo. The darker curves represent the test beam. . . . .	38
5.4	<i>Mean</i> and <i>Width</i> distributions from Fig.5.3 after corrections. . . .	39
5.5	Gaussian fits to the reconstructed ( $E_{rec}$ ) energy over generated ( $E_{gen}$ ) energy distribution for one of the hadron TB and MC runs. . . . .	40
5.6	Unnormalized probability of the event as a function of the ratio of electromagnetic part to the total shower energy. Crosses - $3\pi$ model, pluses - LUND prediction. . . . .	42
5.7	Top - total muon energy of the primary and secondary muons. Middle - muon energies at the front face of the toroid. Bottom - hadronic energy. $\nu$ mode is on the left, $\bar{\nu}$ mode is on the right. $\chi^2$ per total number of degrees freedom is listed for each distribution. Pluses are data, histograms - Monte Carlo . . . . .	44
5.8	Top - visible neutrino energy. Middle - vertex distribution in x transverse plane. Bottom - vertex distributions in y transverse plane. $\nu$ mode is on the left, $\bar{\nu}$ mode is on the right. $\chi^2$ per total number of degrees freedom is listed for each distribution. Pluses are data, histograms - Monte Carlo . . . . .	45
6.1	3D bin in $E_{vis}$ , $x_{vis}$ , and $z_{vis}$ phase space. Crosses denote data, and points represent Monte Carlo events. . . . .	48

6.2	NuTeV $x$ , $z$ , and $E$ distributions for dimuons. Neutrino mode is on the left, anti-neutrino mode is on the right. Crosses represent the data. Circles represent strange sea contribution, stars - $d$ quark contribution, and boxes - $\pi K$ background. The histogram is the sum of all model contributions. $\chi^2$ for total degrees of freedom is shown for each plot. . . . .	54
6.3	NuTeV inelasticity $y$ , W boson momentum $Q^2$ , and the opening angle between two muons distributions for dimuons. Neutrino mode is on the left, anti-neutrino mode is on the right. Crosses represent the data. Circles represent strange sea contribution, stars - $d$ quark contribution, and boxes - $\pi K$ background. The histogram is the sum of all model contributions. $\chi^2$ for total degrees of freedom is shown for each plot. . . . .	55
6.4	NuTeV energy of the first muon, energy of the second muon, and the hadronic energy distributions for dimuons. Neutrino mode is on the left, anti-neutrino mode is on the right. Crosses represent the data. Circles represent strange sea contribution, stars - $d$ quark contribution, and boxes - $\pi K$ background. The histogram is the sum of all model contributions. $\chi^2$ for total degrees of freedom is shown for each plot. . . . .	56
6.5	NuTeV strange (top) sea and anti-strange (bottom) sea as functions of Bjorken $x$ for $Q^2 = 16 \text{ GeV}^2$ . Hatched - BGPARG model. The solid lines bound GRV fit region, dashed lines - CTEQ. . . . .	57
6.6	NuTeV strange sea (hatched) vs. anti-strange sea (dashed) for $Q^2 = 16 \text{ GeV}^2$ . Top - BGPARG model, middle - GRV, and bottom - CTEQ.	58



6.7	CCFR $x$ , $z$ , and $E$ distributions for dimuons. Neutrino mode is on the left, anti-neutrino mode is on the right. Crosses represent the data. Circles represent strange sea contribution, stars - $d$ quark contribution, and boxes - $\pi K$ background. The histogram is the sum of all model contributions. $\chi^2$ for total degrees of freedom is shown for each plot. . . . .	65
6.8	CCFR inelasticity $y$ , W boson momentum $Q^2$ , and the opening angle between two muons distributions for dimuons. Neutrino mode is on the left, anti-neutrino mode is on the right. Crosses represent the data. Circles represent strange sea contribution, stars - $d$ quark contribution, and boxes - $\pi K$ background. The histogram is the sum of all model contributions. $\chi^2$ for total degrees of freedom is shown for each plot. . . . .	66
6.9	CCFR energy of the first muon, energy of the second muon, and the hadronic energy distributions for dimuons. Neutrino mode is on the left, anti-neutrino mode is on the right. Crosses represent the data. Circles represent strange sea contribution, stars - $d$ quark contribution, and boxes - $\pi K$ background. The histogram is the sum of all model contributions. $\chi^2$ for total degrees of freedom is shown for each plot. . . . .	67
6.10	CCFR strange (top) sea and anti-strange (bottom) sea as functions of Bjorken $x$ for $Q^2 = 16 \text{ GeV}^2$ . Hatched - BGPARG model. The solid lines bound GRV fit region, dashed lines - CTEQ. . . . .	68
6.11	CCFR strange sea (hatched) vs. anti-strange sea (dashed) for $Q^2 = 16 \text{ GeV}^2$ . Top - BGPARG model, middle - GRV, and bottom - CTEQ.	69
6.12	NuTeV strange sea (hatched) vs. CCFR strange sea (solid) for $Q^2 = 16 \text{ GeV}^2$ , BGPARG model. Top - neutrino mode, bottom - anti-neutrino mode . . . . .	70

6.13	NuTeV $x$ toroid-toroid distribution. Neutrino mode is on the top, anti-neutrino mode is on the bottom. Crosses represent the data. Circles represent strange sea contribution, stars - $d$ quark contribution, and boxes - $\pi K$ background. The histogram is the sum of all model contributions. $\chi^2$ for total degrees of freedom is shown for each plot. . . . .	71
6.14	NuTeV same sign dimuons, toroid-toroid sample. Neutrino mode is on the top, anti-neutrino mode is on the bottom. Crosses represent the data. Circles represent strange sea contribution, stars - $d$ quark contribution, and boxes - $\pi K$ background. The histogram is the sum of all model contributions. $\chi^2$ for total degrees of freedom is shown for each plot. . . . .	72
6.15	NuTeV $z_{vis}$ distributions. Top - full sample, Bottom - only toroid-toroid events. $\nu$ s are on the left, $\bar{\nu}$ s are on the right. . . . .	73
6.16	NuTeV $z_{vis}$ distributions. Left - full sample vs. only toroid-toroid events. Right - the ratio of the histograms on the left side. Top - $\nu$ mode, bottom - $\bar{\nu}$ mode. . . . .	74
6.17	NuTeV and CCFR $z_{vis}$ distributions. Top - NuTeV vs. CCFR. Bottom - the ratio of the histograms on the left side. . . . .	75
6.18	Fragmentation function for different $\epsilon$ s. The higher the $\epsilon$ , the more the function's peak is shifted to the left. Histogram represents NuTeV full sample, and crosses - NuTeV toroid-toroid sample. . . .	76
7.1	DOF and $\chi^2$ as a function of coverage area . . . . .	85
7.2	Pulls. Solid line - input parameter, dashed - average over fake data fits, crosses - errors on input parameters, squares - average error on fake data parameters. Points with errorbars represent the result of the fit to each fake data sample. . . . .	87

7.3	Pulls. Solid line - input parameter, dashed - average over fake data fits, squares - average error on input parameters (same as in Fig.7.2). Points with errorbars represent the average over all fits to the fake data tables. The result is shown as the function of the coverage area for each of the parameters. . . . .	88
7.4	$\sigma_{2\mu}(x)$ from NuTeV neutrinos, for various $E_\nu - y$ bins in units of charged-current $\sigma$ . The cross-section extracted using the BGPARG model in the Monte Carlo is shown in squares, the circles correspond to extraction using the CTEQ model, and the triangles to the GRV model. The curves show the model prediction for GRV (dashed), CTEQ (dotted), and BGPARG (solid) after the models have been fit to the data. . . . .	89
7.5	$\sigma_{2\mu}(x)$ from NuTeV anti-neutrinos, for various $E_\nu - y$ bins in units of charged-current $\sigma$ . The cross-section extracted using the BGPARG model in the Monte Carlo is shown in squares, the circles correspond to extraction using the CTEQ model, and the triangles to the GRV model. The curves show the model prediction for GRV (dashed), CTEQ (dotted), and BGPARG (solid) after the models have been fit to the data. . . . .	90
7.6	$\sigma_{2\mu}(x)$ from CCFR neutrinos, for various $E_\nu - y$ bins in units of charged-current $\sigma$ . The cross-section extracted using the BGPARG model in the Monte Carlo is shown in squares, the circles correspond to extraction using the CTEQ model, and the triangles to the GRV model. The curves show the model prediction for GRV (dashed), CTEQ (dotted), and BGPARG (solid) after the models have been fit to the data. . . . .	91

7.7	$\sigma_{2\mu}(x)$ from CCFR anti-neutrinos, for various $E_\nu - y$ bins in units of charged-current $\sigma$ . The cross-section extracted using the BGPARG model in the Monte Carlo is shown in squares, the circles correspond to extraction using the CTEQ model, and the triangles to the GRV model. The curves show the model prediction for GRV (dashed), CTEQ (dotted), and BGPARG (solid) after the models have been fit to the data. . . . .	92
-----	---	----

# List of Tables

1.1	The fundamental forces . . . . .	3
1.2	The constituents of matter . . . . .	4
3.1	NuTeV trigger list with descriptions . . . . .	29
5.1	Coefficients for <i>Mean</i> (top two rows) and <i>Width</i> hadronic energy distributions. . . . .	41
5.2	Coefficients for <i>Mean</i> (top two rows) and Width muon energy distributions. . . . .	41
6.1	Results of LO fits to NuTeV data. The first error is statistical, the second systematic. On the far right is the $\chi^2$ per degree of freedom. . . . .	50
6.2	Results of LO fits to NuTeV data. The first error is statistical, the second systematic. . . . .	51
6.3	Systematic error sources for LO-QCD fit to NuTeV data. . . . .	52
6.4	Results of LO fits to CCFR data. The first error is statistical, the second systematic. The far right column shows $\chi^2$ per degree of freedom . . . . .	59
6.5	Results of LO fits to CCFR data. The first error is statistical, the second systematic. . . . .	59

6.6	High- $x$ events using the anti-neutrino data sample. $E_{VIS}$ is in GeV, $N_{x>0.5}$ is the number of observed events for $x_{VIS} > 0.5$ , $MC$ is the Monte Carlo prediction for $x_{VIS} > 0.5$ , $N_{\pi/k}$ and $N_{\bar{s}}$ are the $\pi/K$ decay and $\bar{s}$ contributions to $MC$ , $N_{tot}$ is the total number of dimuon events, and $\frac{M}{M_{e>5}}$ is the Monte Carlo correction in Eq. 6.8 .	63
6.7	High- $x$ events using the neutrino data sample. $E_{VIS}$ is in GeV, $N_{x>0.5}$ is the number of observed events for $x_{VIS} > 0.5$ , $MC$ is the Monte Carlo prediction for $x_{VIS} > 0.5$ , $N_{\pi/k}$ and $N_s$ are the $\pi/K$ decay and $s$ contributions to $MC$ , $N_{tot}$ is the total number of dimuon events, and $\frac{M}{M_{e>5}}$ is the Monte Carlo correction in Eq. 6.8. .	63
7.1	Results of LO fits to the cross-section tables extracted from the NuTeV, CCFR, and combined data sets. . . . .	86
A.1	NuTeV forward differential cross-section for $\nu_\mu N \rightarrow \mu^- \mu^+ X$ at $E \sim 90.18$ GeV. The forward cross-section requires $E_{\mu^+} \geq 5$ GeV, and the cross-section values should be multiplied by $\frac{1}{100} \times G_F^2 ME/\pi$ . The first error given for the cross-sections is statistical and the second systematic. Units are in GeV or GeV <sup>2</sup> , where appropriate, for the averages of the kinematic quantities. . . . .	95
A.2	NuTeV forward differential cross-section for $\nu_\mu N \rightarrow \mu^- \mu^+ X$ at $E \sim 174.37$ GeV. The forward cross-section requires $E_{\mu^+} \geq 5$ GeV, and the cross-section values should be multiplied by $\frac{1}{100} \times G_F^2 ME/\pi$ . The first error given for the cross-sections is statistical and the second systematic. Units are in GeV or GeV <sup>2</sup> , where appropriate, for the averages of the kinematic quantities. . . . .	96

A.3	NuTeV forward differential cross-section for $\nu_\mu N \rightarrow \mu^- \mu^+ X$ at $E \sim 244.72$ GeV. The forward cross-section requires $E_{\mu^+} \geq 5$ GeV, and the cross-section values should be multiplied by $\frac{1}{100} \times G_F^2 M E / \pi$ . The first error given for the cross-sections is statistical and the second systematic. Units are in GeV or GeV <sup>2</sup> , where appropriate, for the averages of the kinematic quantities. . . . .	97
A.4	NuTeV forward differential cross-section for $\bar{\nu}_\mu N \rightarrow \mu^+ \mu^- X$ at $E \sim 78.97$ GeV. The forward cross-section requires $E_{\mu^-} \geq 5$ GeV, and the cross-section values should be multiplied by $G_F^2 M E / \pi$ . The first error given for the cross-sections is statistical and the second systematic. Units are in GeV or GeV <sup>2</sup> , where appropriate, for the averages of the kinematic quantities. . . . .	98
A.5	NuTeV forward differential cross-section for $\bar{\nu}_\mu N \rightarrow \mu^+ \mu^- X$ at $E \sim 146.06$ GeV. The forward cross-section requires $E_{\mu^-} \geq 5$ GeV, and the cross-section values should be multiplied by $G_F^2 M E / \pi$ . The first error given for the cross-sections is statistical and the second systematic. Units are in GeV or GeV <sup>2</sup> , where appropriate, for the averages of the kinematic quantities. . . . .	99
A.6	NuTeV forward differential cross-section for $\bar{\nu}_\mu N \rightarrow \mu^+ \mu^- X$ at $E \sim 222.14$ GeV. The forward cross-section requires $E_{\mu^-} \geq 5$ GeV, and the cross-section values should be multiplied by $G_F^2 M E / \pi$ . The first error given for the cross-sections is statistical and the second systematic. Units are in GeV or GeV <sup>2</sup> , where appropriate, for the averages of the kinematic quantities. . . . .	100

- A.7 CCFR E744/E770 forward differential cross-section for  $\nu_\mu N \rightarrow \mu^- \mu^+ X$  at  $E \sim 109.46$  GeV. The forward cross-section requires  $E_{\mu^+} \geq 5$  GeV, and the cross-section values should be multiplied by  $G_F^2 ME/\pi$ . The first error given for the cross-sections is statistical and the second systematic. Units are in GeV or  $\text{GeV}^2$ , where appropriate, for the averages of the kinematic quantities. . . . . 101
- A.8 CCFR E744/E770 forward differential cross-section for  $\nu_\mu N \rightarrow \mu^- \mu^+ X$  at  $E \sim 209.89$  GeV. The forward cross-section requires  $E_{\mu^+} \geq 5$  GeV, and the cross-section values should be multiplied by  $G_F^2 ME/\pi$ . The first error given for the cross-sections is statistical and the second systematic. Units are in GeV or  $\text{GeV}^2$ , where appropriate, for the averages of the kinematic quantities. . . . . 102
- A.9 CCFR E744/E770 forward differential cross-section for  $\nu_\mu N \rightarrow \mu^- \mu^+ X$  at  $E \sim 332.70$  GeV. The forward cross-section requires  $E_{\mu^+} \geq 5$  GeV, and the cross-section values should be multiplied by  $G_F^2 ME/\pi$ . The first error given for the cross-sections is statistical and the second systematic. Units are in GeV or  $\text{GeV}^2$ , where appropriate, for the averages of the kinematic quantities. . . . . 103
- A.10 CCFR E744/E770 forward differential cross-section for  $\bar{\nu}_\mu N \rightarrow \mu^+ \mu^- X$  at  $E \sim 87.48$  GeV. The forward cross-section requires  $E_{\mu^-} \geq 5$  GeV, and the cross-section values should be multiplied by  $G_F^2 ME/\pi$ . The first error given for the cross-sections is statistical and the second systematic. Units are in GeV or  $\text{GeV}^2$ , where appropriate, for the averages of the kinematic quantities. . . . . 104



- A.11 CCFR E744/E770 forward differential cross-section for  $\bar{\nu}_\mu N \rightarrow \mu^+ \mu^- X$  at  $E \sim 160.70$  GeV. The forward cross-section requires  $E_{\mu^-} \geq 5$  GeV, and the cross-section values should be multiplied by  $G_F^2 ME/\pi$ . The first error given for the cross-sections is statistical and the second systematic. Units are in GeV or GeV<sup>2</sup>, where appropriate, for the averages of the kinematic quantities. . . . . 105
- A.12 CCFR E744/E770 forward differential cross-section for  $\bar{\nu}_\mu N \rightarrow \mu^+ \mu^- X$  at  $E \sim 265.82$  GeV. The forward cross-section requires  $E_{\mu^-} \geq 5$  GeV, and the cross-section values should be multiplied by  $G_F^2 ME/\pi$ . The first error given for the cross-sections is statistical and the second systematic. Units are in GeV or GeV<sup>2</sup>, where appropriate, for the averages of the kinematic quantities. . . . . 106

# Chapter 1

## Introduction

Neutrino-nucleon deep inelastic scattering is a very effective way to probe the structure of the nucleon and to study the dynamics of heavy quark production. The presented analysis focuses on charm quark production in deep inelastic scattering of neutrinos and anti-neutrinos off a nucleon. Data sample is based on opposite sign dimuon events that was obtained by the Fermilab experiment E815 (or NuTeV) experiment in fixed-target run during 1995-1998 at the Fermi National Accelerator Laboratory.

Dimuon events primarily come from charged current (CC) production of charm quarks through the following sub-processes:

$$\begin{aligned}\nu_\mu + (d, s) &\rightarrow \mu^- + c + X \\ &\hookrightarrow \mu^+ + \bar{\nu}_\mu,\end{aligned}\tag{1.1}$$

$$\begin{aligned}\bar{\nu}_\mu + (\bar{s}) &\rightarrow \mu^+ + \bar{c} + X \\ &\hookrightarrow \mu^- + \nu_\mu.\end{aligned}\tag{1.2}$$

In Eq.1.1, a neutrino ( $\nu_\mu$ ) interacts with a down ( $d$ ) or strange ( $s$ ) quark inside

a nucleon and produces a negatively charged muon ( $\mu^-$ ), a charm quark ( $c$ ), and a hadron shower ( $X$ ). The charm quark pairs with an anti-quark ( $\bar{q}$ ) from quark sea forming one of the  $D$  mesons. A  $D$  meson decays about 10% of the time into  $\mu^+$  and anti-neutrino. In second equation all particles in first one are substituted by their anti-particles. It is important to point out that in anti-neutrino scattering almost all dimuon events come from anti-strange quark while in neutrino scattering only 50% of events are initiated by the strange quark.

Therefore the dimuon data allows to measure the charm quark mass  $m_c$ , nucleon strange quark probability distribution functions, the fragmentation function that describes how a charm quark couples with anti-quark to form a charmed hadron, and the semi-leptonic charm decay branching ratio ( $B_c$ ).

Following this rather terse statement of the physics addressed in this thesis are several sections that briefly introduce quarks and leptons and forces by which they interact as a part of the so-called Standard Model. A brief explanation of deep-inelastic scattering is introduced, as are descriptions of other processes that have to be dealt with in this analysis.

Chapter 2 provides more detail on neutrino-nucleon scattering and charm production. Chapter 3 describes the experimental apparatus. Chapter 4 outlines the selection criteria used in this analysis. The physics results are presented in chapters 5 and 6<sup>1</sup>.

## 1.1 Standard Model

All forces in modern physics are described by quantum field theories (QFT). Forces are mediated by field quanta, the so-called gauge bosons. Currently there are four known forces: strong, electromagnetic, weak and gravitational. The dynamics of each force are determined by an underlying gauge symmetry[1]. Their relative

---

<sup>1</sup>A condensed version of this thesis has been published in Physics Review D [43].

<i>force</i>	<i>relative strength</i>	<i>Mediator</i>	<i>Participating fermions</i>
strong	1.	gluons (g)	quarks
electromagnetic	1/137	photon( $\gamma$ )	quarks and charged leptons
weak	$10^{-5}$	$W^{\pm}$ , Z	all
gravity	$10^{-40}$	[graviton(G)]	all

Table 1.1: The fundamental forces

strengths and mediator particles are shown in the Table 1.1. The Standard Model (SM)[2] is a unified theory of strong, electromagnetic, and weak forces. The strong force is responsible for short range binding of protons and neutrons within nucleus. The theory describing the strong force obeys an  $SU(3)$ -color symmetry and is known as Quantum Chromodynamics (QCD)[3, 4]. The strong force is mediated by gluons. Each quark carries a color charge that can be denoted as red, blue, or green. Each particle must be color neutral, meaning that it is an  $SU(3)$  singlet. Mesons are particles composed of a quark and an anti-quark. Mesons are color neutral because an anti-quark has an opposite color as the quark. Baryons are composed of three quarks or anti-quarks so that the combined color singlet can be thought of as blue + red + green = white.

The electroweak gauge theory[5, 6], based upon the  $SU(2) \times U(1)$  symmetry group, unifies electromagnetic and weak forces. The electromagnetic force obeys a  $U(1)$  charge symmetry and is mediated by massless photons, while the weak force obeys  $SU(2)$  weak isospin symmetry and is mediated by relatively heavy  $W$  and  $Z$  bosons.  $W$  bosons can carry electric charge of +1 or -1 (in units of the proton charge); the  $Z$  boson has no charge. If an interaction is mediated by a  $W$  boson, it is a *charged current interaction* (CC). The  $Z$  boson is associated with *neutral current* (NC) interactions. The combination of electroweak and strong interactions is now described by the  $SU(3) \times SU(2) \times (U1)$  group in a scheme referred to as the Standard Model (SM).

QUARKS			
<i>electric charge</i>	<i>lightest</i>	<i>heavier</i>	<i>heaviest</i>
+2/3e	up (u)	charm (c)	top (t)
-1/3e	down (d)	strange (s)	bottom (b)
LEPTONS			
<i>electric charge</i>	<i>lightest</i>	<i>heavier</i>	<i>heaviest</i>
-1e	electron (e)	muon ( $\mu$ )	tau( $\tau$ )
0	e-neutrino( $\nu_e$ )	$\mu$ -neutrino( $\nu_\mu$ )	$\tau$ -neutrino( $\nu_\tau$ )

Table 1.2: The constituents of matter

All elementary particles in the SM are listed in the Table1.2. All matter on Earth is build from  $u$  and  $d$  quarks and electrons. The proton is a combination of  $uud$  quarks and the neutron is a combination of  $ddu$  quarks. These  $u$  and  $d$  quarks are thus referred to as “valence” quarks. All quark types can also show up inside a nucleon as a quark-anti-quark quantum fluctuation; in this case, they are referred to as “sea” quarks.

The neutrino is a neutral lepton and participates only in weak interactions. The process described by Eq.1.1 is a weak CC interaction. All neutrino CC interactions with quarks change *flavor* (or quark type). For example: if a neutrino strikes a  $d$  quark via  $W$  boson exchange, the  $d$  quark changes into some other quark that can be an  $u$ ,  $c$ , or  $t$ . In nature, the weak flavor eigenstates of quarks that participate in CC interactions are not the same quantum states as those that form massive propagating hadrons. The weak eigenstates of the down-like quarks are written as an admixture of the mass eigenstates of the down-like quarks:

$$V = \begin{pmatrix} d' \\ s' \\ b' \end{pmatrix} = \begin{pmatrix} V_{ud} & V_{us} & V_{ub} \\ V_{cd} & V_{cs} & V_{cb} \\ V_{td} & V_{ts} & V_{tb} \end{pmatrix} \begin{pmatrix} d \\ s \\ b \end{pmatrix} \quad (1.3)$$

The matrix in Eq.1.3 is called the Cabibbo-Kobayashi-Maskawa (CKM) matrix. The CKM matrix is assumed to be unitary. This implies that there are no flavor-changing NC interactions, and that, for example,  $|V_{ud}|^2 + |V_{cd}|^2 + |V_{td}|^2 = 1$ .

## 1.2 Asymptotic Freedom

The SU(3)-color symmetry group (on which QCD is based) is *non-Abelian*, which means that the mediators (gluons) are allowed to interact with one another. Each gluon carries one unit of color and one of anti-color. In terms of color SU(3) symmetry, there are eight states that form a “color octet”, and one state that is a “color singlet”. In nature, “free” gluons do not exist; all free particles are color singlets. Therefore there are only eight gluons, and all of them are color octets. If a color singlet existed, it could be exchanged between color singlets (neutron and proton, for example), giving rise to a long-range force. But we know that the strong force is of short range. Physically, this leads to the effect (asymptotic freedom) that the coupling strength decreases as the interacting particles get closer together (larger  $|q^2|$ ). This can be thought of as the consequence of the Heisenberg uncertainty principle: the shorter the distance between interacting particles (smaller interaction time), the higher the energy carried by the mediator particle. The qualitative explanation is that gluon-gluon interactions produce an “anti-screening” effect, Fig.1.1.

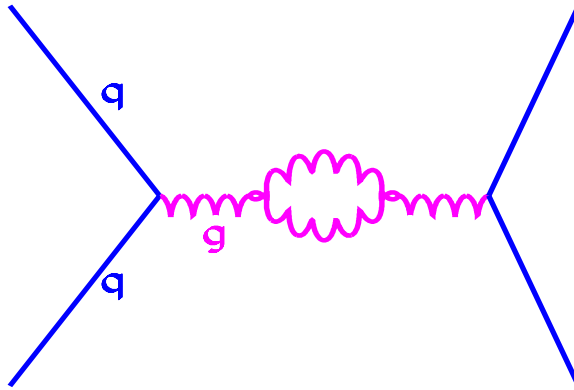


Figure 1.1: Gluon screening.

In neutrino scattering, if a  $W$  boson has high enough squared momentum  $Q^2$ , it strikes a quark inside a nucleus that is “free”, or not bound to other quarks (a picture known as the parton model). The strong force that is responsible for binding quarks is weaker at short distances or, equivalently, large  $Q^2$ . This property

is referred to as asymptotic freedom and is expressed by the formula

$$\alpha_s(Q^2) = \frac{12\pi}{(11n - 2f) \log(Q^2/\Lambda_{QCD}^2)}, \quad (1.4)$$

where  $\alpha_s$  is a strong coupling constant, and  $\Lambda_{QCD}$  is a constant around 200 MeV[7].  $n$  is the number of colors (3 in SM),  $f$  is the number of flavors with  $m_{quark}^2 \ll Q^2$  (6 in general, 3 at NuTeV).

If  $Q^2 \gg \Lambda_{QCD}^2$ , the perturbative description of QCD is valid. Otherwise, asymptotic freedom breaks down, the parton model is no longer valid, and, as a result, quarks cannot be treated as free particle. In this case QCD becomes non-perturbative. In NuTeV dimuon events have average  $Q_{vis}^2 \approx 21.1 \text{ GeV}^2 \gg \Lambda_{QCD}^2$ , thus it is appropriate to think of a neutrino interacting with a single quark that is “free”. Therefore perturbative QCD is valid as a theoretical model in the NuTeV regime.

The coupling strength in QCD behaves in exactly the opposite way as the coupling strength in QED, which describes electromagnetism. In QED, photons are the electromagnetic force carriers. A photon is a “QED color singlet”, which means that it exists as a free particle, and can be exchanged between other color singlets, giving rise to the long range property of the electromagnetic force. In QED, the closer interacting particles get together (larger  $|q|^2$ ), the *stronger* the force gets.

### 1.3 Deep Inelastic Scattering

The deep inelastic scattering model assumes that an incoming neutrino interacts with a single free quark inside the nucleon. In the previous section it is shown that this is an appropriate assumption for NuTeV CC events. In order for neutrino scattering to be deeply inelastic, the time of interaction must be small so that the neutrino exchanges energy only with the struck quark. Therefore there are two conditions that must be true for interaction to be called deep inelastic:

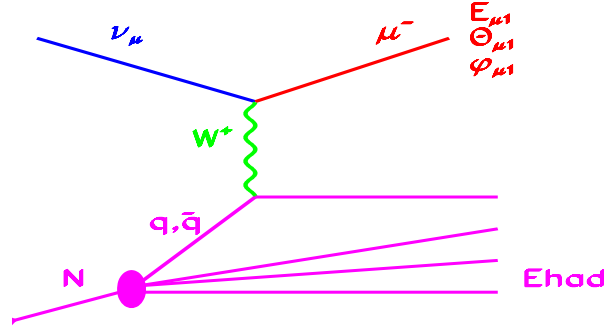


Figure 1.2: CC diagram  $\nu\mu(\bar{\nu}\mu)N \rightarrow \mu^-(\mu^+)X$ .

$$\begin{aligned} \tau_{int} &\sim 1/E_\nu \ll \tau_{glue}, \\ Q^2 &\gg \Lambda_{QCD}^2. \end{aligned} \tag{1.5}$$

The first expression in Eq.1.6 states that the duration of an interaction must be much smaller than the time it takes two quarks to exchange a gluon. It amounts to requiring the neutrino to transfer a high energy. The second equation means that the momentum transferred by  $W^+(W^-)$  must be much greater than the binding energy between quarks inside nucleon so that a perturbative QCD treatment can be applied.

Charged current deep inelastic scattering is illustrated by the *Feynmann diagram* shown in Fig.1.2. At the primary vertex the muon neutrino emits a  $W$  boson and turns into a muon. The  $W$  boson interacts with one of the quarks within the nucleon at the secondary vertex, changing the quark's flavor. This quark, along with the remaining quarks inside nucleon, must quickly combine with other quarks to create mesons and baryons. In the detector this results in an outgoing muon and a burst of hadrons as shown in Fig.1.3.



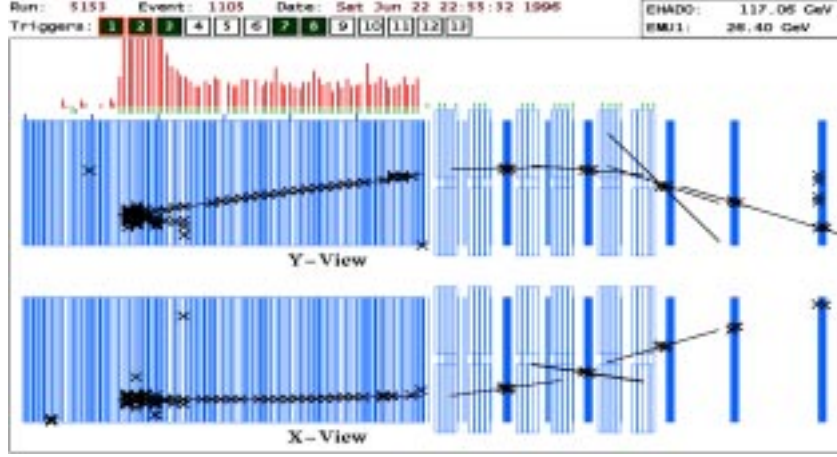


Figure 1.3: Typical CC event

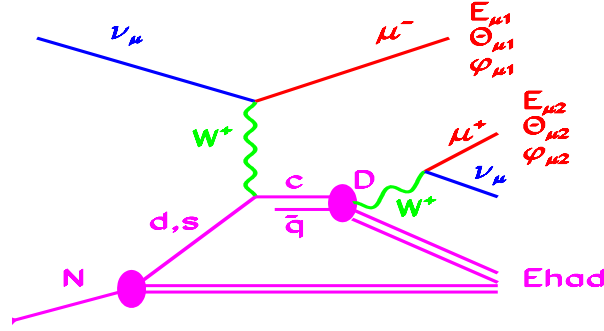


Figure 1.4: CC charm production  $\nu\mu(\bar{\nu}_\mu)N \rightarrow \mu^-(\mu^+)X$ .

## 1.4 Dimuon production

In the CC interaction shown in Fig.1.2, the  $W$  boson could hit  $d$  or  $s$  quark. There is a small, but non-zero, probability that  $d$  quark will turn into a  $c$ . The probability of an  $s$  quark turning into  $c$  is close to 1. Since there are no valance strange quarks, the  $d$  valance quark distribution dominates  $s$  quarks. As a result, a charm quark is produced approximately half of a time from  $d$  and half of a time from  $s$  quarks. In the case of the anti-neutrino interactions, an anti-charm quark  $\bar{c}$  can come either from  $\bar{d}$  or from  $\bar{s}$ , only this time both  $\bar{d}$  and  $\bar{s}$  quarks are sea

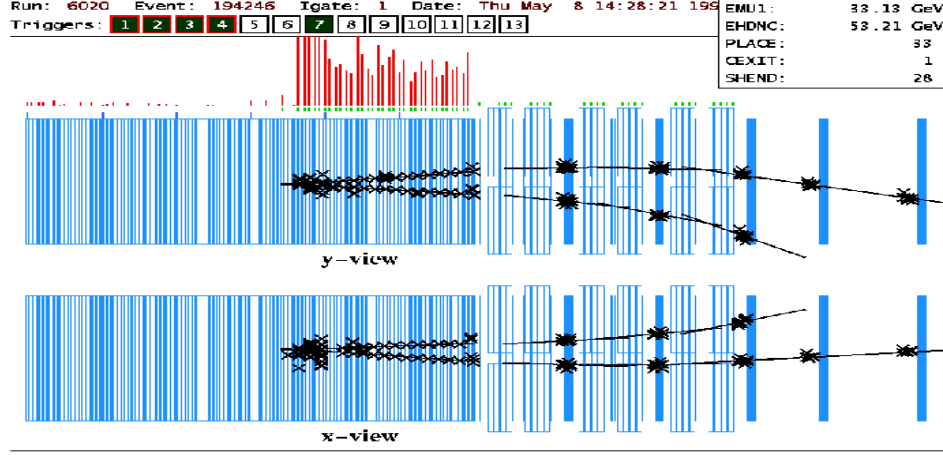


Figure 1.5: Typical dimuon event

quarks; and, since  $V_{cs}$  is much bigger than  $V_{cd}$ , almost all charm production comes from  $\bar{s}$  quarks.

The dimuon event starts exactly like an ordinary CC event except the  $W$  strikes a  $s$  or  $d$  quark inside a nucleon turning it into charm quark  $c$ . The charm quark combines with some anti-quark from the quark sea forming a charmed hadron; either a  $D^0$  ( $c\bar{u}$ ),  $D^+$  ( $c\bar{d}$ ), or  $D_s^+$  ( $c\bar{s}$ ) meson or a  $\Lambda_c$  ( $cud$ ) baryon. A charmed hadron weakly decays approximately 10% of the time into a neutrino and a muon that carries opposite charge from the first muon. In the detector these events have a very distinct signature called a *dimuon event*: two oppositely charged muons and a hadron shower as shown in Fig.1.5. Muons are easily recognized as the only particles that can penetrate a substantial distance through the detector steel. The only other significant source of a signal like that would be from a second muon produced inside the hadronic shower of an ordinary CC process. This turns out to be a fairly rare occurrence.

The focus of this analysis is to select dimuon events from a data sample and compare them to Monte Carlo prediction that uses specific dimuon production and background models by performing maximum likelihood fit. As a result of the fit, I extract parameters such as charm quark mass  $m_c$ , shape and absolute value of strange sea, charm - anti-quark fragmentation, and  $D$  meson decay branching

ratio  $B_c$ . I also developed a method to “invert” the model so that the result can be presented in nearly model-independent way that would make testing of different theories of charm production easy to do.

## Chapter 2

# Neutrino-Nucleon Scattering and Charm Production

Neutrinos are excellent probes for studying the structure of hadrons because they are structureless and chargeless elementary particles whose electroweak interactions are well understood. Neutrinos are always polarized, and therefore suited for studies of the helicity dependent dynamics of the nucleon constituents. This is valuable because the  $W^-$  ( $W^+$ ) boson couples only to left (right) handed fermions and right (left) handed anti-fermions. The process of probing nucleon structure starts with using inclusive charged current data to measure nucleon's *structure functions*: a complete set of Lorentz scalars that parameterize the structure of the nucleon. Nucleon structure is associated with *partons*, QCD's quarks and gluons. QCD describes the parton dynamics, and the structure function measurements provide a determination of the nucleon's valence and sea quark distributions as well as the gluon distribution.

Dimuon data, a sub-sample of full charged current sample, provides a determination of a strange sea quark distribution. Dimuon events are the result of heavy charm quark production. The NuTeV kinematic region permits a measurement of the charm quark mass  $m_c$ . In order for a charm particle to produce a second

muon, it must decay; thus, it is possible to measure the semileptonic decay branching ratio  $B_c$ , or, equivalently, the  $V_{cd}$  CKM matrix element, and to study charm fragmentation models. Leading order QCD (LO) and next-to-leading order QCD (NLO) treatments of dimuon production are also discussed in this chapter.

## 2.1 Charged Current Kinematics

Kinematics for a charged current interaction are illustrated on Fig. 2.1.

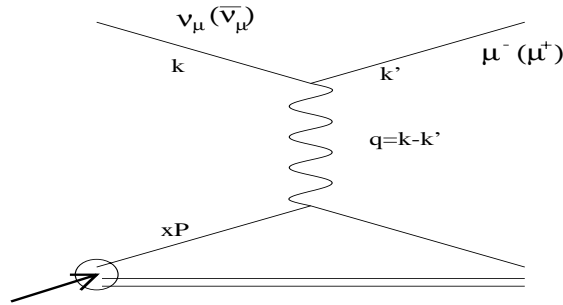


Figure 2.1: Kinematics of Neutrino Nucleon Scattering.

The energy-momentum four-vectors for the incoming neutrino ( $k$ ), muon at a primary vertex ( $k'$ ), target nucleon ( $p$ ), and hadronic system ( $p'$ ) may be written

$$\begin{aligned} k &= (E_\nu, 0, 0, E_\nu), \\ p &= (M, 0, 0, 0), \\ k' &= (E_\mu, p_\mu \sin \theta_\mu \cos \phi_\mu, p_\mu \sin \theta_\mu \sin \phi_\mu, p_\mu \cos \theta_\mu), \\ p' &= p + q = p + (k - k'), \end{aligned} \tag{2.1}$$

where  $E_\nu$  is the energy of the incoming neutrino;  $E_\mu$ ,  $\theta_\mu$ , and  $\phi_\mu$  are the energy, polar angle, and azimuthal angle of the muon;  $q$  is the 4-momentum of the W boson; and  $M$  is the nucleon mass. The following kinematic variables are usually defined:

$$Q^2 = -q^2 = -(k - k')^2 = -m^2 + 2E_\nu(E_\mu - p_\mu \cos \theta_\mu), \tag{2.2}$$

$$\begin{aligned}
x &= \frac{-q^2}{2p \cdot q} = \frac{Q^2}{2ME_{had}}, \\
y &= \frac{p \cdot q}{p \cdot k} = \frac{E_{had}}{E_\nu}, \\
z &= E_D/E_c, \\
\nu &= \frac{p \cdot q}{M} = E_{had},
\end{aligned}$$

where  $Q^2$  is the squared momentum transferred by the W-boson from the primary to the secondary vertex,  $x$  is the Bjorken scaling variable,  $y$  is the inelasticity that determines what fraction the total initial energy is transferred to the hadrons, and  $\nu$  is the energy transferred to the hadronic system. In the case of charm production,  $z$  is the ratio of the energy carried by the D-meson to the energy carried by the  $c$  quark.

In the case of massless final state quarks, conservation of 4-momentum requires

$$\begin{aligned}
(\xi P + q)^2 &\simeq 0, \\
\xi^2 p^2 + q^2 + 2 \cdot \xi p \cdot q &\simeq 0, \\
\xi &= \frac{-q^2}{2ME_\nu} = x,
\end{aligned} \tag{2.3}$$

where  $\xi$  is the fraction of the nucleon 4-momentum carried by the struck quark. If the momentum transferred is much greater than the mass of a struck quark ( $-q^2 \gg x^2 p^2$ ), then  $\xi \cong x$ . Therefor,  $x$  is associated with the momentum carried by the struck quark for the case of massless quark production.

In charm semi-muonic decay, there is always a neutrino that completely escapes detection and can only be accounted for in a Monte Carlo simulation. The variables given in Eq.2.4 are calculated from quantities that are observed in the detector ( $E_\mu, E_{had}, \theta_\mu$ ) or “visible” quantities which correspond to the “true” variables defined in Eq.2.2. They appear with a subscript “vis”, and are defined as

$$\begin{aligned}
E_{vis}^\nu &= E_{\mu 1} + E_{\mu 2} + E_{had}, \\
Q_{vis}^2 &= -m_\mu^2 + 2E_\nu \cdot E_{\mu 1} \cdot (1 - \cos \theta 1), \\
x_{vis} &= Q_{vis}^2 / (2 \cdot M \cdot E_{had}),
\end{aligned} \tag{2.4}$$

$$\begin{aligned}
y_{vis} &= E_{had}/E_{\nu}^{vis}, \\
z_{vis} &= E_{\mu 2}/(E_{had} + E_{\mu 2}).
\end{aligned}$$

## 2.2 Charged-Current Cross Section

To derive the neutrino-nucleon scattering differential cross section, one starts with Fermi's Golden Rule [4]

$$d\sigma = \frac{2\pi}{\hbar} d\Gamma \frac{|M|^2}{\Phi}, \quad (2.5)$$

where  $\Phi$  is the incident neutrino flux,  $|M|^2$  is the squared scattering amplitude, and  $d\Gamma$  is the density of final states.

The matrix element  $M$  factorizes into a product of leptonic and hadronic currents linked by the  $W$  boson, and can be written as

$$M = L_{\alpha\beta} \frac{\sqrt{2}G_F}{1 + \frac{Q^2}{M_W^2}} W^{\alpha\beta}, \quad (2.6)$$

where the convention that a double appearance of an index implies a sum over the 4 space-time dimension. The leptonic tensor is precisely known from the SM to be

$$\begin{aligned}
L_{\alpha\beta} &= \bar{u}(k')\gamma^\alpha(1 - \gamma_5)u(k) \\
&= 8(k_\alpha k'_\beta + k_\beta k'_\alpha - g_{\alpha\beta}k \cdot k' \mp i\epsilon_{\alpha\beta\gamma\delta}k^\gamma k'^\delta)
\end{aligned} \quad (2.7)$$

where the last term is negative (positive) for neutrinos (anti-neutrinos).

The hadronic tensor parameterizes the unknown structure of the boson-nucleon vertex. It can depend only on two independent vectors -  $p$  and  $q$ , and so can be written as a sum of all possible second-rank tensors formed from  $p$  and  $q$ :

$$\begin{aligned}
W^{\alpha\beta} = & - g^{\alpha\beta}W_1 + \frac{p^\alpha p^\beta}{M^2}W_2 - i\epsilon^{\alpha\beta\gamma\delta}p_\gamma q_\delta W_3 \\
& + \frac{q^\alpha q^\beta}{M^2}W_4 + \frac{(p^\alpha q^\beta + p^\beta q^\alpha)}{M^2}W_5 \\
& + \frac{i(p^\alpha q^\beta - p^\beta q^\alpha)}{2M^2}W_6,
\end{aligned} \quad (2.8)$$

where  $W_i$  are Lorenz scalars that depend on  $q^2$  and  $p \cdot q$ . Contracting  $L_{\alpha\beta}W^{\alpha\beta}$ , discarding terms multiplied by  $W_4$ ,  $W_5$ , and  $W_6$  that are proportional to the incident lepton mass, and using the Jacobian transformation

$$E_\mu \frac{d^3\sigma}{d^3k'} = \frac{2MEx^2}{\pi Q^2} \frac{d^2\sigma}{dx dQ^2}, \quad (2.9)$$

the differential cross section can be written as a function of  $x$  and  $Q^2$  as

$$\begin{aligned} \frac{d^2\sigma}{dx dQ^2} = & \frac{G_F^2}{2\pi x(1 + Q^2/M_W^2)^2} (xy^2 MW_1 + \\ & (1 - y - \frac{xyM}{2E})\nu W_2 \pm xy(1 - \frac{y}{2})\nu W_3). \end{aligned} \quad (2.10)$$

Scaling structure functions are introduced via

$$\begin{aligned} 2xF_1(x, Q^2) &= 2xMW_1(\nu, Q^2), \\ F_2(x, Q^2) &= \nu W_2(\nu, Q^2), \\ xF_3(x, Q^2) &= x\nu W_3(\nu, Q^2), \end{aligned} \quad (2.11)$$

Finally, in terms of these structure functions, the differential cross section becomes

$$\begin{aligned} \frac{d^2\sigma^{\nu(\bar{\nu})}}{dx dy} = & \frac{G_F^2}{2\pi x(1 + Q^2/M_W^2)^2} \left[ xy^2 F_1^{\nu(\bar{\nu})} + \right. \\ & \left. (1 - y - \frac{xyM}{2E}) F_2^{\nu(\bar{\nu})} \pm xy(1 - \frac{y}{2}) F_3^{\nu(\bar{\nu})} \right]. \end{aligned} \quad (2.12)$$

This is the master equation of deep inelastic neutrino scattering. It shows that measurement of the differential cross section is equivalent to a measurement of three structure functions that contain all information about the struck nucleon.

## 2.3 The Parton Model

In the limit of  $Q^2 \rightarrow \infty$  and  $\nu \rightarrow \infty$ , the structure functions  $F(x, q^2)$  remain finite, and, to first approximation, dependent only on the dimensionless and finite ratio



of these two variables,  $-q^2/2M\nu$ , which is equal to Bjorken  $x$ . This is known as the *Bjorken scaling hypothesis*.

In the parton model the nucleon is represented as a collection of free partons. Each parton is a spin-1/2 ( $q, \bar{q}$ ) or spin-1 ( $g$ ) particle. The incident neutrino carries spin 1/2. Elastic scattering of point particles depends only on the center of mass energy and angular momentum of the system. The scattering angle in the center of mass frame is related to inelasticity  $y$  via

$$\cos \theta^* = \frac{1+y}{2}. \quad (2.13)$$

The scattering cross section can be written for the three possible total spin configurations as:

$$\begin{aligned} \text{total spin } 0 : \quad \frac{d\sigma^{\nu q}}{dy} &= \frac{d\sigma^{\bar{\nu} q}}{dy} = \frac{G_F^2 M E_\nu}{\pi(1 + Q^2/M_W^2)^2}, \\ \text{total spin } 1 : \quad \frac{d\sigma^{\nu q}}{dy} &= \frac{d\sigma^{\bar{\nu} q}}{dy} = \frac{G_F^2 M E_\nu}{\pi(1 + Q^2/M_W^2)^2} (1-y)^2, \\ \text{total spin } 1/2 : \quad \frac{d\sigma^{\nu k}}{dy} &= \frac{d\sigma^{\bar{\nu} k}}{dy} = \frac{2G_F^2 M E_\nu}{\pi(1 + Q^2/M_W^2)^2} (1-y), \end{aligned} \quad (2.14)$$

where  $k$  represents the combination of partons associated with total spin 1/2. Defining  $q(x, Q^2)$ ,  $\bar{q}(x, Q^2)$ ,  $k(x, Q^2)$  to be the probability of finding a particle inside nucleon carrying  $x$  fraction of nucleon's momentum, neutrino scattering cross section can be written as

$$\begin{aligned} \frac{d^2\sigma^{\nu N}}{dx dy} &= \left[ q(x) + \bar{q}(x)(1-y)^2 + 2k(x)(1-y) \right], \\ \frac{d^2\sigma^{\bar{\nu} N}}{dx dy} &= \left[ q(x)(1-y)^2 + \bar{q}(x) + 2k(x)(1-y) \right]. \end{aligned} \quad (2.15)$$

Comparing the above expression with Eq.2.12, one can write structure functions in terms of parton probability distributions (PDF):

$$\begin{aligned} 2xF_1 &= xq(x) + x\bar{q}(x), \\ F_2 &= xq(x) + x\bar{q}(x) + 2k(x), \\ xF_3 &= xq(x) - x\bar{q}(x). \end{aligned} \quad (2.16)$$

To leading order in QCD the spin 1/2 cross section is zero. This implies the *the Callan-Gross* relationship

$$2xF_1 \rightarrow F_2 \text{ as } Q^2 \rightarrow \infty. \quad (2.17)$$

## 2.4 Neutrino Scattering off a Real Target

In NuTeV, neutrinos scatter off an iron target that is a nearly equal mixture of protons and neutrons. One must rewrite the scattering cross sections to take into account the fact that protons and neutrons have different intrinsic structure.

Charged current interactions change the flavor of the struck quark, and conservation of charge at the quark vertex limits neutrinos to scatter from  $d$ ,  $s$ ,  $\bar{u}$  and  $\bar{c}$  quarks. Anti-neutrinos can scatter from  $\bar{d}$ ,  $\bar{s}$ ,  $u$  and  $c$  quarks. The neutron can be obtained from the proton by changing all  $d$ -type quarks into  $u$ -type quarks and vice-versa, with essentially no change in mass - a principle called *isospin invariance*. Isospin invariance demands a symmetry between the proton and neutron light quark densities

$$\begin{aligned} d(x) &\equiv d^p(x) = u^n(x) \quad , \quad u(x) \equiv u^p(x) = d^n(x), \\ \bar{d}(x) &\equiv \bar{d}^p(x) = \bar{u}^n(x) \quad , \quad \bar{u}(x) \equiv \bar{u}^p(x) = \bar{d}^n(x). \end{aligned}$$

Since nucleons do not exhibit net strangeness or charm, it is reasonable to assume

$$\begin{aligned} s(x) &\equiv s^p(x) = s^n(x) \quad , \quad c(x) \equiv c^p(x) = c^n(x), \\ \bar{s}(x) &\equiv \bar{s}^p(x) = \bar{s}^n(x) \quad , \quad \bar{c}(x) \equiv \bar{c}^p(x) = \bar{c}^n(x). \end{aligned}$$

Combining all of the above together, one can write parton densities for an isoscalar nucleon ( $\frac{1}{2}(\text{proton} + \text{neutron})$ ) in terms of *proton densities* as

$$\begin{aligned} q^{\nu N} &= \frac{1}{2} [u(x) + d(x) + 2s(x)], \\ \bar{q}^{\nu N} &= \frac{1}{2} [\bar{u}(x) + \bar{d}(x) + 2\bar{c}(x)], \\ q^{\bar{\nu} N} &= \frac{1}{2} [u(x) + d(x) + 2c(x)], \end{aligned} \quad (2.18)$$

$$\bar{q}^{\nu N} = \frac{1}{2} [\bar{u}(x) + \bar{d}(x) + 2\bar{s}(x)].$$

Substituting the above expressions into 2.16 yields

$$\begin{aligned} 2xF_1^{\nu N} &= x[u(x) + \bar{u}(x) + d(x) + \bar{d}(x) + 2s(x) + 2\bar{c}(x)], \\ 2xF_1^{\bar{\nu} N} &= x[u(x) + \bar{u}(x) + d(x) + \bar{d}(x) + 2\bar{s}(x) + 2c(x)], \\ xF_3^{\nu N}(x) &= xu_V(x) + xd_V(x) + 2xs(x) - 2x\bar{c}(x), \\ xF_3^{\bar{\nu} N}(x) &= xu_V(x) + xd_V(x) - 2x\bar{s}(x) + 2xc(x). \end{aligned} \tag{2.19}$$

where  $u_V \equiv u - \bar{u}$  and  $d_V \equiv d - \bar{d}$  are the proton's so-called valence densities that obey the baryon conservation conditions

$$\begin{aligned} \int (u - \bar{u})dx &= 2, \\ \int (d - \bar{d})dx &= 1. \end{aligned} \tag{2.20}$$

## 2.5 LO QCD Charm Production

At the hadronic vertex a charm quark can be produced only from  $d$  and  $s$  quarks in neutrino interactions and from  $\bar{d}$  and  $\bar{s}$  quarks in anti-neutrino interaction. Therefor one writes structure functions, for charm production for zero charm mass, as

$$\begin{aligned} 2xF_1^\nu &= xF_3 = |V_{cd}|^2[xu(x) + xd(x)] + |V_{cs}|^2 2xs(x), \\ 2xF_1^{\bar{\nu}} &= -xF_3^{\bar{\nu}} = |V_{cd}|^2[x\bar{u}(x) + x\bar{d}(x)] + |V_{cs}|^2 2x\bar{s}(x). \end{aligned} \tag{2.21}$$

The charm quark mass  $m_c$  is not negligible compared to the average momentum transfer  $Q^2$  in NuTeV. If a massless quark carrying momentum fraction  $\xi p$  interacts with a W-boson with momentum  $q$ , the 4-momentum conservation requirement in Eq.2.3 is modified to

$$(\xi p + q)^2 = m_c^2 \tag{2.22}$$

Solving the above equation for  $\xi$  and neglecting second order terms in  $M/Q$ , one obtains

$$\xi = x(1 + \frac{m_c^2}{Q^2}). \quad (2.23)$$

The variable  $\xi$  is known, for historical reasons, as the slow rescaling variable and should be substituted for  $x$  into structure functions on the right-hand side of Eq.2.21. Substituting Eq.2.21 into Eq.2.12, and switching from  $x$  to  $\xi$  one finally arrives to the charged current charm production cross-sections

$$\begin{aligned} \frac{d^2 \sigma^{(\nu N \rightarrow c \mu^-)}}{d\xi dy} &= \xi \left\{ [u(\xi) + d(\xi)] |V_c d|^2 + 2s(\xi) |V_c s|^2 \right\} \\ &\quad \times (1 - y + \frac{xy}{\xi} - \frac{Mxy}{2E}), \\ \frac{d^2 \sigma^{(\bar{\nu} N \rightarrow \bar{c} \mu^+)}}{d\xi dy} &= \xi \left\{ [\bar{u}(\xi) + \bar{d}(\xi)] |V_c d|^2 + 2\bar{s}(\xi) |V_c s|^2 \right\} \\ &\quad \times (1 - y + \frac{xy}{\xi} - \frac{Mxy}{2E}). \end{aligned} \quad (2.24)$$

The multiplicative factor  $1 - y + \frac{xy}{\xi} - \frac{Mxy}{2E}$  emerges from keeping terms proportional to  $m_c$  and  $M$ .

## 2.6 Next-to-Leading Order Charm Production

Formula 2.24 describes neutrino scattering only from target's quarks. It corresponds to the Feynmann diagram in Fig.2.2 on the far left. On the same figure, it is shown that charm can be produced via other higher order processes. Perturbative QCD permits calculation of transition probabilities as a Taylor expansion in terms of strong coupling constant  $\alpha_s$ .

The quark-initiated diagram is the lowest order in  $\alpha_s$  order term and is called leading order (LO). The rest of the diagrams on Fig.2.2 are of order  $\alpha_s^2$  and all together are called next-to-leading order diagrams (NLO). In NuTeV we observe the dimuon final state. This means that first the charm quark has to be produced, after it charm quark has to recombined with one of the anti-quarks turning most

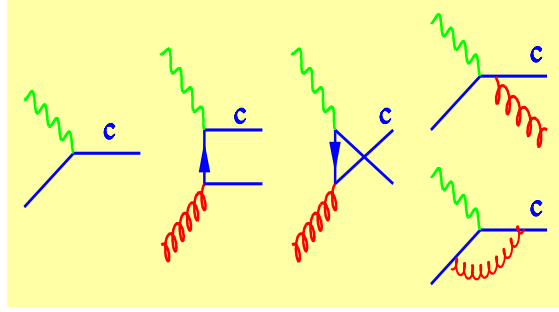


Figure 2.2: LO and NLO Feynmann diagrams.

of the time into D-meson, and at the end D-meson has to decay weakly. In LO the probability of that happening can be factorized and written down as the product of three different probabilities: production, fragmentation, and decay. In NLO dimuon production, probability does not factorize and fragmentation must be convoluted with the charm production cross section.

## Chapter 3

# E815 Experimental Apparatus

This chapter describes the NuTeV beamline, detector, and calibration beam.

### 3.1 The Sign Selected Neutrino Beam

NuTeV uses a beamline constructed in order to enable separate running in neutrino or anti-neutrino mode. NuTeV’s detector is essentially the same as that used by a series of earlier neutrino experiments collectively referred to as “CCFR”. In both experiments neutrinos and anti-neutrinos were produced as the result of pion ( $\pi$ ) and kaon ( $K$ ) decays, particles produced in collisions of 800 GeV protons with a beryllium oxide target (BeO) at the Tevatron (Fig.3.1). The BeO target is chosen because of its thermal and structural properties, and because low-Z materials are more efficient in producing neutrinos. NuTeV’s beamline features the Sign-Selected Quadrupole Train (SSQT) shown in Fig.3.2. Dipole magnets were always set up so that only  $\pi$ ’s and  $K$ ’s of a particular sign would pass through the SSQT. Quadrupole magnets then focus the remaining charged particle beam. Positively charged particles decay into neutrinos while negatively charged particles decay into anti-neutrinos. This knowledge greatly enhances NuTeV capability of identifying primary and secondary muons in dimuon events. In  $\nu$  mode the

contamination of  $\bar{\nu}$  was  $\bar{\nu}/\nu = 0.8 \times 10^{-3}$ . In  $\bar{\nu}$  mode, the ratio  $\nu/\bar{\nu} = 4.8 \times 10^{-3}$ .

After traveling through the magnets in Fig.3.2 the beam consist of  $\pi$ 's and  $K$ 's of a particular sign with mean energy of about 250 GeV. These particles travel through a 320 m decay pipe where approximately 5% of them decay into a muon and a neutrino (or anti-neutrino). After the decay pipe, a 915 m berm consisting of iron and earth stops muons from entering the NuTeV detector, leaving only neutrinos from the primary beam. Some neutrinos actually interact in the berm producing secondary muons called straight through muons that are used for alignment and calibration.

The Tevatron sends  $10^{12}$  protons to the BeO target in short bursts of 4 ms long "pings". The period of time during which neutrinos arrive at NuTeV detector is called the neutrino, or fast gate. In 60 seconds there are 4 or 5 fast gates. The remainder of the 60 seconds is called the slow gate, during which calibration data and cosmic ray events for background studies are recorded in the detector. The timing of the Tevatron beam is shown in Fig.3.3.

### 3.2 Lab E Detector

The NuTeV detector, shown in Fig.3.4, is approximately  $3 \times 3$  m<sup>2</sup> across and 28 meters long; it weighs over 1000 tons. The detector consists of two major parts: the target calorimeter and the toroid muon spectrometer. The muon spectrometer measures the momentum of muons, and the calorimeter measures the energy of hadron shower as well as a part of the muon energy deposited by traveling through the calorimeter, the position of the interaction, and the primary and secondary muon scattering angles. The calorimeter has a basic repeating structure of an iron sheet and scintillation counter. Details of the detector can be found in several places [29].

The energy of hadrons (muons) in the calorimeter is measured by liquid scin-

tillation counters. A hadron or a muon ionizes particles in the liquid scintillator which results in emission of a number of photons that are collected and counted by phototubes positioned at the four corners of the counter. The un-amplified response from each phototube is called the *low*. The combination of all *lows* from a counter is amplified by 100 and piped through a discriminator. The discriminator threshold is set to 150 mV, which is approximately 1/4 of an energy of a minimum ionizing particle (MIP). The resulting signal is called an s-bit. S-bits are used to find muons in the detector. Each *low* is amplified by 10 and sent to an adc counter as *high*. *Highs* are used to define the relationship between muon energy loss and phototube response, called a MIP (minimum ionizing particle), the standard unit of energy in the calorimeter. *Lows* from all counters in the area of the hadron shower are translated then into hadronic energy. The hadron energy resolution is measured in test beam data to be

$$\frac{\sigma_E}{E} = 0.024 \oplus \frac{87.4\%}{\sqrt{E}} \oplus \frac{4.38 \times 10^{-6}}{E}. \quad (3.1)$$

The hadron energy scale uncertainty is measured with the testbeam to be 0.5% [29].

The muon energy is measured by the calorimeter ( $dE/dx$ ) and the muon spectrometer ( $E_{\mu ff}$ ). When a muon flies through the calorimeter it loses energy that is measured by translating the response of scintillation counters that are outside of the hadron shower into deposited energy. Since a muon is a charged particle it bends when it passes through the toroid. The energy of the muon when it enters the front face of the toroid ( $E_{\mu ff}$ ) is calculated from its curvature. Of course, a muon also loses some energy when it travels through the toroid. The toroid resolution, dominated by multiple Coulomb scattering, is measured to be  $\frac{\Delta E_{\mu ff}}{E_{\mu ff}} = 11\%$ . The  $dE/dx$  usually is significantly smaller than  $E_{\mu ff}$  and is known much better than 11%. The result is that  $\frac{\Delta E_{\mu}}{E_{\mu}} = 11\%$ . The muon scale uncertainty is measured with the testbeam to be 1% [29].

The toroid also provides information about the charge of a muon. The SSQT always leaves  $\pi$ 's or  $K$ 's of a designated sign. Positively charged particles decay into neutrinos, and negatively charged ones decay into anti-neutrinos. Neutrino



charged-current interactions have negatively charged muons at the primary vertex and anti-neutrinos produce positively charged muons. The magnet polarity is always chosen (focusing mode) so that the muon from primary vertex has a positive curvature or, in other words, bends inwards in the toroid as is shown in Fig.1.3. In the case of dimuon production, the secondary muon has the opposite charge from the primary muon which always has a positive curvature. Thus the identification of the primary and secondary muons for dimuon events is easy and straightforward. Measuring one sign is enough.

The toroid consists of three sets of toroid magnets separated from each other by a set of drift chambers. Drift chambers are responsible for muon track reconstruction. Each chamber region is called a gap. A drift chamber is a device that measures the position of a charged particle track. It consists of parallel wires exposed to high electric potential. The charged particle, passing through a drift chamber, ionizes gas inside it. Electrons, that are the result of the ionization, drift in the electric field to the charged wire with a constant drift velocity. Their arrival time permits an accurate calculation of the charged particle's position in one dimension, so two adjacent orthogonal drift chamber planes are used to determine the x-y position.

At every moment in time, the data acquisition system (DAQ) reads in information from all parts of the detector and continuously writes it to the computer storage device. There are several general event types that might happen in the detector each resulting in a unique signal pattern. These patterns are recognized and information is stored under so called "triggers". All triggers are listed in Table 3.1. For this analysis all events are collected under Trigger 1, which is designed to recognize charged current events. Trigger 1 events have the following topology: the event must happen within the fast gate; the veto wall (an array of solid scintillation counters) in front of Lab E must not fire, meaning that it is not a straight through muon; the vertex must lie well downstream of the first counter; and the muon must fire two s-bits out of last four counters and be recorded in both of the

first two gaps in the toroid. If the muon does not penetrate to the second gap, it must fire two s-bits in counters from 9 to 12 (counter 1 is the closest to the toroid).

### **3.3 Calibration Beam**

In order to translate scintillation counter response into actual energy the calibration beam is used. The idea is to send particles of known energies into the detector and to map the detector response to the energy. The calibration beam delivered beams of hadrons, electrons and muons of known energy over the range 5-200 GeV [29]. The layout is shown on Fig.3.5. The set-up allows one to distinguish between different types of particles, to select particles of a particular energy, and to measure each particle's momentum vector. Calibration beam information is used to tune the simulated detector response. The procedure for tuning muon and hadron energies is discussed later.

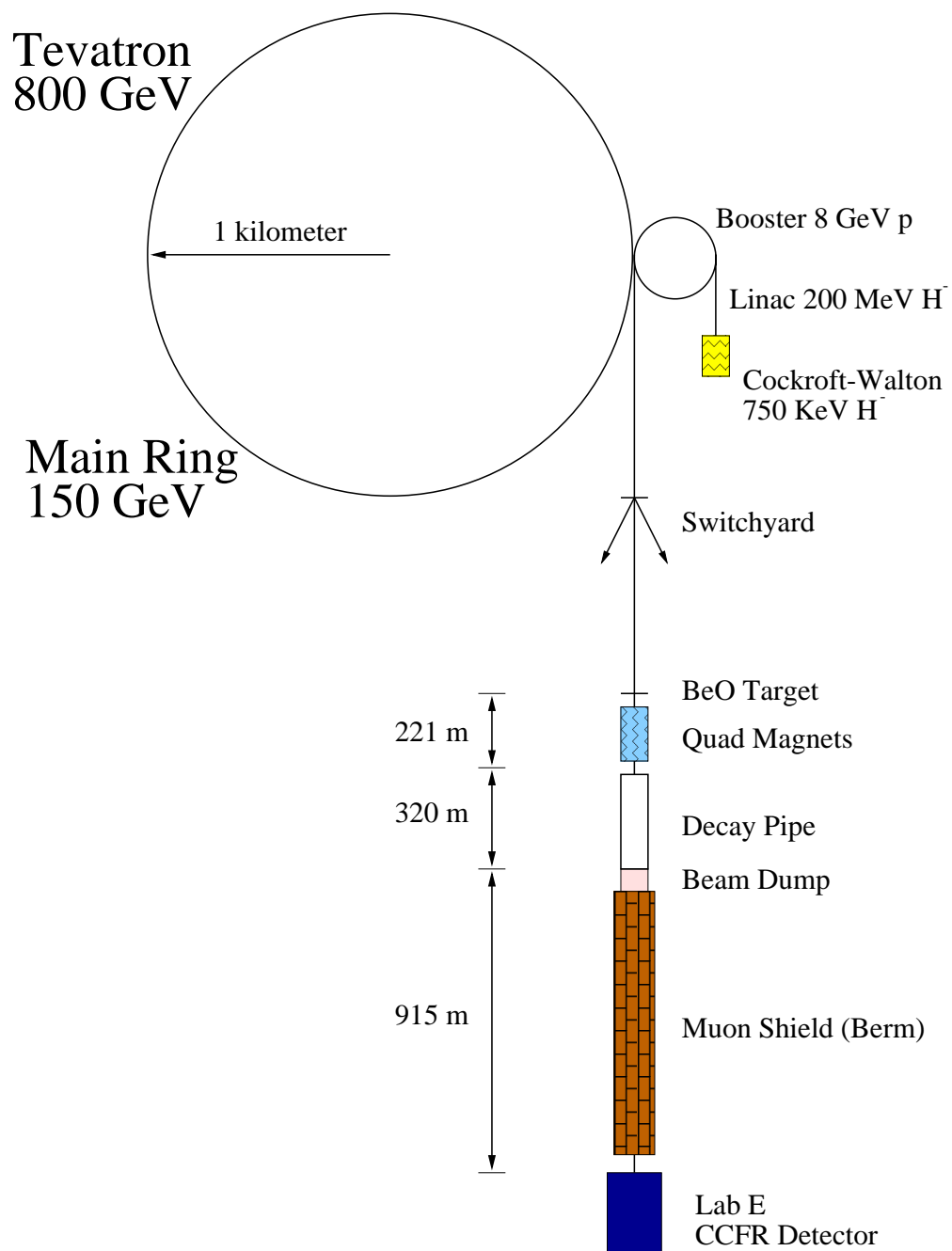


Figure 3.1: The Fermilab Tevatron and neutrino-beamline.

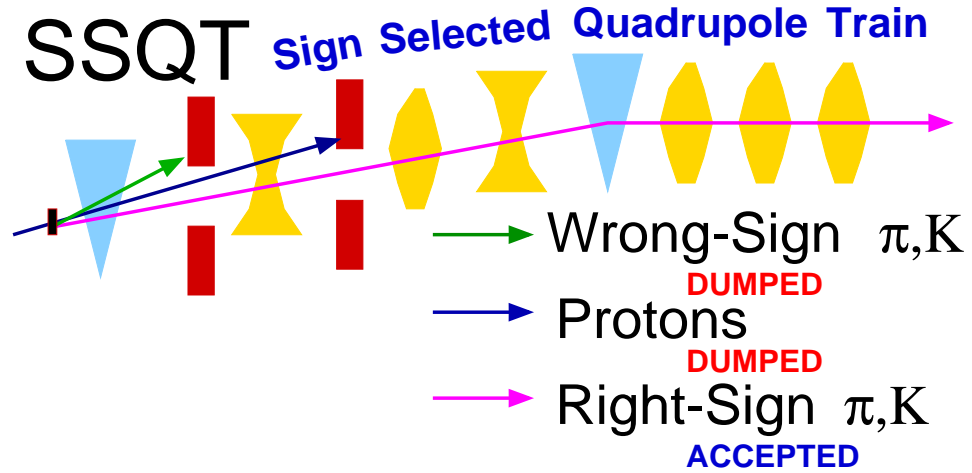


Figure 3.2: The SSQT beamline.

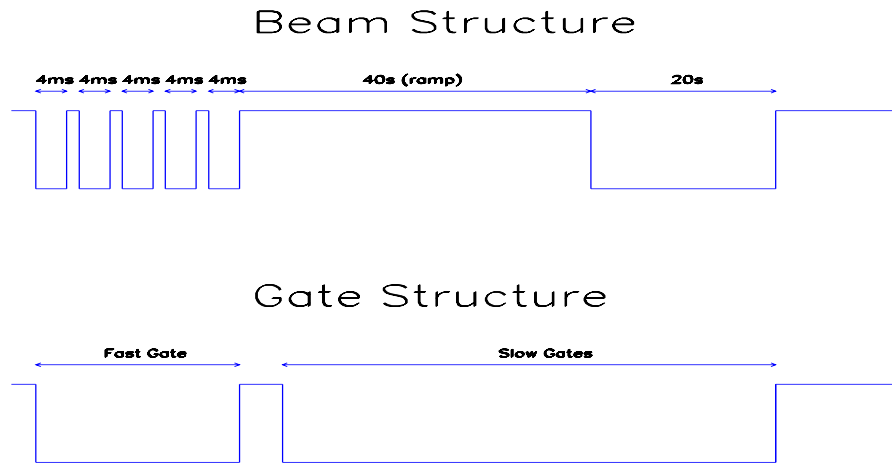


Figure 3.3: Schematic diagram of beam timing structure

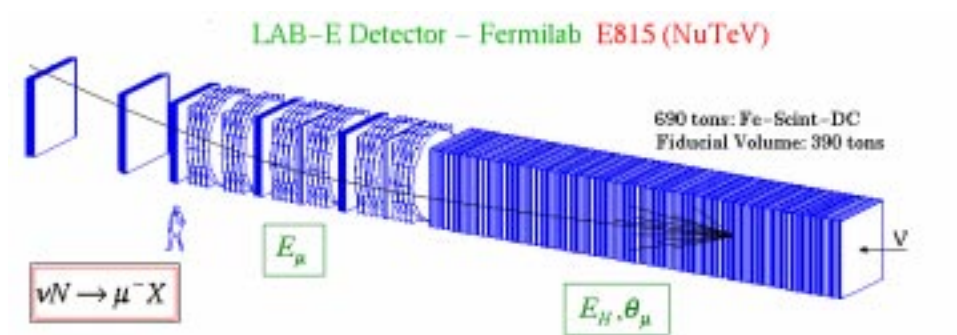


Figure 3.4: The Lab E detector.

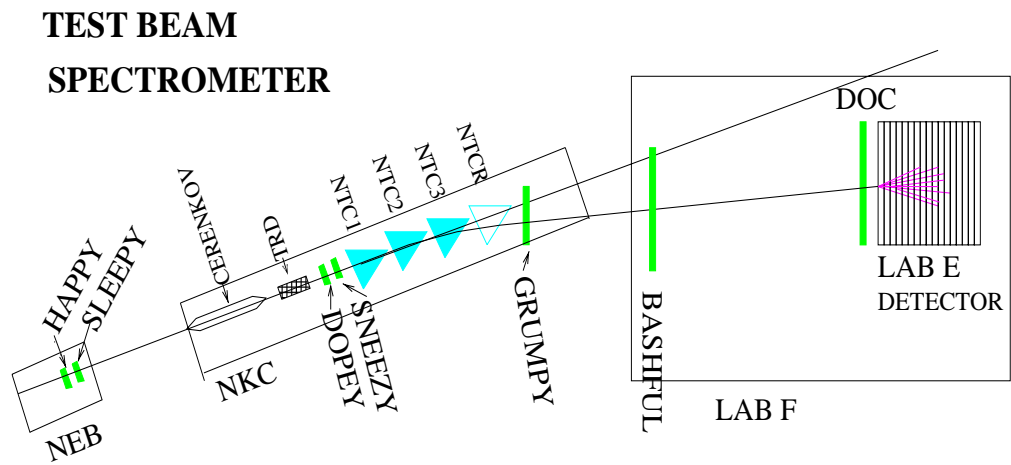


Figure 3.5: The NuTeV Testbeam spectrometer.

<i>Trigger</i>	<i>Name</i>	<i>Requirements</i>
1	Charged Current Trigger	<ul style="list-style-type: none"> <li>• counters on upstream of washer 1</li> <li>• counters on in both toroid gaps</li> <li>• no upstream veto</li> </ul>
2	Neutral Current Trigger	<ul style="list-style-type: none"> <li>• <math>E_{had} &gt; 5</math> GeV in 8 consecutive counters</li> <li>• <math>E_{had} &gt; 0.15</math> GeV in 2 out of 4 consecutive counters</li> <li>• no upstream veto</li> </ul>
3	Range-Out/Exit Trigger	<ul style="list-style-type: none"> <li>• 1/4 MIP in each of 16 non-consecutive counters</li> <li>• 4 GeV energy in any 8 adjacent counters</li> <li>• no upstream veto</li> </ul>
4	Charged Current Trigger II	<ul style="list-style-type: none"> <li>• shower energy</li> <li>• hits in first cart upstream of toroid</li> <li>• muon track through one toroid quadrant</li> </ul>
5	Test Beam Trigger	<ul style="list-style-type: none"> <li>• slow spill</li> </ul>
6	Straight through $\mu$ Trigger	<ul style="list-style-type: none"> <li>• hits in each cart and one toroid quadrant</li> </ul>
8	Cosmic Ray Trigger	<ul style="list-style-type: none"> <li>• 40 counter muon requirement</li> </ul>
10,11,12	Pedestal Triggers	<ul style="list-style-type: none"> <li>• No other triggers</li> </ul>

Table 3.1: NuTeV trigger list with descriptions

## Chapter 4

# The Dimuon Data Sample

NuTeV collected almost four million events with a detector signature consistent with a charged-current event. Various selection criteria (cuts) are applied to the data to remove improperly reconstructed events, overlayed or multiple events, background events, and other anomalies. Charged-current cuts identify single muon events. To select dimuon events out of all charged-current events, additional cuts on the second muon are applied. Since data is going to be compared with Monte Carlo simulation, cuts also are designed to remove events that cannot be properly simulated. This chapter describes the charged-current data and dimuon data selection criteria.

### 4.1 Charged-current Data Selection

The charged-current event is easily recognized by the localized deposition of hadronic energy accompanied by an outgoing muon track or tracks. Various cuts are applied to ensure that the event has occurred in time with the neutrino beam (fast gate), is well inside the fiducial volume of the detector, is properly reconstructed by the detector, and can be simulated by the Monte Carlo. The following cuts are used to select charged-current events:

1. The event must occur in coincidence with the beam (fast gate) and fire the charged current trigger.
2. The incident neutrino energy,  $E_\nu$ , must be greater than 20 GeV and the energy of the hadronic shower,  $E_{had}$ , greater than 10 GeV.
3. In order to ensure event containment, only events occurring within an active fiducial volume are accepted: the transverse vertex positions ( $V_x, V_y$ ) must satisfy  $-127 \text{ cm} < V_{x,y} < 127 \text{ cm}$  and  $\sqrt{V_x^2 + V_y^2} < 152.4 \text{ cm}$ , while the longitudinal vertex position must lie between counters 20 and 80, which corresponds to 2.7 and 17.7 hadronic interaction lengths from the upstream and downstream ends of the calorimeter, respectively.
4. The time obtained from fitting the primary muon track must be within 36 ns of the trigger time.
5. The muon must be toroid-analyzed with muon energy on the front face of the detector  $E_{\mu ff} > 3 \text{ GeV}$ .
6. The muon must pass through at least 2/3 of the toroid.
7. The muon must hit the front face of the toroid inside a circle of radius  $R_{FF} < 152 \text{ cm}$ , and more than 80% of the path length of the muon must be in the toroid steel.
8. Finally, in order to remove mis-reconstructed events, a requirement is imposed on the reconstructed  $x_{vis}$  kinematic variable:  $0 \leq x_{vis} \leq 1$ .

## 4.2 Dimuon Data Selection

A typical dimuon event is shown in Fig.1.5. In this figure, the toroid can be seen to focus the leading muon originating from the leptonic vertex and to de-focus the secondary muon which originates most probably from charm decay. In the event shown in the figure, both muons pass through the toroid, and both of their signs



are determined. For events where the sign of one muon is not measured, it is assumed to be the opposite of the one measured. Since the charge of the primary muon is always known, the measurement of the sign of only one muon is sufficient to identify the primary and secondary muons in the event. The rate of the same sign dimuon events with both muons toroid-analyzed is very low [28]. Cuts used to select the dimuon sample consist of the following:

1. The event must occur in coincidence with the fast gate and fire the charged current trigger.
2. The incident neutrino energy must be greater than 20 GeV and the energy of the hadronic shower,  $E_{had}$ , greater than 10 GeV.
3. In order to ensure event containment, only events occurring within an active fiducial volume are accepted: the transverse vertex position  $(V_x, V_y)$  must satisfy  $-127 \text{ cm} < V_{x,y} < 127 \text{ cm}$  and  $\sqrt{V_x^2 + V_y^2} < 152.4 \text{ cm}$ , while the longitudinal vertex position must lie between counters 15 and 81, which corresponds to 2.7 and 13.3 hadronic interaction lengths from the upstream and downstream ends of the calorimeter, respectively. The place requirement is relaxed compared to the charged current cut in order to gain statistics. Dimuon events tend to have smaller hadronic energy, so the shower is still well-contained in the detector.
4. Two muons must be identified in the event and satisfy the following criteria:
  - The energy of both muons,  $E_{\mu 1, \mu 2}$  must be greater than 5 GeV.
  - The time obtained from fitting each track must be within 36 ns of the trigger time.
  - One of the muons must be toroid-analyzed. The energy of the primary muon at the entrance of the toroid greater than 5 GeV.
  - At least one toroid-analyzed muon must pass through at least 2/3 of the toroid.

- The toroid-analyzed muons must hit the front face of the toroid inside a circle of radius  $R_{FF} < 152$  cm, and more than 80% of the path length of the muon must be in the toroid steel.
5. Finally, in order to remove mis-reconstructed events, a requirement is imposed on the reconstructed  $x_{vis}$  kinematic variable:  $0 \leq x_{vis} \leq 1$ .

The final dimuon event sample contains 5102  $\nu_\mu$  induced and 1458  $\bar{\nu}_\mu$  induced events. Of these, 2280/655 in  $\nu_\mu/\bar{\nu}_\mu$  mode have both muons reconstructed in the toroid spectrometer. All other events have only one. The mean  $E_{vis}$  of the events is 157.8 GeV, the mean  $Q_{vis}^2 = 21.1$  GeV<sup>2</sup> and the mean  $x_{vis} = 0.14$ . The overall reconstruction efficiency, including detector acceptance, is  $\sim 60\%$  for events with  $E_{\mu 2} \approx 5$  GeV, and  $\sim 80\%$  when  $E_{\mu 2}$  is above 30 GeV, as shown on Fig.4.1

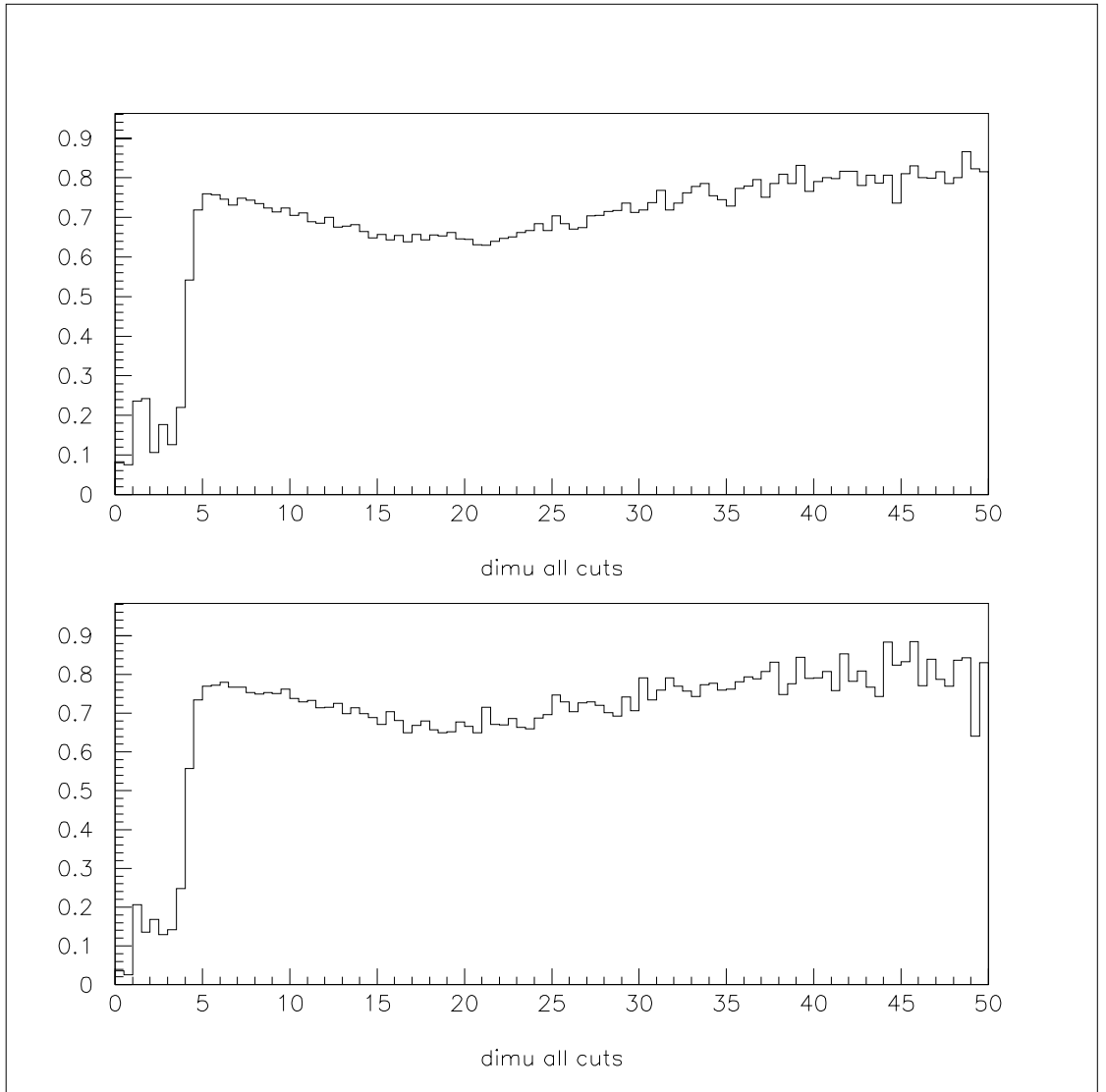


Figure 4.1: Total reconstruction efficiency as a function of second muon generated energy.

## Chapter 5

# Monte Carlo Simulation

In neutrino-nucleon scattering many stochastic processes are involved both in the basic physics and in the response of the detector. It is impossible to describe observed processes by simple analytical formulas. Instead, a detailed simulation of the NuTeV experiment is performed using the Monte Carlo (MC) technique. The first part of Monte Carlo simulation involves generation of an event's kinematics according to a specific physical model. The second part is the propagation of the single muon or dimuon events through the detector. The end result of the MC simulation is a set of events that look like real data events. A fit can then be performed of MC sample to the data by varying physics model parameters. The MC sample must be statistically superior to the real data sample to ensure numerical accuracy.

In this analysis, two different Monte Carlo samples are used. A single muon MC sample is used to correct for the neutrino flux and to normalize the dimuon rate to the total charged current rate. The generation begins with randomly selecting (throwing) values for kinematic variables that determine the charged current cross section. Next, another random number is thrown in the range between zero and the maximum value the cross section can have. If this number is less than the cross section value (from Eq.2.12) for the already selected kinematics, then we keep the

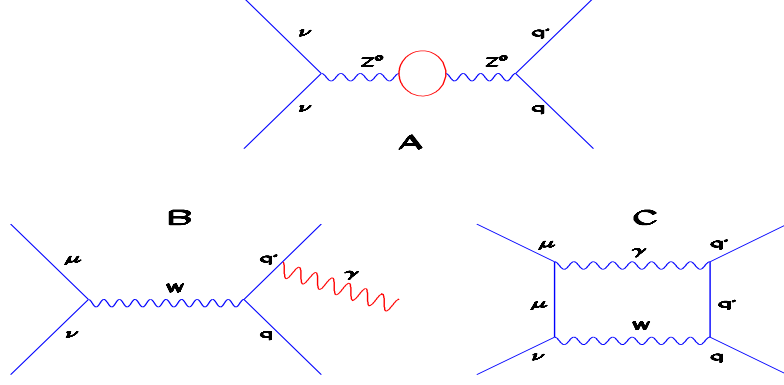


Figure 5.1: Radiative correction diagrams. A) Boson loop correction. B) Boson radiation from final state quark. C) Box diagram.

event. Otherwise, the event is discarded. The dimuon MC sample is used in a fit to the dimuon data to extract model parameters sensitive to charm production. The dimuon MC sample is generated separately from charged current sample. Each MC event is assigned a weight that is the ratio of dimuon cross-section to charged current cross-section.

$$Weight = \frac{\sigma_{2\mu}(E_\nu, x, q^2)}{\sigma_{1\mu}(E_\nu, x, q^2)}. \quad (5.1)$$

The fitting procedure then operationally consists of varying the weight.

## 5.1 Detector Simulation

A hit-level Monte Carlo simulation of the detector based on the GEANT package [30] was used to model the detector response and provide an accurate representation of the detector geometry. Monte Carlo events were analyzed using the same reconstruction software used in the data analysis. The detector response in the simulation was tuned to both hadron and muon test beam data at various energies. To ensure accurate modeling of the muon reconstruction efficiency, the drift chamber efficiencies were measured in the data as a function of time and implemented in the simulation.

Primary neutrino interactions were generated using the LO QCD model and

fragmentation function described more fully in Sec. 6.1. The cross section model in Eq.2.12 does not account for electroweak radiation processes: loop corrections to the boson propagation,  $\gamma/Z^0/W^\pm$  radiation from the final state quark, and the  $\gamma$  radiation from the primary vertex muon (Fig.5.1). Electroweak radiative corrections based on the model by Bardin [31] were applied to this cross-section. The main background to charm arises from ordinary CC interactions in which a pion or kaon produced in the hadronic shower decays muonically. This was simulated following a parameterization of hadron test beam muon-production data for simulating secondary decays, and the LEPTO [32] package for the decays of primary hadrons [33]. The total probability to produce such muons with momentum greater than 4 GeV/c is  $\approx 2 \times 10^{-4}$  for events with  $E_{had} \sim 30$  GeV, and  $\approx 10^{-3}$  for  $E_{had} \sim 100$  GeV. The contribution from the primary hadron decays is roughly two times larger than that from the secondary decays.

To make sure that the detector response is properly simulated the calibration beam data is used to correct for apparent muon and hadron energy biases, or “pulls”. Since the true energy of each muon or hadron is measured separately one should look at the detector response by measuring energy of a particle by the detector and comparing it to the true value. The same response should be observed in Monte Carlo simulation of the calibration beam. To correct for an apparent muon energy pull the procedure described below is used.

In order to make sure that the detector energy response is properly simulated a calibration beam (test beam (TB)) of muons for a particular energy  $E_{gen}$  is selected and for each event the ratio of the reconstructed energy  $E_{rec}$  to the generated energy of the muon. The result is an asymmetric Gaussian distribution with the mean  $Mean_{tb}$  and width  $Width_{tb}$ . NuTeV collected muon and hadron calibration beam over a wide range of energies. By using all calibration beam energies functions  $Mean_{tb}(E_{gen})$  and  $Width_{tb}(E_{gen})$  are measured. Monte Carlo simulation are then used to calculate similar functions  $Mean_{mc}$  and  $Width_{mc}$ . If mean and width MC functions do not agree with those obtained for the test beam over some  $E_{gen}$

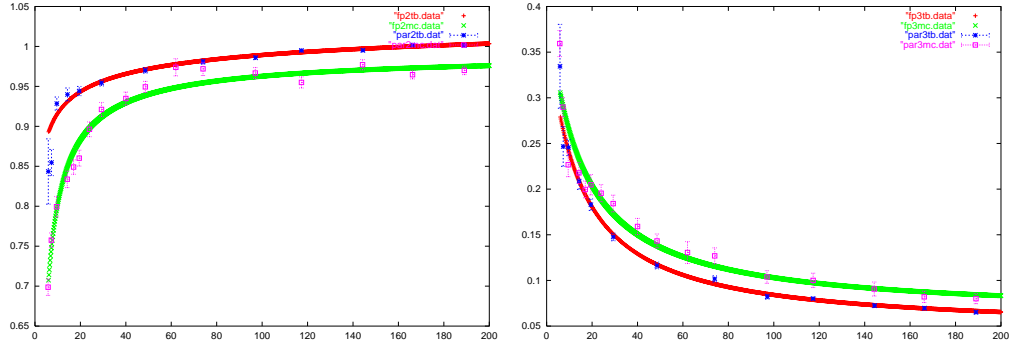


Figure 5.2: The *Mean* (left) and the *Width* (right) of Gaussian fits (Fig.5.5) as functions of the generated hadron energy both for the test beam and Monte Carlo. The darker curves represent the test beam.

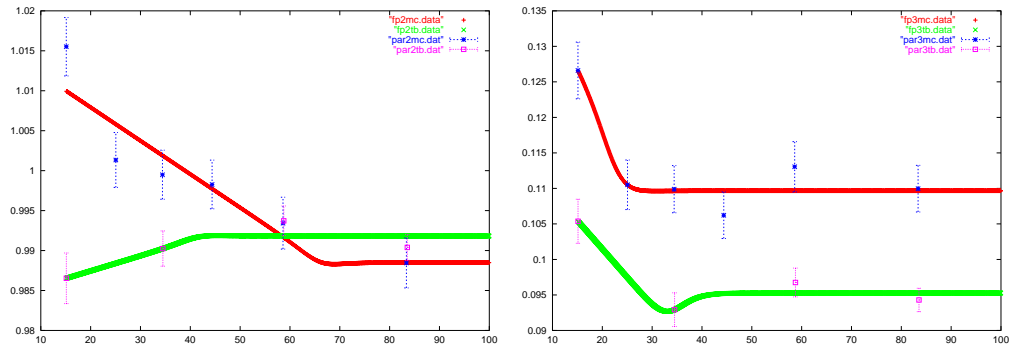


Figure 5.3: The *Mean* (left) and the *Width* (right) of Gaussian fits (Fig.5.5) as functions of the generated muon energy both for the test beam and Monte Carlo. The darker curves represent the test beam.

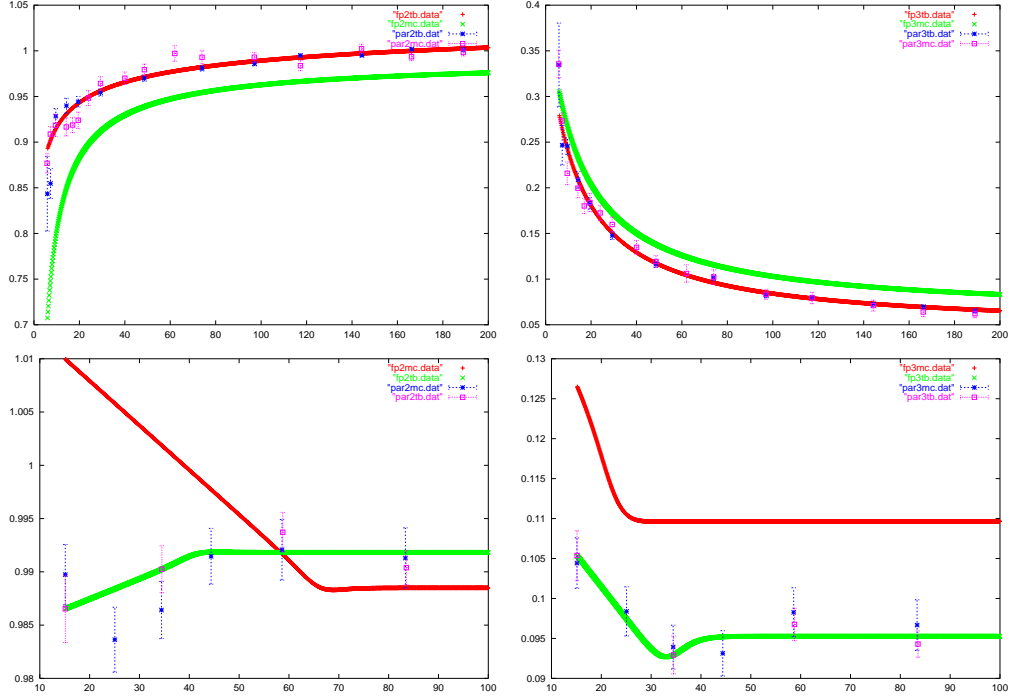


Figure 5.4: *Mean* and *Width* distributions from Fig.5.3 after corrections.

range then a correction for a reconstructed energy (calibration function) is found to enforce the agreement. The same procedure is used to tune the detector response for hadrons. Calibration curves for the mean and the width as a function of energy are shown on Figs.5.2-5.3.

Figures 5.2-5.3 show that the calibration corrections are non-unity for muons and hadrons. The calibration function shifts reconstructed energy by as little as possible to force the Monte Carlo Gaussian to lie on top of calibration beam Gaussian. It turns out that it is possible to adjust the mean and the width simultaneously by using

$$E'_{rec} = E_{gen} \left[ \left( \frac{Width_{tb}}{Width_{mc}} \left( \frac{E_{rec}}{E_{gen}} - Mean_{mc} \right) + Mean_{tb} \right) \right]. \quad (5.2)$$

The result of applying the energy corrections is shown on Fig.5.4. As a result of changing the reconstructed energy in the Monte Carlo according to formula 5.2, MC points move to the calibration beam curves. Figure 5.5 shows the effect of applying formula 5.2 to the Gaussian for the case of two different hadron energies.



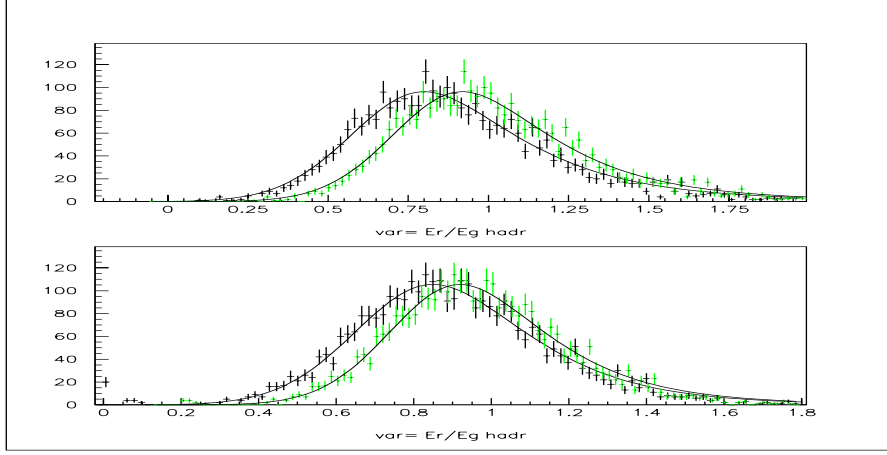


Figure 5.5: Gaussian fits to the reconstructed ( $E_{rec}$ ) energy over generated ( $E_{gen}$ ) energy distribution for one of the hadron TB and MC runs.

It is important to notice that the shape of the distribution stays close to the original one.

For the hadron calibration, the exact form of the distributions on Fig.5.2 is

$$Mean = d(\pi_0 + (1. - \pi_0)/c),$$

$$Width = 1./(a \times x + b) + c,$$

$$\pi_0 = 1 - (x/a)^b,$$

The coefficients  $a$ ,  $b$ ,  $c$ , and  $d$  are summarized in Table 5.1. Similarly, for muons:

$$f = (1. - 1./(1. + \exp((x - m)/w))),$$

$$Mean = f + c'(a' + b'x)/(1. + \exp((x - m)/w)),$$

$$Width = f + c'(a' + b'x)/(1. + \exp((x - m)/w)),$$

and coefficients  $a'$ ,  $b'$ ,  $c'$ , and  $d'$  are given in Table 5.2.

For Monte Carlo hadron shower generation a very simple  $3\pi$  model is used. The total generated energy is divided equally between  $\pi^+$ ,  $\pi^-$ , and  $\pi^0$ . Charged pions constitute the hadronic part of the hadron shower, while  $\pi^0$  are responsible for electromagnetic part of the hadron shower. The hadron test beam for NuTeV always had  $\pi^-$ s, so the correction described above takes care only of one part of

<i>Mean</i>	<i>a</i>	<i>b</i>	<i>c</i>	<i>d</i>
Data	8.91881468	-0.338007016	1.15470893	1.05159627
MC	9.74683905	-0.627438616	1.30525602	1.032245
<i>Width</i>	<i>a</i>	<i>b</i>	<i>c</i>	<i>d</i>
Data	0.19817455	3.25553521	0.0411955189	0
MC	0.118763552	3.683011	0.0402142124	0

Table 5.1: Coefficients for *Mean* (top two rows) and *Width* hadronic energy distributions.

<i>Mean</i>	<i>a</i>	<i>b</i>	<i>c</i>	<i>m</i>	<i>w</i>
Data	0.983556751	0.000189849841	0.99127606	41	2
MC	1.01734759	-0.000436031151	0.989042201	66	2
<i>Width</i>	<i>a</i>	<i>b</i>	<i>c</i>	<i>m</i>	<i>w</i>
Data	0.116241194	-0.000733062922	0.0944287782	34	2
MC	0.149244577	-0.00146297376	0.108360651	22	2

Table 5.2: Coefficients for *Mean* (top two rows) and *Width* muon energy distributions.

the hadron shower. Another correction is applied in order to correct the fraction of a hadron energy that goes into electromagnetic part since the response of the detector to electromagnetic showers is measured to be  $\sim 8\%$  higher than that for hadronic shower [29]. Figure 5.6 shows the amount of a correction that is applied. This study relies heavily on the LUND [17] prediction. The NuTeV Monte Carlo curve is described by the formula

$$f(x) = 34862 - 16998 * x - 18244 * x^2,$$

and the Lund curve is

$$f(x) = 48423 - 79213 * x + 30774 * x^2,$$

where  $x$  is the ratio of electromagnetic part of the shower to the total shower energy.

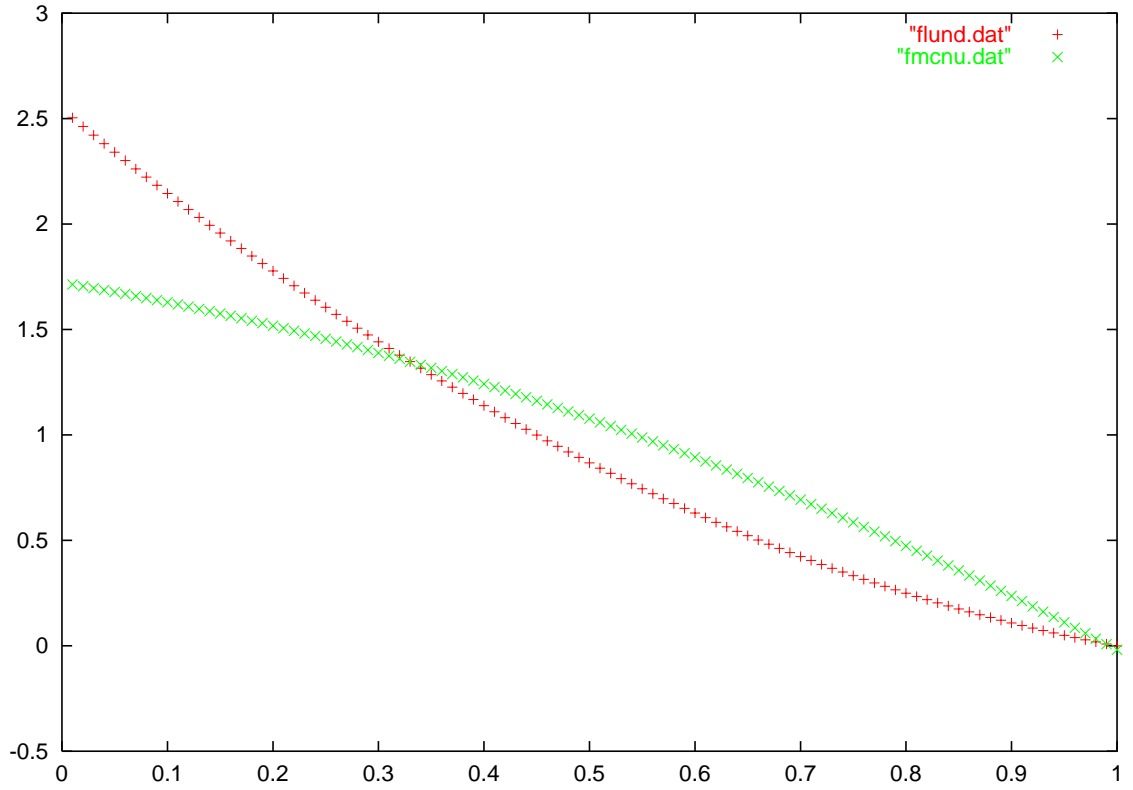


Figure 5.6: Unnormalized probability of the event as a function of the ratio of electromagnetic part to the total shower energy. Crosses -  $3\pi$  model, pluses - LUND prediction.

## 5.2 Neutrino Flux and Normalization

The total flux, energy spectra, and composition for both neutrino and anti-neutrino beams are calculated using a Monte Carlo simulation of the beamline based on the DECAY TURTLE program [34] and production data from Atherton [35] as parameterized by Malensek [36] for thick targets. This flux is used to generate an inclusive charged-current interaction Monte Carlo sample using the GEANT based hit level detector Monte Carlo described in section 5.1.

The predicted flux is then tuned so that the inclusive charged-current interaction spectra in the Monte Carlo match the data. Selection criteria for this sample of inclusive charged-current interactions are exactly the same as those used to select the dimuon sample with the requirement for 2 muons removed. Flux corrections of up to 15% are applied in bins of neutrino energy and transverse vertex position to force the single muon data and Monte Carlo to agree. In addition, an overall factor is determined for each beam (neutrino or anti-neutrino) that absolutely normalizes the single muon Monte Carlo to the data. The dimuon Monte Carlo uses the flux determined with the above procedure; and it is absolutely normalized to the inclusive single muon charged-current data through the flux tuning procedure.

The procedure used to tune the flux to the observed single muon rate is iterative since the event rate observed in the detector depends on the convolution of cross section with neutrino flux, and the result of the charm measurement has a small effect on the total cross-section. Corrections found from the single muon Monte Carlo/data comparisons are incorporated into the dimuon Monte Carlo that is used to determine the dimuon cross-section, and thus the charm production cross-section within our LO model. The charm cross-section results are then used in the single muon Monte Carlo, and the procedure is repeated until the flux parameters do not change (in practice the convergence is very fast). Figure 5.7 shows a comparison between data and Monte Carlo for the single muon (flux) sample; the level of agreement is very good.

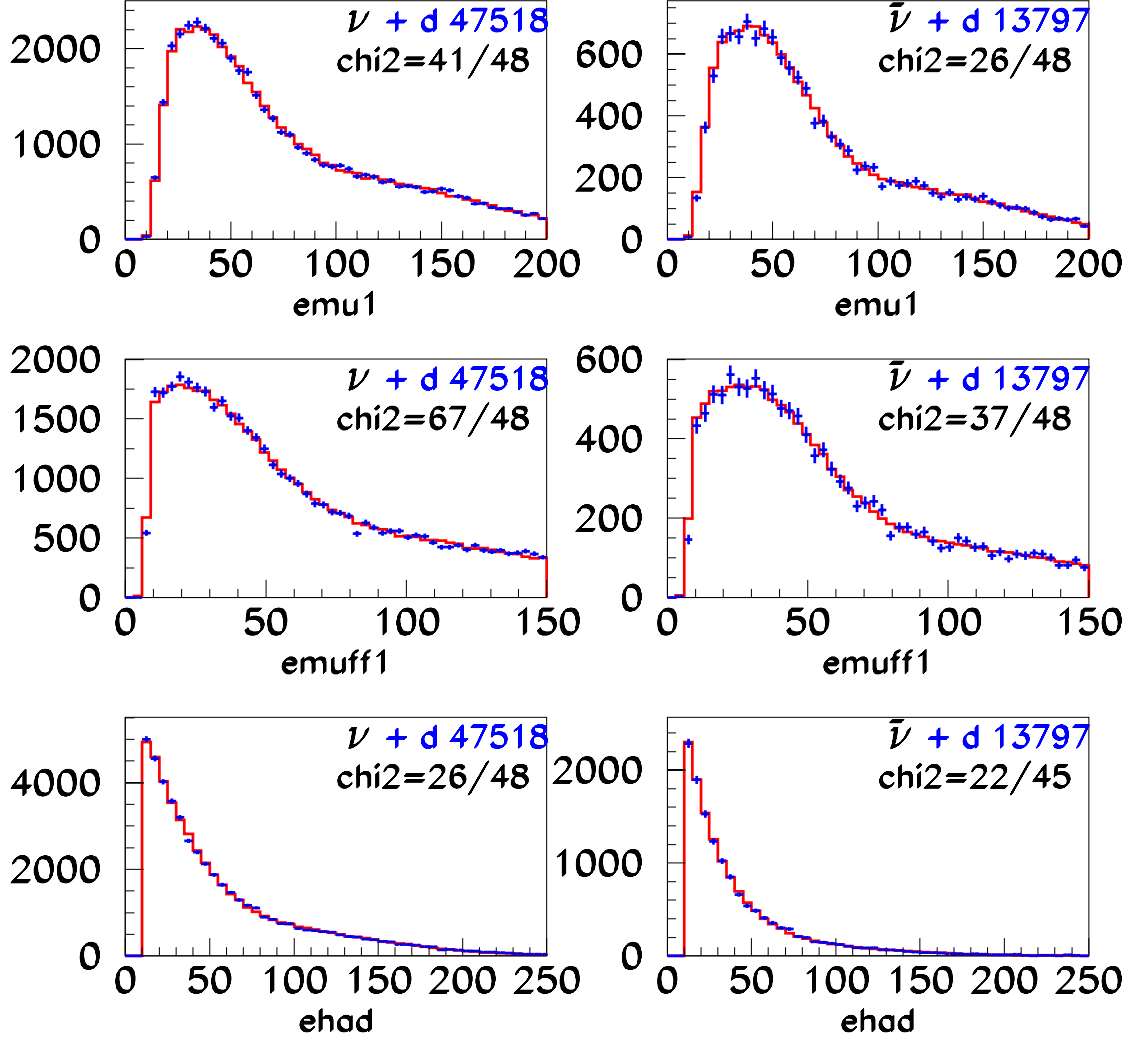


Figure 5.7: Top - total muon energy of the primary and secondary muons. Middle - muon energies at the front face of the toroid. Bottom - hadronic energy.  $\nu$  mode is on the left,  $\bar{\nu}$  mode is on the right.  $\chi^2$  per total number of degrees freedom is listed for each distribution. Pluses are data, histograms - Monte Carlo

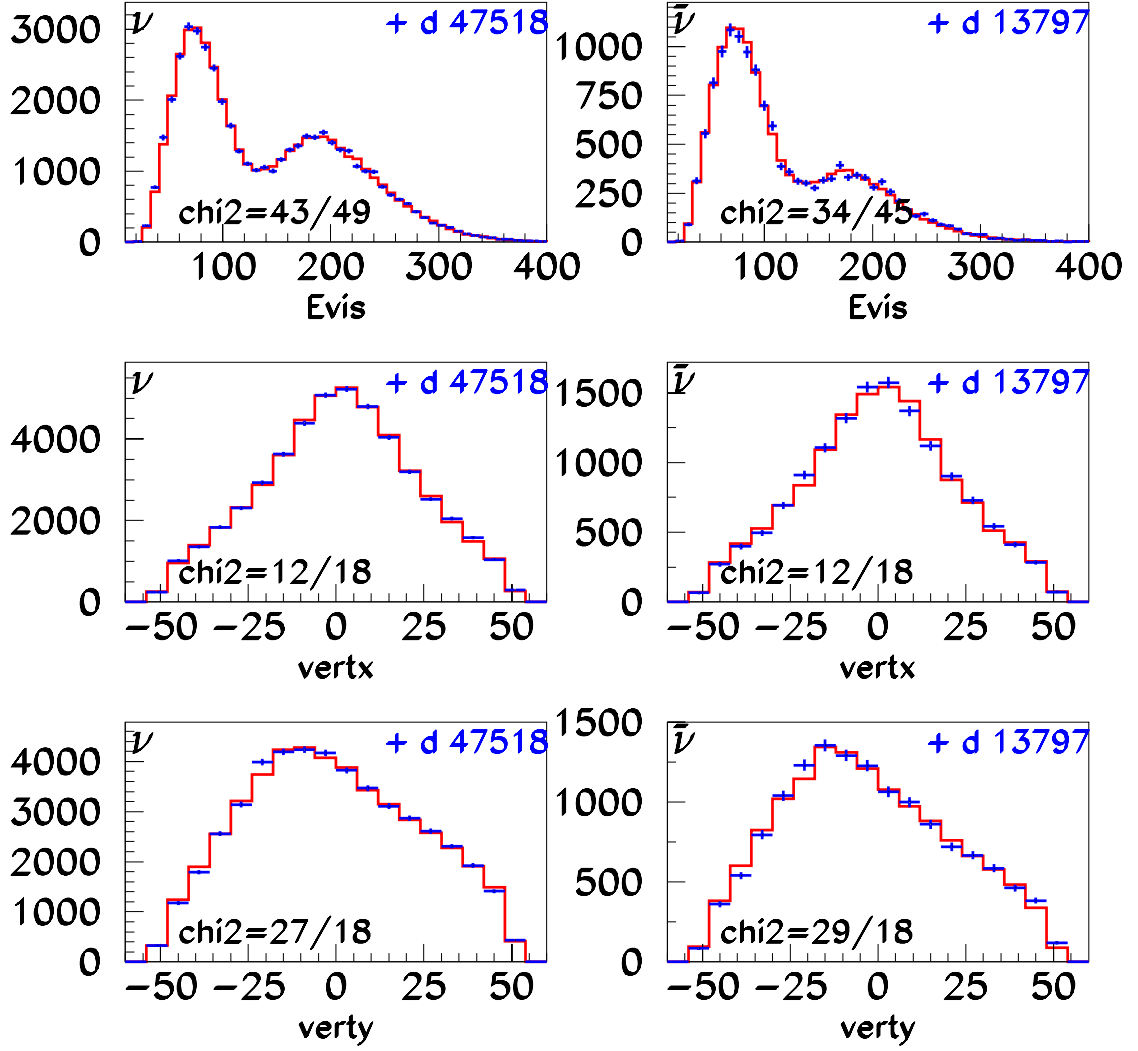


Figure 5.8: Top - visible neutrino energy. Middle - vertex distribution in x transverse plane. Bottom - vertex distributions in y transverse plane.  $\nu$  mode is on the left,  $\bar{\nu}$  mode is on the right.  $\chi^2$  per total number of degrees freedom is listed for each distribution. Pluses are data, histograms - Monte Carlo

## Chapter 6

# Dimuon Analysis Results

Dimuon data yield information about charm production models, charm quark fragmentation process, and the semi-muonic charm particle inclusive branching ratio decay  $B_c$ . In an ideal situation one would like to present direct measurements of the differential charm production cross sections  $d\sigma_c^{\nu(\bar{\nu})N}/dxdy$  at several different neutrino energies. NuTeV and its predecessor CCFR do not measure charm, but rather dimuons. The charm cross section is thus extracted from the data by model-dependent corrections for charm fragmentation and decay and by experimental effects of resolution, acceptance, and neutrino flux. One way of handling these issues is to fit a parametric model directly to the data and extract parameters from the model. This approach was used in the past for LO-QCD[22, 23, 24, 25] and NLO-QCD in the variable flavor ACOT[9] scheme[21].

### 6.1 General Fit Procedure

The approach taken here begins with the same idea, a LO-QCD parametric fit based on the following equation for dimuon production cross section:

$$\frac{d^3\sigma(\nu_\mu N \rightarrow \mu^- \mu^+ X)}{d\xi dy dz} = \frac{d^2\sigma(\nu_\mu N \rightarrow cX)}{d\xi dy} D(z) B_c(c \rightarrow \mu^+ X), \quad (6.1)$$

where first part on the right-hand side is the LO charm production cross section, second term is the fragmentation function, and the third term is the semi-muonic inclusive charmed hadron branching ratio. The expression 6.1 formally introduces the notion that, in LO QCD, the dimuon production cross section can be factored into three parts: production, fragmentation, and decay. The charm production cross section in LO QCD is

$$\left\{ \frac{d^2\sigma(\nu_\mu N \rightarrow cX)}{d\xi dy} \right\}_{LO} = \frac{G_F^2 M E_\nu}{\pi(1 + Q^2/M_W^2)^2} \left( 1 - \frac{m_c^2}{2ME_\nu\xi} \right) \times \quad (6.2)$$

$$\{ [\xi u(\xi, \mu^2) + \xi d(\xi, \mu^2)] |V_{cd}|^2 + 2\xi s(\xi, \mu^2) |V_{cs}|^2 \},$$

where  $\xi = x \left( 1 + \frac{m_c^2}{Q^2} \right) \left( 1 - \frac{x^2 M^2}{Q^2} \right)$  is a slow rescaling variable, with the second multiplicative taking into account target mass effects. Formulas 6.1 and 6.3 establish the set of physical parameters that can be measured by fitting dimuon Monte Carlo to the data. Parameters of interest are: the charm quark mass  $m_c$ , the semi-muonic branching ratio  $B_c$ , and the strange and anti-strange PDFs. It is also possible to obtain the parameter  $\epsilon$  that defines the Collins-Spiller fragmentation function [26]:

$$D(z, \epsilon) = [(1-z)/z + \epsilon(2-z)/(1-z)] (1+z)^2 [1 - (1/z) - \epsilon/(1-z)]^{-2}. \quad (6.3)$$

The fragmentation function describes the process in which produced charm quark (anti-quark) combines with a light anti-quark (quark) that is either present in the nucleon target or produced in the scattering process.  $z$  is the ratio of momentum carried by D-meson to the total initial momentum of the charm quark. Imagine that there is a string attached between charm quark and anti-quark. Part of the initial energy of charm will be transferred into stretching the string (QCD color field energy), resulting in lower D-meson momentum. The Peterson fragmentation function [27] was also tried in the fit but produced worse agreement between MC and data.

Events passing selection criteria detailed in the previous chapter are binned separately in  $\nu_\mu$  and  $\bar{\nu}_\mu$  mode in the quantities

$$E_{vis} = E_{\mu 1} + E_{\mu 2} + E_{HAD},$$



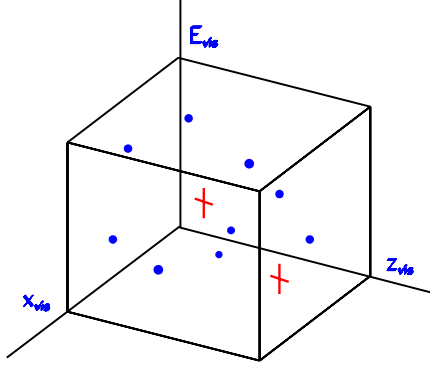


Figure 6.1: 3D bin in  $E_{vis}$ ,  $x_{vis}$ , and  $z_{vis}$  phase space. Crosses denote data, and points represent Monte Carlo events.

$$x_{vis} = \frac{4E_{\mu 1} (E_{\mu 1} + E_{\mu 2} + E_{HAD}) \sin^2 \theta_{\mu 1}}{2M (E_{\mu 2} + E_{HAD})},$$

$$z_{vis} = \frac{E_{\mu 2}}{E_{\mu 2} + E_{HAD}},$$

where  $E_{\mu 1}$  is the energy of the primary muon with the same lepton number as the beam,  $E_{\mu 2}$  is the energy of the other muon,  $E_{HAD}$  is the observed hadronic energy in the calorimeter, and  $\theta_{\mu 1}$  is the scattering angle of the primary muon. The “vis” subscript indicates that these quantities differ from the true values of  $x$ ,  $E$ , and  $z$  due to the energy carried away by the neutrino from charm decay and due to detector smearing. Other quantities of interest for comparison purposes are

$$y_{vis} = \frac{E_{\mu 2} + E_{HAD}}{E_{\mu 1} + E_{\mu 2} + E_{HAD}},$$

$$Q_{vis}^2 = 2ME_{vis}x_{vis}y_{vis}.$$

The phase space is binned in a 3-dimensional (3D) array of  $E_{vis}$ ,  $x_{vis}$ , and  $z_{vis}$  as shown in Fig.6.1.

In each mode there are 7 bins in  $E_{vis}$ , 9 bins in  $x_{vis}$ , and 6 bins in  $z_{vis}$ . The fit is performed by minimizing the negative log-likelihood function

$$\mathfrak{S} = \sum_i^{allbins} (-D_i \log MC_i + MC_i), \quad (6.4)$$

where  $D_i$  is the number of data events in a particular bin, and  $MC_i$  is the number of Monte Carlo events in the same bin. This is just the negative log of the joint Poisson probability of bins in the data being described by the model in question.

The low  $E_{vis}$  region is sensitive to the charm quark mass. Since the  $c$  quark has significant mass, the energy transferred to the struck quark in order to produce charm must be above the charm quark mass threshold. Bjorken  $x_{vis}$  distributions in both modes determine the strange and anti-strange PDFs; and the  $z_{vis}$  distribution is sensitive to fragmentation and therefor measures the function parameter  $\epsilon$ .

A binned likelihood fit is performed that compares the data to a model composed of a charm source described by Eqs. 6.1 and 6.3. The charm events are augmented with a contribution from dimuon production through  $\pi/K$  decay in the charged-current neutrino interaction's hadron shower and then processed through a detailed Monte Carlo (MC) simulation of the detector and the same event reconstruction software used for the data. The MC dimuon sample is normalized to the data through use of the inclusive single muon event rates in  $\nu_\mu$  and  $\bar{\nu}_\mu$  modes. The fit varies a common charm mass  $m_c$ , branching fraction  $B_c$ , and fragmentation parameter  $\epsilon$  for both modes, and two parameters for each mode,  $(\kappa_\nu, \alpha_\nu)$  and  $(\kappa_{\bar{\nu}}, \alpha_{\bar{\nu}})$ , that describe the magnitude and shape of the  $s$  and  $\bar{s}$  quark PDF. The strange sea parameters are defined by

$$s(x, Q^2) = \kappa_\nu \frac{\bar{u}(x, Q^2) + \bar{d}(x, Q^2)}{2} (1-x)^{\alpha_\nu}, \quad (6.5)$$

$$\bar{s}(x, Q^2) = \kappa_{\bar{\nu}} \frac{\bar{u}(x, Q^2) + \bar{d}(x, Q^2)}{2} (1-x)^{\alpha_{\bar{\nu}}}, \quad (6.6)$$

This parameterization differs slightly in the general case of  $\alpha_\nu, \alpha_{\bar{\nu}} \neq 0$  from previous LO analyses in the definition of  $\kappa_\nu, \kappa_{\bar{\nu}}$ . The motivation for not using the older definitions (of the form

$s(x, Q^2) = \frac{\kappa_\nu}{2} (\bar{u}(x, Q^2) + \bar{d}(x, Q^2)) (1-x)^{\alpha_\nu} \times \frac{\int_0^1 dx (\bar{u}(x, Q^2) + \bar{d}(x, Q^2))}{\int_0^1 dx (\bar{u}(x, Q^2) + \bar{d}(x, Q^2)) (1-x)^{\alpha_\nu}}$ ) is to avoid a procedure that requires information about PDF outside the experimentally accessible  $x$  range of the experiment. In these parameterizations values of  $\kappa_\nu = \kappa_{\bar{\nu}} = 1$  and  $\alpha_\nu = \alpha_{\bar{\nu}} = 0$  would imply an SU(3)-flavor symmetric sea; previous

<b>model</b>	<b><math>m_c</math> (<math>GeV/c^2</math>)</b>	<b><math>\epsilon</math></b>	<b><math>B_c</math> (%)</b>	<b><math>\chi^2/DOF</math></b>
BGPAR	$1.33 \pm 0.19 \pm 0.10$	$2.07 \pm 0.31 \pm 0.64$	$11.40 \pm 1.08 \pm 1.15$	105/112
GRV	$1.65 \pm 0.18 \pm 0.09$	$2.09 \pm 0.31 \pm 0.64$	$11.11 \pm 1.51 \pm 1.60$	101/112
CTEQ	$1.63 \pm 0.17 \pm 0.09$	$2.07 \pm 0.31 \pm 0.63$	$10.70 \pm 1.66 \pm 1.76$	100/112

Table 6.1: Results of LO fits to NuTeV data. The first error is statistical, the second systematic. On the far right is the  $\chi^2$  per degree of freedom.

measurements have yielded  $\kappa$  values in the range of 0.4 and  $\alpha$  values consistent with zero within large errors. By using strange sea parameterization 6.6, the implicit assumption is made that the strange sea follows the non-strange sea  $q^2$  QCD evolution.

## 6.2 NuTeV Leading Order QCD fits

The LO QCD fits were performed using three different choices of  $u$  and  $d$ -quark parton distribution function (PDF) sets with their corresponding QCD evolution kernels: GRV94LO [37] and CTEQ4LO[38] , as implemented in the PDF compilation PDFLIB [39], and a Buras-Gaemers parameterization[40] (BGPAR) that has been used extensively in this experiment and its CCFR predecessor. In the BGPAR case, an explicit Callan-Gross relation violation is implemented by replacing the term  $1 - \frac{m_c^2}{2ME_\nu\xi}$  in equation 6.3 with  $(1 + R_L)(1 + (\frac{2M\xi}{Q})^2)^{-1}(1 - y - \frac{Mxy}{2E}) + \frac{xy}{\xi}$ , where  $R_L$ , the ratio of longitudinal to transverse  $W^\pm N$  cross sections, is taken from a fit to electro-production data[41]. Tables 6.1 and 6.1 list fit results with the rightmost column in Table 6.1 showing the combined  $\chi^2$  for  $\nu$  and  $\bar{\nu}$  modes. All three models have the same good level of agreement with the dimuon data. Figure 6.2 illustrates the quality of fits by comparing the BGPAR model fit and the data is shown for the kinematic variables used directly in the fit. Figures 6.3 and 6.4 show a comparison for variables not used directly in the fits.

By using the  $\kappa$  and  $\alpha$  parameters in formula 6.5, one obtains strange and anti-strange seas for each model that are shown in Fig.6.5. Error bars take into

<b>model</b>	$\kappa$	$\bar{\kappa}$	$\alpha$	$\bar{\alpha}$
BGPAR	$0.32 \pm 0.06 \pm 0.04$	$0.37 \pm 0.05 \pm 0.04$	$-1.10 \pm 1.05 \pm 0.59$	$-2.78 \pm 0.42 \pm 0.40$
GRV	$0.37 \pm 0.05 \pm 0.03$	$0.37 \pm 0.06 \pm 0.06$	$0.87 \pm 1.25 \pm 0.71$	$0.28 \pm 0.44 \pm 0.42$
CTEQ	$0.44 \pm 0.06 \pm 0.04$	$0.45 \pm 0.08 \pm 0.07$	$1.17 \pm 1.20 \pm 0.68$	$1.08 \pm 0.44 \pm 0.41$

Table 6.2: Results of LO fits to NuTeV data. The first error is statistical, the second systematic.

account full correlations between model parameters. Figure 6.6 shows the strange sea versus anti-strange sea for three different models. In each case the strange sea agrees with anti-strange sea within the errors.

One observes that a difference in choice of PDF parameterization result in different charm production parameters, indicating significant model dependence at LO. We would like to provide a way for the rest of physics community to be able to compare to our measures dimuon production cross-section. Just quoting results in the form that they appear in the Tables 6.1-6.2 would require knowledge of many choices that are made in this particular calculation, such as PDF set used,  $V_{cd}$  and  $V_{cs}$  matrix elements, etc. Because of the above arguments, the most relevant quantity to extract is the dimuon production cross section. The NuTeV experiment has approximately the same statistical dimuon sample as the CCFR experiment. Extracting cross-section tables for each of the experiments is the most straightforward way to combine this data.

### 6.3 Systematic Errors

Although the main thrust of the analysis is the extraction of the dimuon production cross-section, the various sources of systematic uncertainty are presented by listing their contributions to the LO fit parameters. This is done for reasons of clarity, since the individual systematic uncertainty contributions add too many entries in the cross-section tables, and it is completely equivalent since the systematic uncertainty on the parameters of the LO fits propagates directly to the cross-

	$\mathbf{m}_c \text{ (GeV}/c^2\text{)}$	$\epsilon$	$\mathbf{B}_c \text{ (\%)}$	$\kappa$	$\bar{\kappa}$	$\alpha$	$\bar{\alpha}$
$\nu \pi/K(15\%)$	0.022	0.51	0.81	0.018	0.031	0.01	0.05
$\bar{\nu} \pi/K(21\%)$	0.006	0.13	0.06	0.001	0.017	0.01	0.17
$R_L(20\%)$	0.037	0.09	0.17	0.001	0.010	0.48	0.26
$\mu$ energy scale (1%)	0.080	0.33	0.74	0.036	0.023	0.25	0.24
Hadron energy scale (0.4%)	0.012	0.08	0.02	0.005	0.003	0.01	0.04
MC statistics	0.047	0.02	0.31	0.012	0.006	0.23	0.01
Flux	0.010	0.01	0.07	0.001	0.000	0.03	0.03
Systematic Error	0.104	0.64	1.15	0.043	0.043	0.59	0.40

Table 6.3: Systematic error sources for LO-QCD fit to NuTeV data.

section measurement.

The main sources of the systematic uncertainties arise from modeling uncertainties in the Monte Carlo. The most significant are the  $\pi/K$  decay background simulation, the detector calibration from the analysis of test beam hadron and muon data as a functions of energy and position, and the overall normalization. In addition, in the case of the BGPARG fits, the uncertainty on the longitudinal structure function is important.

Systematic errors are summarized in Table 6.3. The main sources are:

1. uncertainties in  $\pi/K$  background for neutrinos and anti-neutrinos;
2. an  $R_L$  systematic error due to the uncertainty in the longitudinal cross-section calculation;
3. calibration uncertainties of muon and hadron energies;
4. the limited statistics of the Monte Carlo sample used in the fit;
5. uncertainties in the neutrino and anti-neutrino flux used in the Monte Carlo simulation.

To demonstrate that the background is estimated correctly, a study of *same sign* dimuons is performed. These events can only come from charged current events

with a  $\pi$  or  $K$  decaying into same sign muon as the primary one. Production could occur if  $b$  quarks were produced in charged current interactions, but the rate is too small to see [28]. To look at these events the additional requirement that both muons must go through two gaps in the toroid so that both signs are determined is imposed. Figure 6.13 shows the NuTeV toroid-toroid dimuon sample. Secondary muons from background are lower energy than muons resulting from charm production. As a result only a few reach the second gap in the toroid. The same sign dimuon sample is shown on Fig.6.14. Most events are  $\pi/K$  decays. Events from charm sources end up in the same sign sample because the sign of the second muon can be misreconstructed by the toroid. Notice that Monte Carlo describes the data well, meaning that the only significant effect of the second muon charge misreconstruction is the reduced statistics in the dimuon analysis sample. The number of actual background events is 270 out of 442 in  $\nu$  mode and 52 out of 101 in  $\bar{\nu}$  mode in the same sign sample. The number of background events in opposite sign dimuon sample is 195 out of 2320 in  $\nu$  mode and 35 out of 669 in  $\bar{\nu}$  mode. Because of charge misidentification of the second muon, 45.7 events leak from the opposite sign into same sign sample in  $\nu$  mode, while only 7.9 leak the opposite way. In the  $\bar{\nu}$  mode, these numbers are 8.6 and 1.9.

The total number of dimuon events generated as a result of  $\nu$  interaction that end up reconstructed in the  $\bar{\nu}$  sample is  $1.4 \times 10^{-4}$ . The number of dimuons generated in  $\bar{\nu}$  mode and misreconstructed to belong to the  $\nu$  sample is  $0.1 \times 10^{-4}$ . The total number of same sign events with the sign opposite to the polarity of the toroid is zero both in the data and the Monte Carlo. Out of all dimuon events that pass all but charge id cuts, 91.6% pass charge id cuts in  $\nu$  mode and 92.9% in  $\bar{\nu}$  mode. The total reconstruction efficiency is 67.8% in  $\nu$  mode and 67.9% for  $\bar{\nu}$ s.

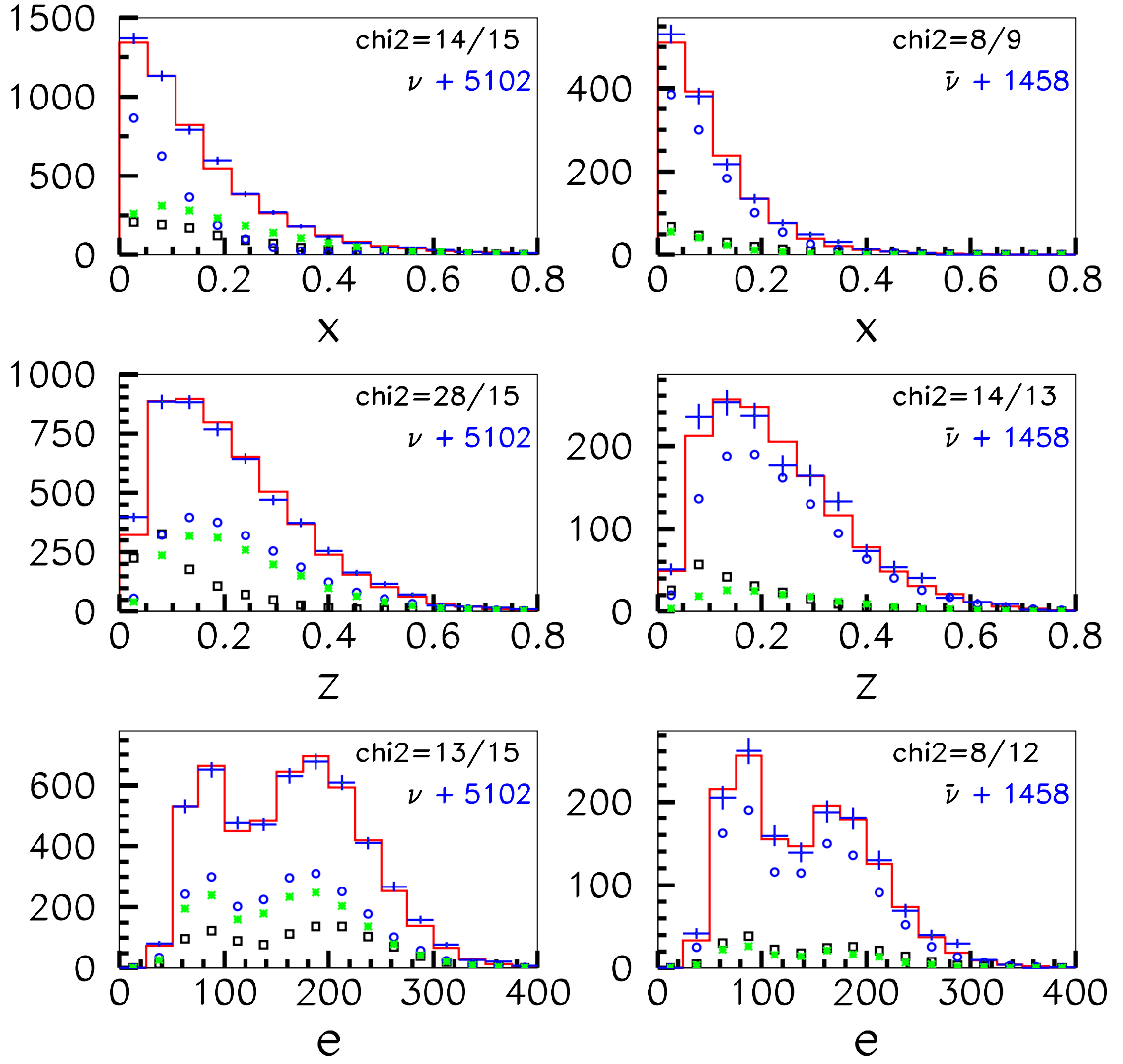


Figure 6.2: NuTeV  $x$ ,  $z$ , and  $E$  distributions for dimuons. Neutrino mode is on the left, anti-neutrino mode is on the right. Crosses represent the data. Circles represent strange sea contribution, stars -  $d$  quark contribution, and boxes -  $\pi K$  background. The histogram is the sum of all model contributions.  $\chi^2$  for total degrees of freedom is shown for each plot.

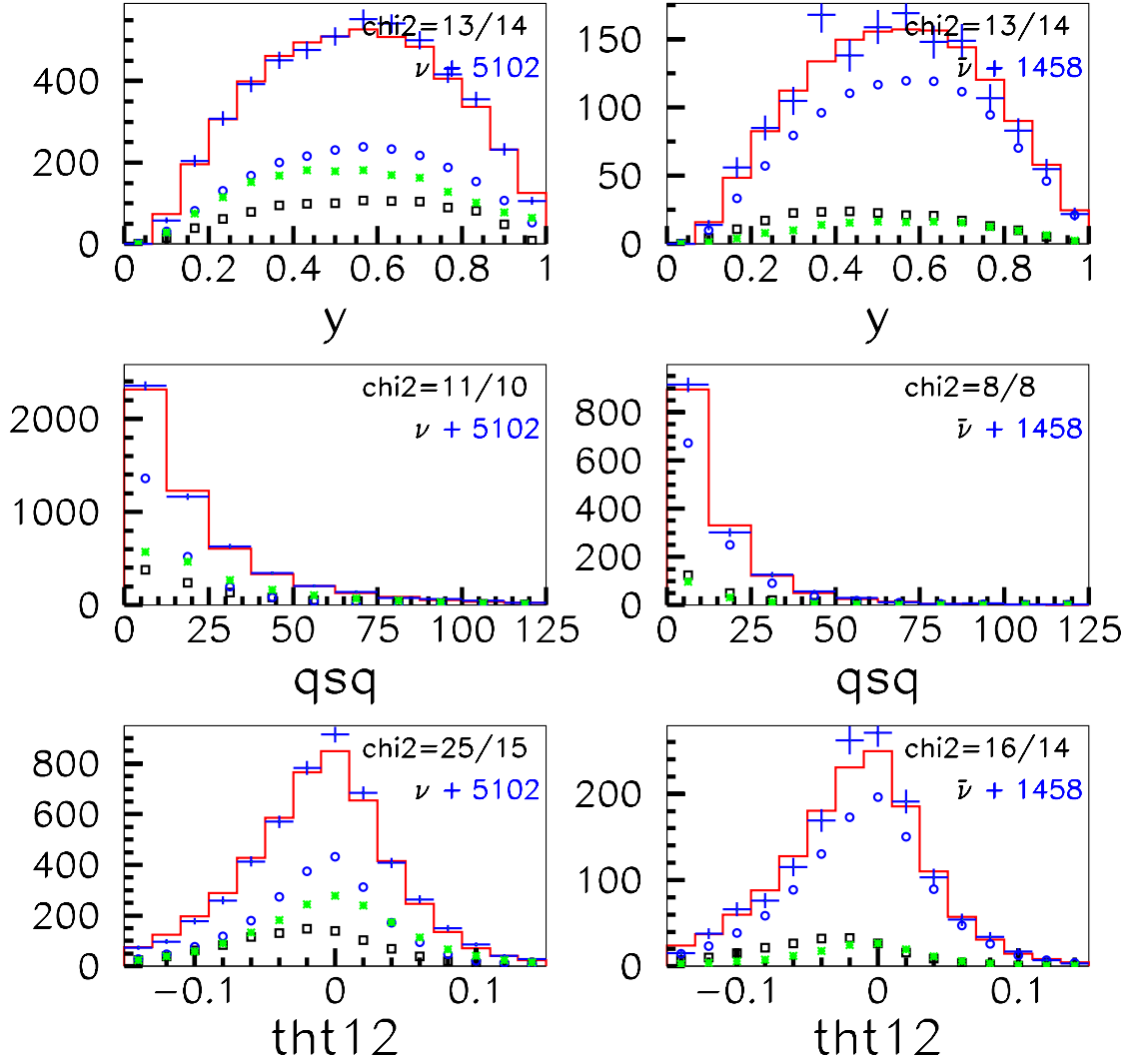


Figure 6.3: NuTeV inelasticity  $y$ , W boson momentum  $Q^2$ , and the opening angle between two muons distributions for dimuons. Neutrino mode is on the left, anti-neutrino mode is on the right. Crosses represent the data. Circles represent strange sea contribution, stars -  $d$  quark contribution, and boxes -  $\pi K$  background. The histogram is the sum of all model contributions.  $\chi^2$  for total degrees of freedom is shown for each plot.



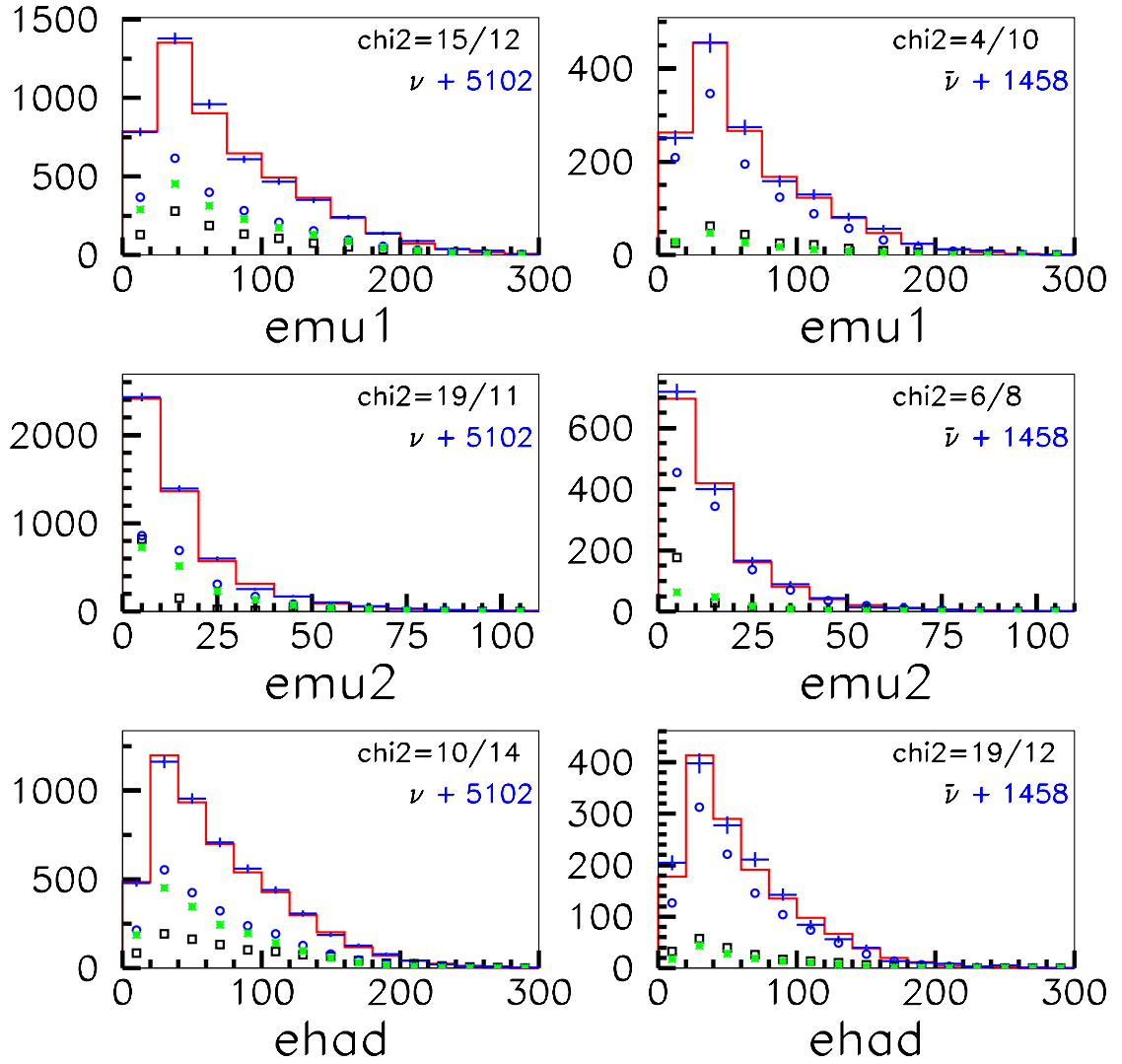


Figure 6.4: NuTeV energy of the first muon, energy of the second muon, and the hadronic energy distributions for dimuons. Neutrino mode is on the left, anti-neutrino mode is on the right. Crosses represent the data. Circles represent strange sea contribution, stars -  $d$  quark contribution, and boxes -  $\pi K$  background. The histogram is the sum of all model contributions.  $\chi^2$  for total degrees of freedom is shown for each plot.

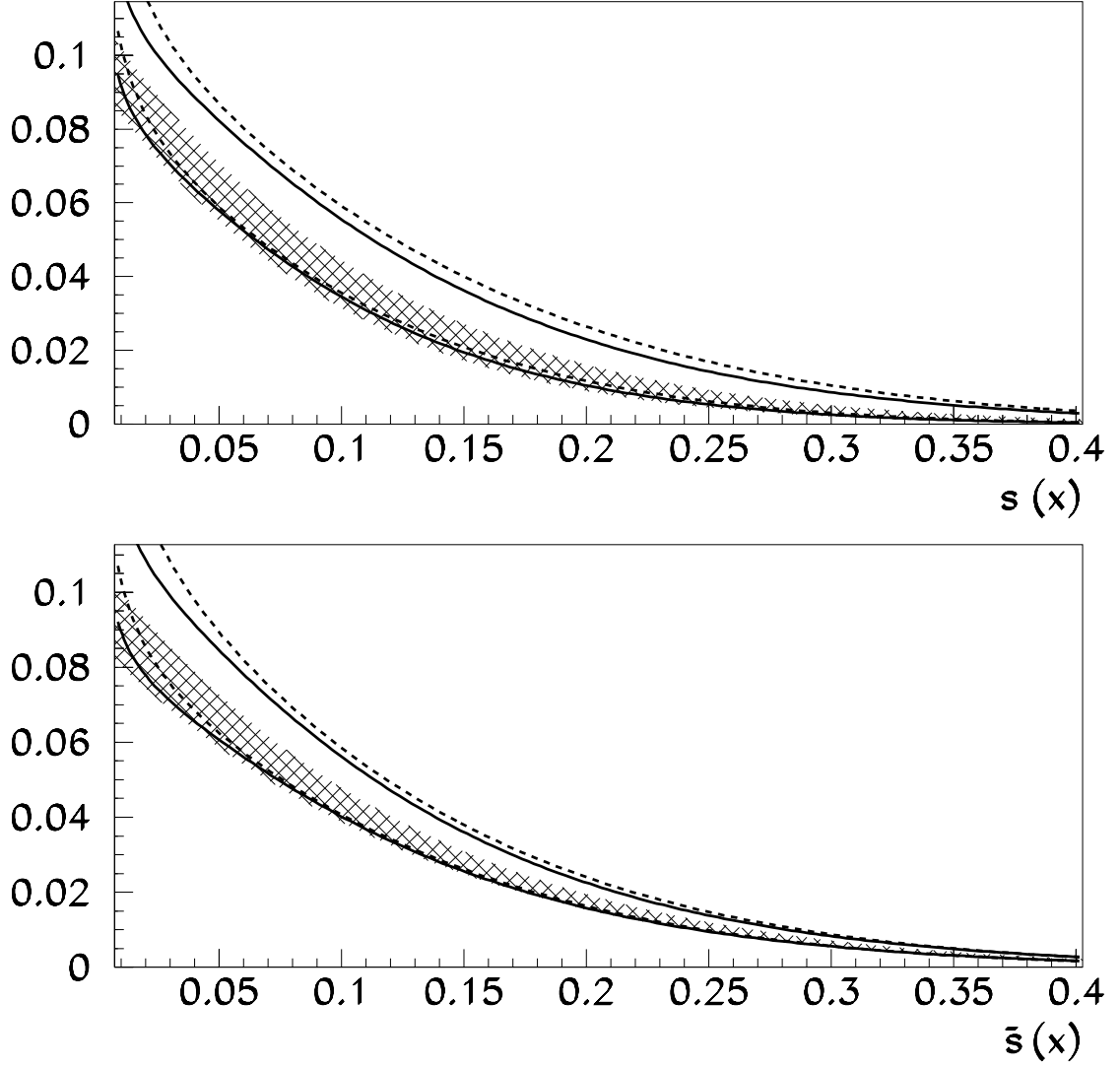


Figure 6.5: NuTeV strange (top) sea and anti-strange (bottom) sea as functions of Bjorken  $x$  for  $Q^2 = 16 \text{ GeV}^2$ . Hatched - BGP model. The solid lines bound GRV fit region, dashed lines - CTEQ.

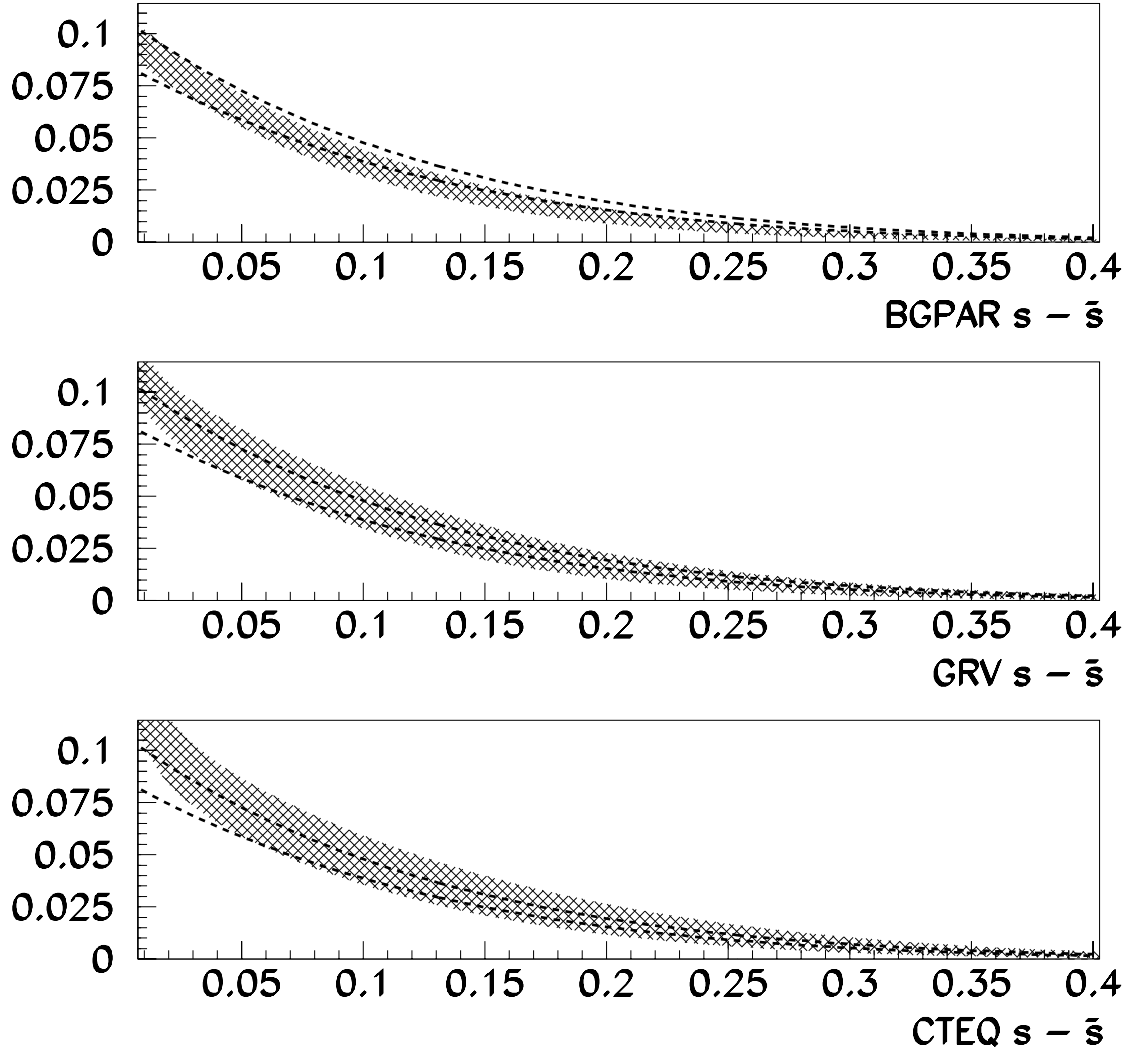


Figure 6.6: NuTeV strange sea (hatched) vs. anti-strange sea (dashed) for  $Q^2 = 16 \text{ GeV}^2$ . Top - BGP model, middle - GRV, and bottom - CTEQ.

## 6.4 Leading Order Fits To CCFR Data

The CCFR experiment is a predecessor of NuTeV. NuTeV used essentially the same detector as CCFR, but CCFR did not have a sign-selected beam to distinguish between events that originate from neutrino interactions from events that are the result of anti-neutrinos interactions they had to rely heavily on a “ $P_t$  algorithm”. The algorithm exploits the fact that in dimuon event the secondary muon has a lower transverse momentum with respect to the hadron shower than the primary muon. Use of this algorithm meant that CCFR data had a substantially higher fraction of  $\nu_\mu$  events misreconstructed as  $\bar{\nu}_\mu$  and vice-versa. This was especially true for the  $\bar{\nu}_\mu$  sample. CCFR had a beam of higher energy than NuTeV. The dimuon data statistics from both experiments are almost the same. Description of CCFR experiment can be found in Refs. [22] and [21].

We reanalyzed CCFR data in the same manner as NuTeV data. The results of the fit using three different cross-section models are shown in Tables 6.4-6.5. Strange and anti-strange seas are shown in Figs.6.7-6.9.

model	$m_c (GeV/c^2)$	$\epsilon$	$B_c (\%)$	$\chi^2/DOF$
BGPAR	$1.20 \pm 0.23 \pm 0.12$	$0.88 \pm 0.12 \pm 0.04$	$11.43 \pm 0.95 \pm 0.40$	138/112
GRV	$1.65 \pm 0.18 \pm 0.10$	$0.88 \pm 0.11 \pm 0.04$	$11.55 \pm 1.17 \pm 0.49$	137/112
CTEQ	$1.54 \pm 0.19 \pm 0.10$	$0.90 \pm 0.12 \pm 0.04$	$11.16 \pm 1.22 \pm 0.51$	136/112

Table 6.4: Results of LO fits to CCFR data. The first error is statistical, the second systematic. The far right column shows  $\chi^2$  per degree of freedom

model	$\kappa$	$\bar{\kappa}$	$\alpha$	$\bar{\alpha}$
BGPAR	$0.32 \pm 0.06 \pm 0.04$	$0.37 \pm 0.05 \pm 0.04$	$-1.10 \pm 1.05 \pm 0.59$	$-2.78 \pm 0.42 \pm 0.40$
GRV	$0.37 \pm 0.05 \pm 0.03$	$0.37 \pm 0.06 \pm 0.06$	$0.87 \pm 1.25 \pm 0.71$	$0.28 \pm 0.44 \pm 0.42$
CTEQ	$0.44 \pm 0.06 \pm 0.04$	$0.45 \pm 0.08 \pm 0.07$	$1.17 \pm 1.20 \pm 0.68$	$1.08 \pm 0.44 \pm 0.41$

Table 6.5: Results of LO fits to CCFR data. The first error is statistical, the second systematic.

As in the case of NuTeV, CCFR leading order fits to different models yield

different model parameters while describing the data equally well. Strange and anti-strange sea are shown on Fig.6.10. The strange sea versus anti-strange sea is shown on Fig.6.11 for each of the three models. In each case, the strange sea agrees with anti-strange sea within errors. Finally, Fig.6.12 compares NuTeV strange sea with CCFR strange sea. Systematic errors estimates for the CCFR experiment are taken from previous work [22], since access to that experiment data and MC was limited.

One notices that the fragmentation function parameter is very different between NuTeV and CCFR. It is explained by the fact that in NuTeV analysis more low energy second muons are accepted in order to obtain statistically significant data sample. Figure 6.15 shows NuTeV  $z_{vis}$  distributions for the full dimuon sample and for toroid-toroid events. Only muons with high enough energies reach the toroid, therefor the toroid-toroid sample has very different  $z_{vis}$  form. The shape difference is shown on Fig.6.16. Also there are much fewer background events, 8.6% in  $\nu$  mode and 5.3% in  $\bar{\nu}$  mode, because  $\pi/K$  decays normally produce low energy muons. The fit to the toroid-toroid sample produces  $\epsilon = 1.27 \pm 0.23$ , the value that is consistent with CCFR. The shape difference in  $z_{vis}$  between NuTeV and CCFR (Fig.6.17) looks very much like the shape difference between NuTeV full sample and NuTeV toroid-toroid sample. Notice that Monte Carlo mimics data very well. The statistical error on  $\epsilon$  from the toroid-toroid fit is smaller than the statistical error from full fit, even though the toroid-toroid sample has much fewer events. Summarizing, in NuTeV analysis a lot of low energy muons are accepted which leads to increase in fragmentation function parameter  $\epsilon$ . That also leads to decreased sensitivity to the fragmentation function which results in bigger errors on  $\epsilon$ . The third effect is a larger background contribution, and thus, bigger systematic error assigned to  $\epsilon$ .

## 6.5 $V_{cd}$ Matrix Element

In the high  $x$  region of neutrino data most of the charm production comes from the  $d$  quark. The total dimuon rate is thus proportional to  $V_{cd}^2 \times B_c$ . In the cross section calculation code the  $V_{cd}$  value is fixed, and the fit varies  $B_c$ . This can be converted into the measurement of  $V_{cd}$  as

$$V_{cd}^2 = V_{cd}^{ext2} \times B_c^{ext} / B_c, \quad (6.7)$$

where  $ext$  stands for the value that is estimated from external sources and used in the Monte Carlo. The external value for the matrix element is obtained from the matrix unitarity assumption and is equal to

$$V_{cd}^{ext} = 0.2205$$

with a negligible error. The branching ratio is estimated to be [19]

$$B_c^{ext} = (9.3 \pm 0.9)\%.$$

Combining these two with the branching ratio measured by NuTeV

$$B_c = (11.4 \pm 1.08 \pm 1.15)\%,$$

the  $V_{cd}$  evaluates to

$$V_{cd} = 0.244 \pm 0.017 \pm 0.017.$$

The CCFR experiment measured the matrix element to be [21]

$$V_{cd}^{CCFR} = 0.232 \pm 0.019,$$

but they used an old value for  $B_c^{ext}$  ( $[9.9 \pm 1.2]\%$  vs.  $[9.3 \pm 0.9]\%$ ). With new  $B_c^{ext}$ , the  $V_{cd}$  matrix element measured by CCFR becomes

$$V_{cd}^{CCFR} = 0.239 \pm 0.013 \pm 0.015.$$

The NuTeV measurement is consistent with the previous one, and both are higher than, but consistent with, the unitarity prediction. Combining NuTeV and CCFR results, this thesis quotes the most precise measurement of  $V_{cd}$ :

$$V_{cd} = 0.242 \pm 0.011 \pm 0.017.$$

Further improvement requires a better measurement of  $B_c^{ext}$ .

## 6.6 The high $x$ region

This section presents a supplementary investigation of the high  $x$  region ( $x > 0.5$ ). The objective of this study is to ascertain whether there is any indication of an enhancement in the cross-section that we may be missing due to our use of wide  $x$  bins (dictated by the low observed event rate at high  $x$ ). Such an enhancement could be caused by an unusually large strange sea, particularly in neutrino mode, which has been advocated to resolve certain discrepancies between inclusive charged lepton and neutrino scattering [14]. Previous dimuon analyses [21, 22] may have missed this effect due to dependence on the particular model used to parameterize the strange sea distribution.

In order to minimize model-dependent corrections, we report our high  $x$  cross-section measurements as fractions of the total dimuon cross-section. Similarly, to quote a limit for the  $x > 0.5$  cross-section we use the observed data rate for  $x_{VIS} > 0.5$ . This is a conservative way to set a limit, since by the kinematic effect of the missing decay neutrino energy, the contribution to a given  $x_{VIS}$  bin always comes from  $x < x_{VIS}$ .

The cross-section ratio of the dimuon cross-section for  $x > 0.5$  to the total dimuon cross-section in a given energy bin can be expressed as

$$\frac{\sigma_{x>0.5}^{2\mu}}{\sigma^{2\mu}} = \frac{N_{x>0.5}}{N_{tot}} \frac{M}{M_{E>5}}, \quad (6.8)$$

where  $N_{x>0.5}$  is the number of observed events for  $x_{VIS} > 0.5$ ,  $N_{tot}$  is the total number of observed dimuon events, and  $M$  is the Monte Carlo prediction with all experimental cuts applied, and  $M_{E>5}$  is the Monte Carlo prediction without the  $\pi/K$  decay contribution and with only the  $E_{\mu 2} > 5$  GeV cut applied. For this study, we use the same data selection criteria described in Section 4, except for the  $x_{VIS}$  selection, which is changed to:  $0 \leq x_{VIS} \leq 2$ .

$E_{VIS}$	$N_{x>0.5}$	MC	$N_{\pi/k}$	$N_{\bar{s}}$	$N_{tot}$	$\frac{M}{M_{e>5}}$
34.8-128.6	1	3.4	2.1	1.3	688	0.67
128.6-207.6	4	3.4	1.9	1.5	528	0.75
207.6-388.0	2	3.4	2.1	1.3	238	0.78

Table 6.6: High- $x$  events using the anti-neutrino data sample.  $E_{VIS}$  is in GeV,  $N_{x>0.5}$  is the number of observed events for  $x_{VIS} > 0.5$ ,  $MC$  is the Monte Carlo prediction for  $x_{VIS} > 0.5$ ,  $N_{\pi/k}$  and  $N_{\bar{s}}$  are the  $\pi/K$  decay and  $\bar{s}$  contributions to  $MC$ ,  $N_{tot}$  is the total number of dimuon events, and  $\frac{M}{M_{e>5}}$  is the Monte Carlo correction in Eq. 6.8

$E_{VIS}$	$N_{x>0.5}$	MC	$N_{\pi/k}$	$N_s$	$N_{tot}$	$\frac{M}{M_{e>5}}$
36.1-153.9	65	53.39	11.6	2.0	2304	0.64
153.9-214.1	42	53.44	14.8	1.8	1598	0.75
214.1-399.5	60	53.38	17.4	2.2	1201	0.78

Table 6.7: High- $x$  events using the neutrino data sample.  $E_{VIS}$  is in GeV,  $N_{x>0.5}$  is the number of observed events for  $x_{VIS} > 0.5$ ,  $MC$  is the Monte Carlo prediction for  $x_{VIS} > 0.5$ ,  $N_{\pi/k}$  and  $N_s$  are the  $\pi/K$  decay and  $s$  contributions to  $MC$ ,  $N_{tot}$  is the total number of dimuon events, and  $\frac{M}{M_{e>5}}$  is the Monte Carlo correction in Eq. 6.8.

In the anti-neutrino dimuon data sample we define three energy bins and record the number of the observed dimuon events with  $x_{VIS} > 0.5$  in the data for each bin, together with the Monte Carlo prediction and all the relevant information for Eq. 6.8. Here the Monte Carlo prediction is very well constrained by our dimuon data in the full  $x$  range, since the observed rate is mostly due to scattering on  $\bar{s}$  quarks. The results are presented in Table 6.6. Systematic and statistical errors on the Monte Carlo prediction are negligible for this discussion. Treating the Monte Carlo prediction as a “background,” and using Eq. 6.8, we set cross-section ratio upper limits at 90% CL, for any additional source of  $x > 0.5$  dimuons, of 0.0012, 0.007, and 0.009, respectively, in each of the energy bins defined in Table 6.6 (counting from lower to higher energy bin).



We follow the same procedure in the neutrino data sample. Here, there is an additional complication in the interpretation of the result since a substantial contribution from valence quark events is expected. The Monte Carlo prediction for the rates of the non-strange sea component is not directly constrained by our dimuon data, but rather by inclusive structure function measurements. The results are presented in Table 6.7. It is worth noticing that within the model and PDF sets used in this analysis (BGPART) the Monte Carlo prediction for the contribution of the strange sea is only on the order of 3.7% of the total rate for  $x_{VIS} > 0.5$ ; most of the contribution (69%) in this model comes from the valence quarks.

Using Eq. 6.8 and treating the Monte Carlo prediction as a “background” source, we set 90% CL limits for an additional cross-section source at  $x > 0.5$ . We find that for the first and last energy bins in Table 6.7 this additional source cannot be larger than 0.006 and 0.013 of the total dimuon cross-section, while for the 153.9-214.1 bin there is less than 5% probability that there is an additional source consistent with our data. The result is quoted this way because we have a  $1.75\sigma$  negative yield compared to our background prediction.

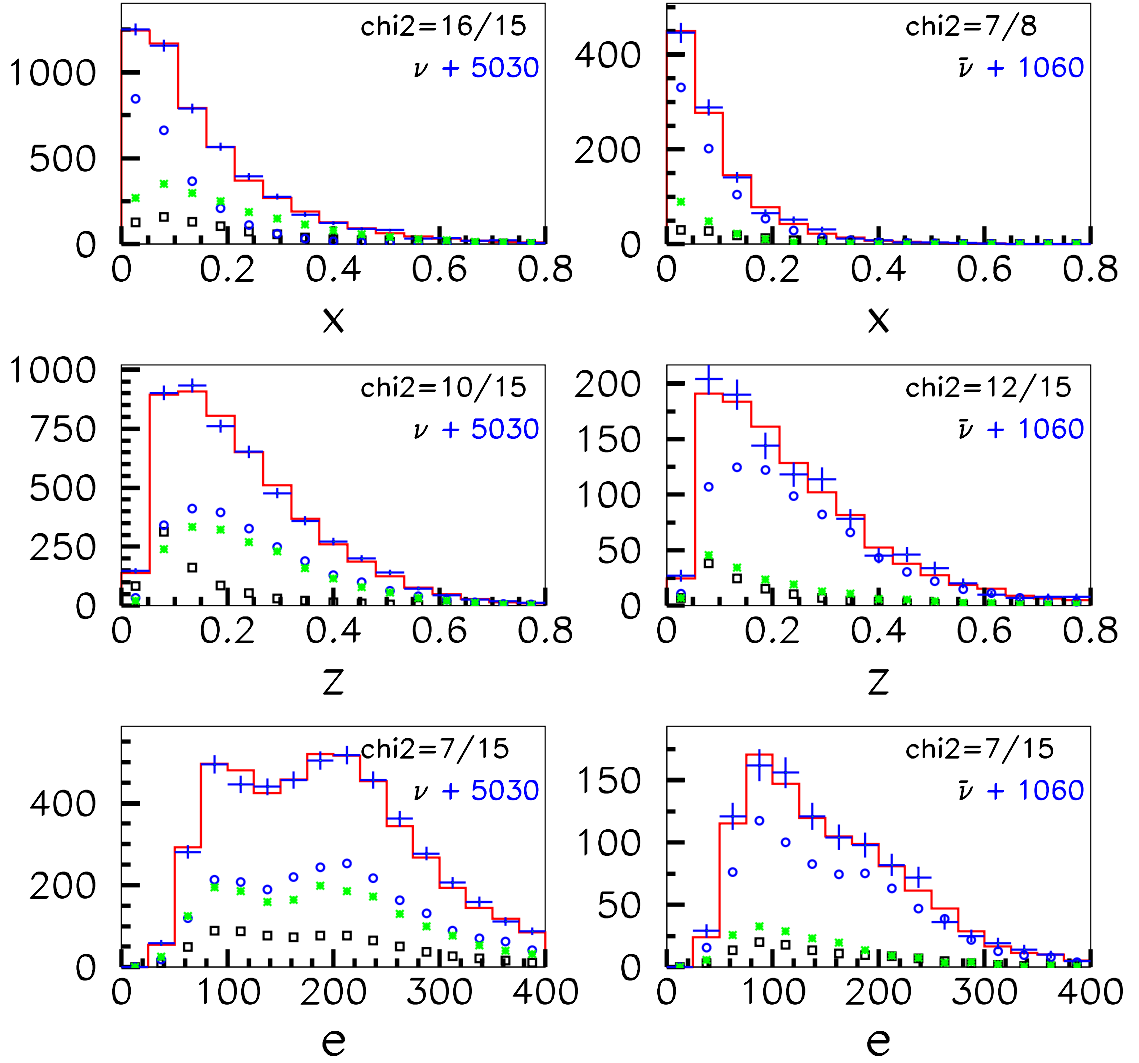


Figure 6.7: CCFR  $x$ ,  $z$ , and  $E$  distributions for dimuons. Neutrino mode is on the left, anti-neutrino mode is on the right. Crosses represent the data. Circles represent strange sea contribution, stars -  $d$  quark contribution, and boxes -  $\pi K$  background. The histogram is the sum of all model contributions.  $\chi^2$  for total degrees of freedom is shown for each plot.

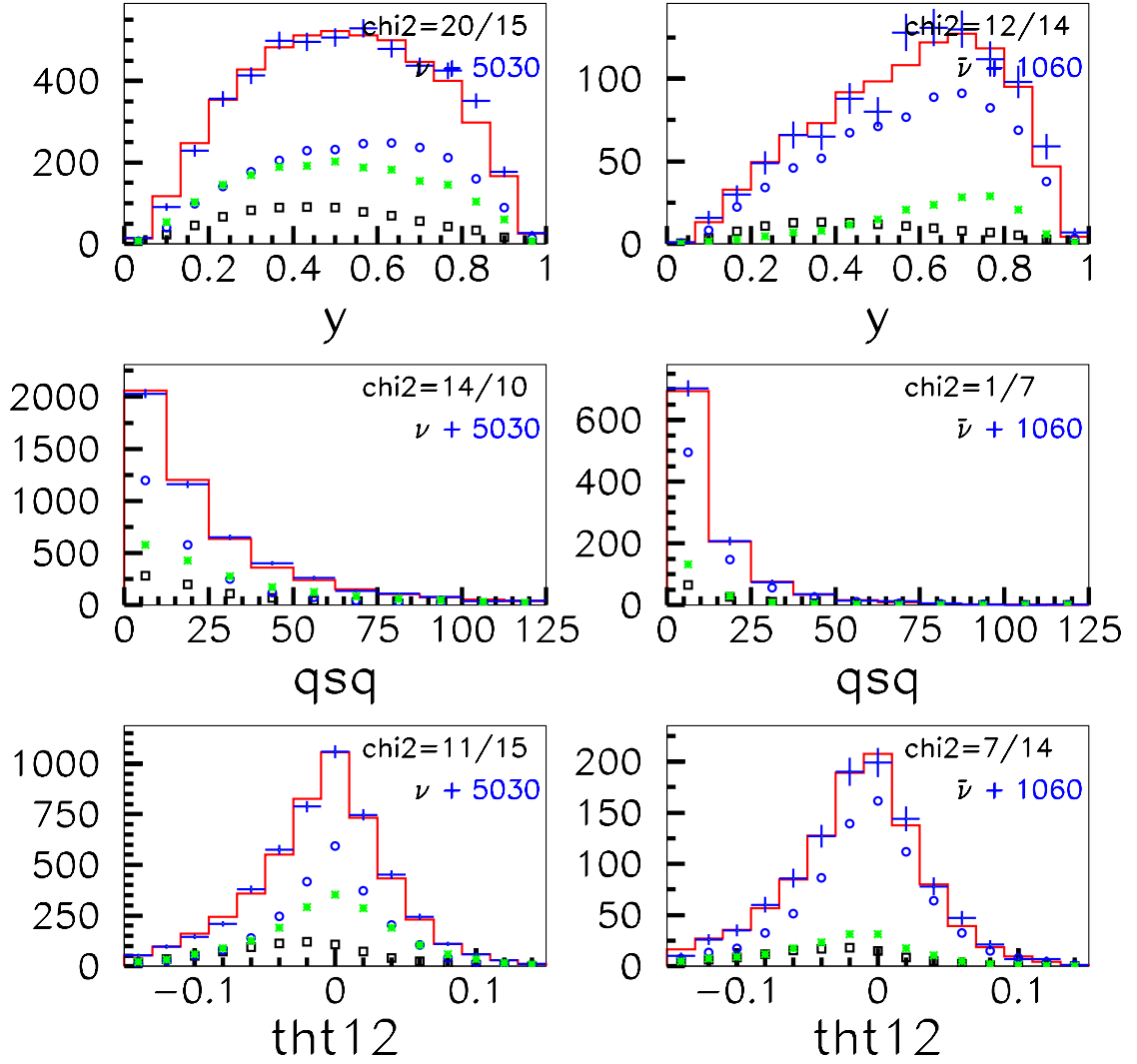


Figure 6.8: CCFR inelasticity  $y$ , W boson momentum  $Q^2$ , and the opening angle between two muons distributions for dimuons. Neutrino mode is on the left, anti-neutrino mode is on the right. Crosses represent the data. Circles represent strange sea contribution, stars -  $d$  quark contribution, and boxes -  $\pi K$  background. The histogram is the sum of all model contributions.  $\chi^2$  for total degrees of freedom is shown for each plot.

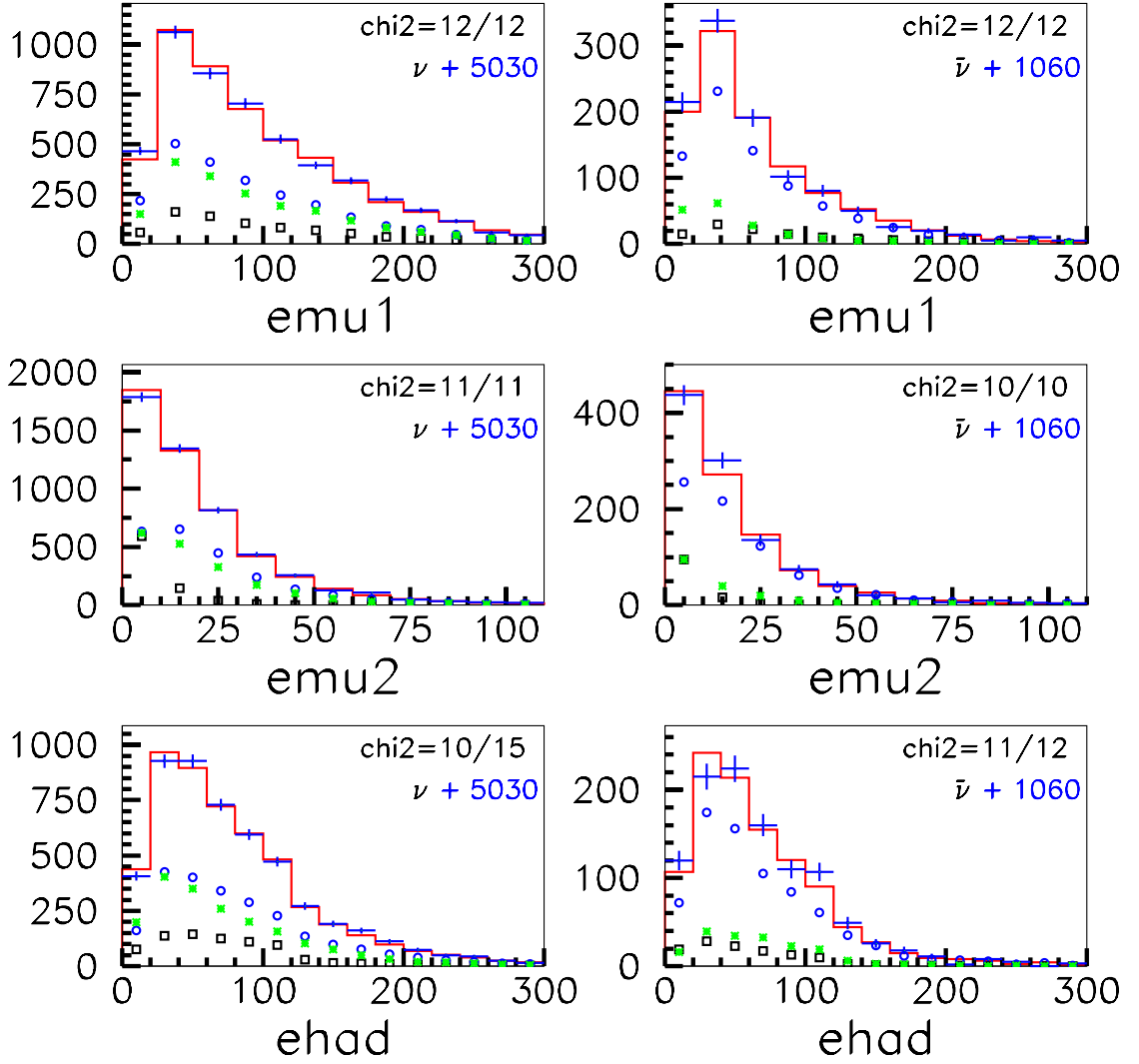


Figure 6.9: CCFR energy of the first muon, energy of the second muon, and the hadronic energy distributions for dimuons. Neutrino mode is on the left, anti-neutrino mode is on the right. Crosses represent the data. Circles represent strange sea contribution, stars -  $d$  quark contribution, and boxes -  $\pi K$  background. The histogram is the sum of all model contributions.  $\chi^2$  for total degrees of freedom is shown for each plot.

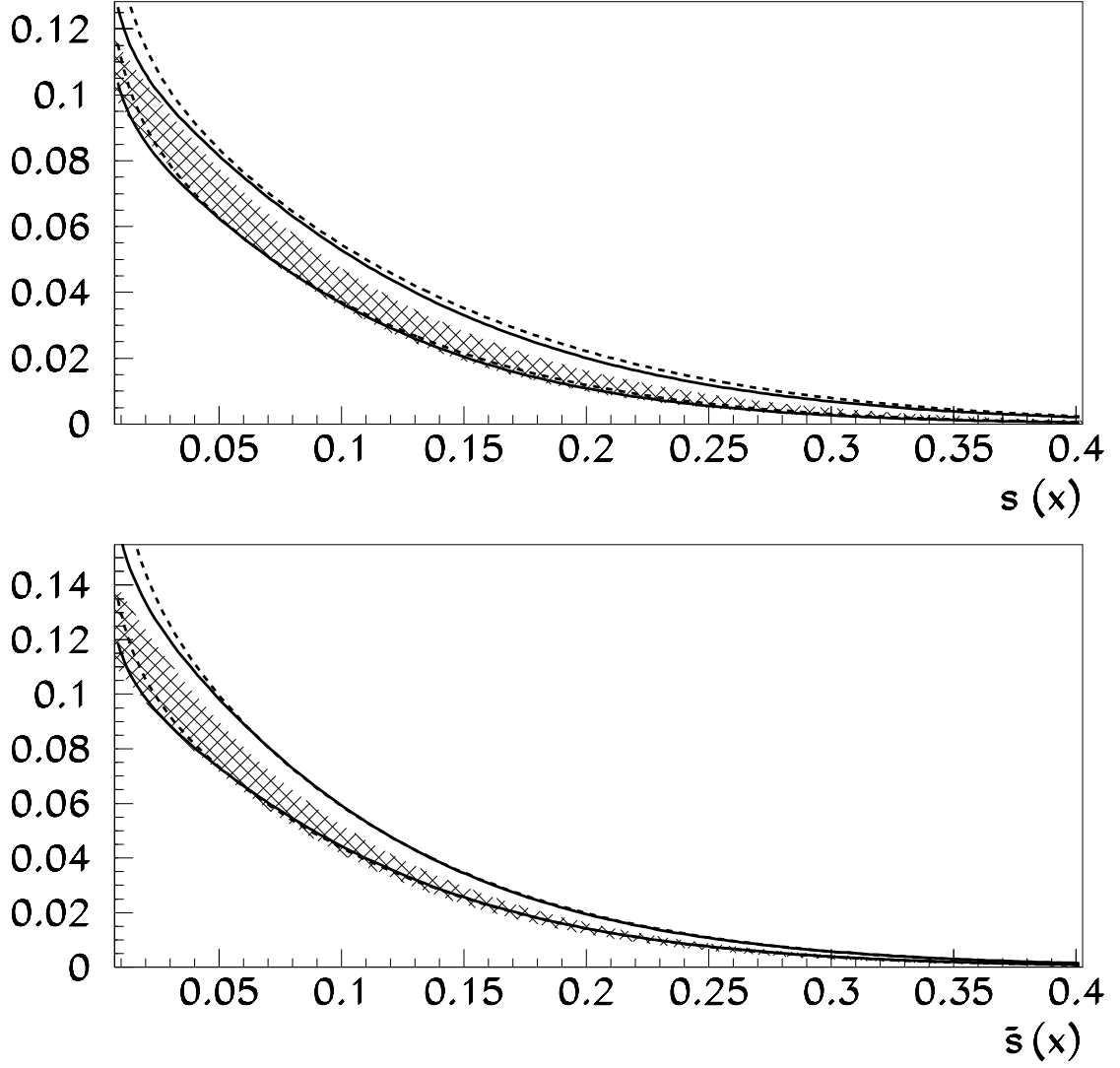


Figure 6.10: CCFR strange (top) sea and anti-strange (bottom) sea as functions of Bjorken  $x$  for  $Q^2 = 16 \text{ GeV}^2$ . Hatched - BGPAR model. The solid lines bound GRV fit region, dashed lines - CTEQ.

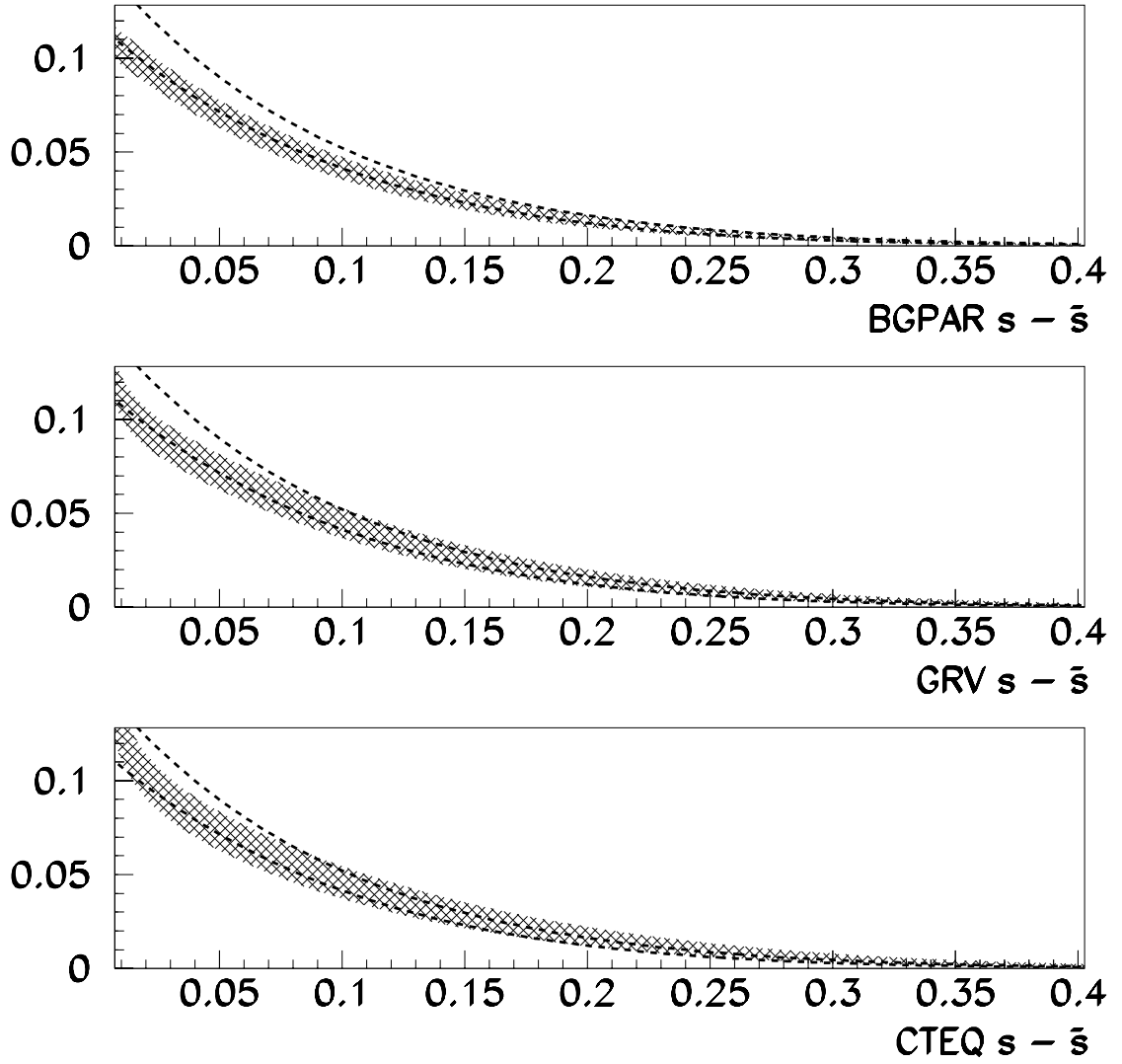


Figure 6.11: CCFR strange sea (hatched) vs. anti-strange sea (dashed) for  $Q^2 = 16$   $\text{GeV}^2$ . Top - BGP model, middle - GRV, and bottom - CTEQ.

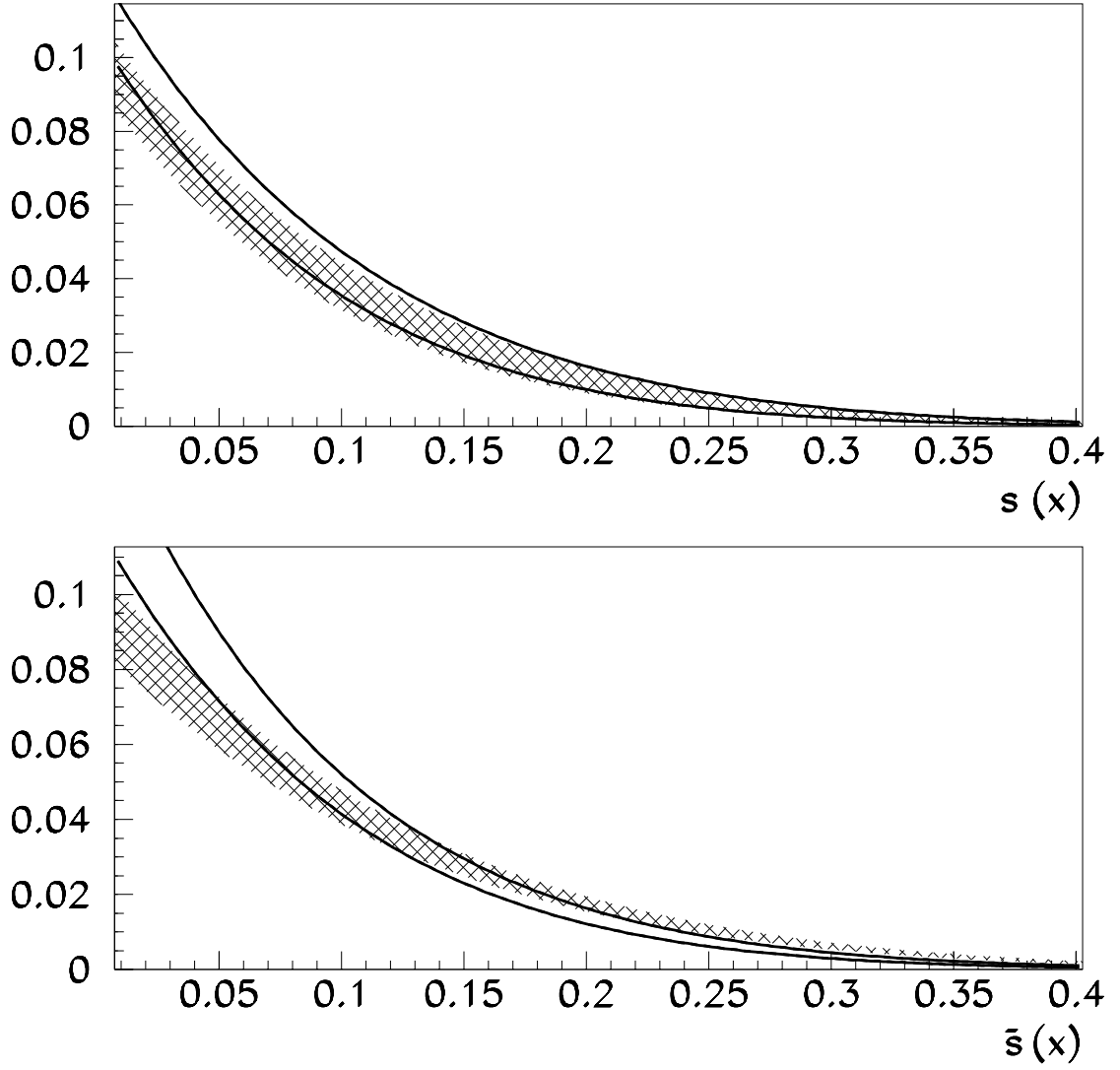


Figure 6.12: NuTeV strange sea (hatched) vs. CCFR strange sea (solid) for  $Q^2 = 16$   $\text{GeV}^2$ , BGPART model. Top - neutrino mode, bottom - anti-neutrino mode

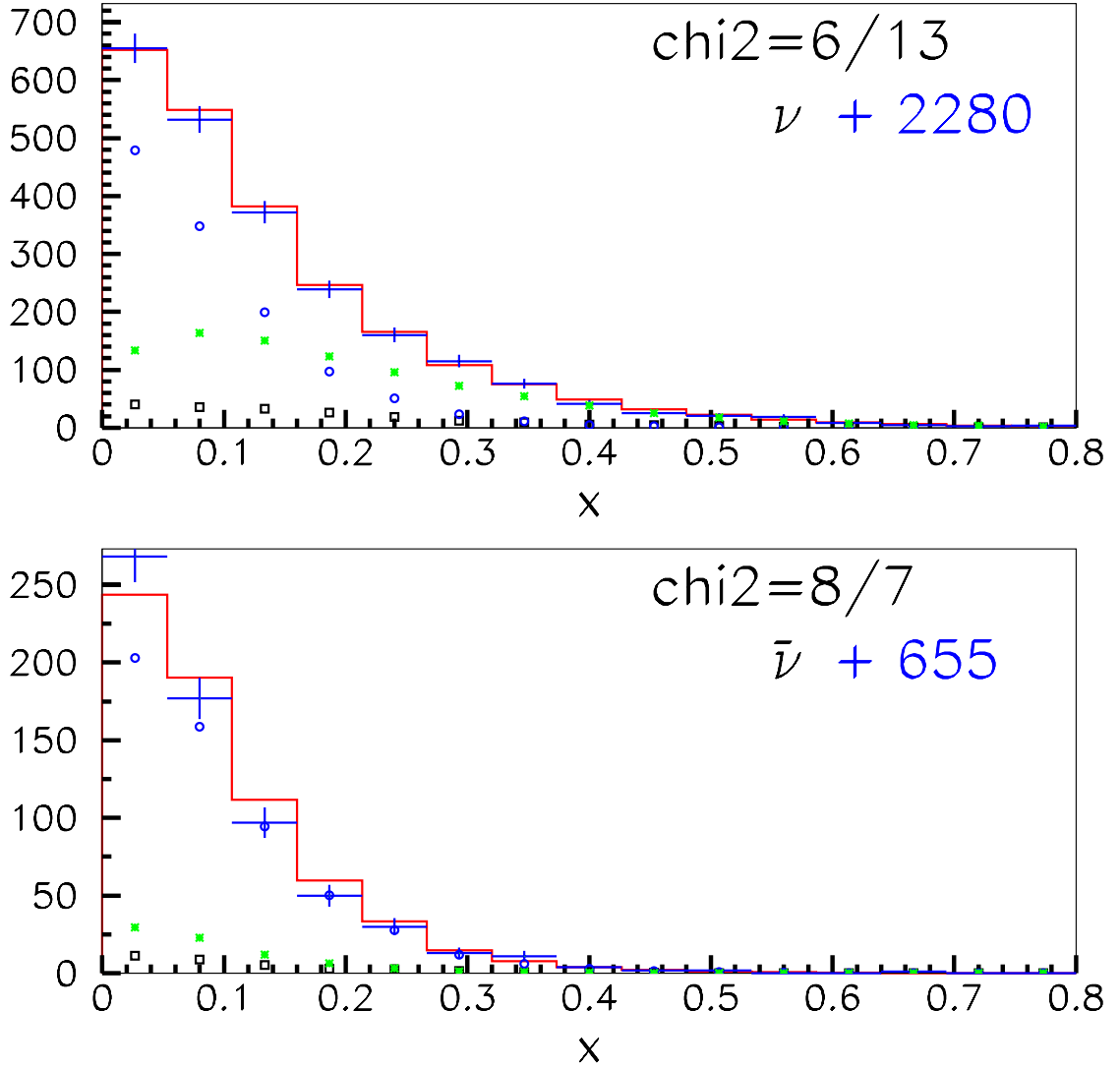


Figure 6.13: NuTeV  $x$  toroid-toroid distribution. Neutrino mode is on the top, anti-neutrino mode is on the bottom. Crosses represent the data. Circles represent strange sea contribution, stars -  $d$  quark contribution, and boxes -  $\pi K$  background. The histogram is the sum of all model contributions.  $\chi^2$  for total degrees of freedom is shown for each plot.



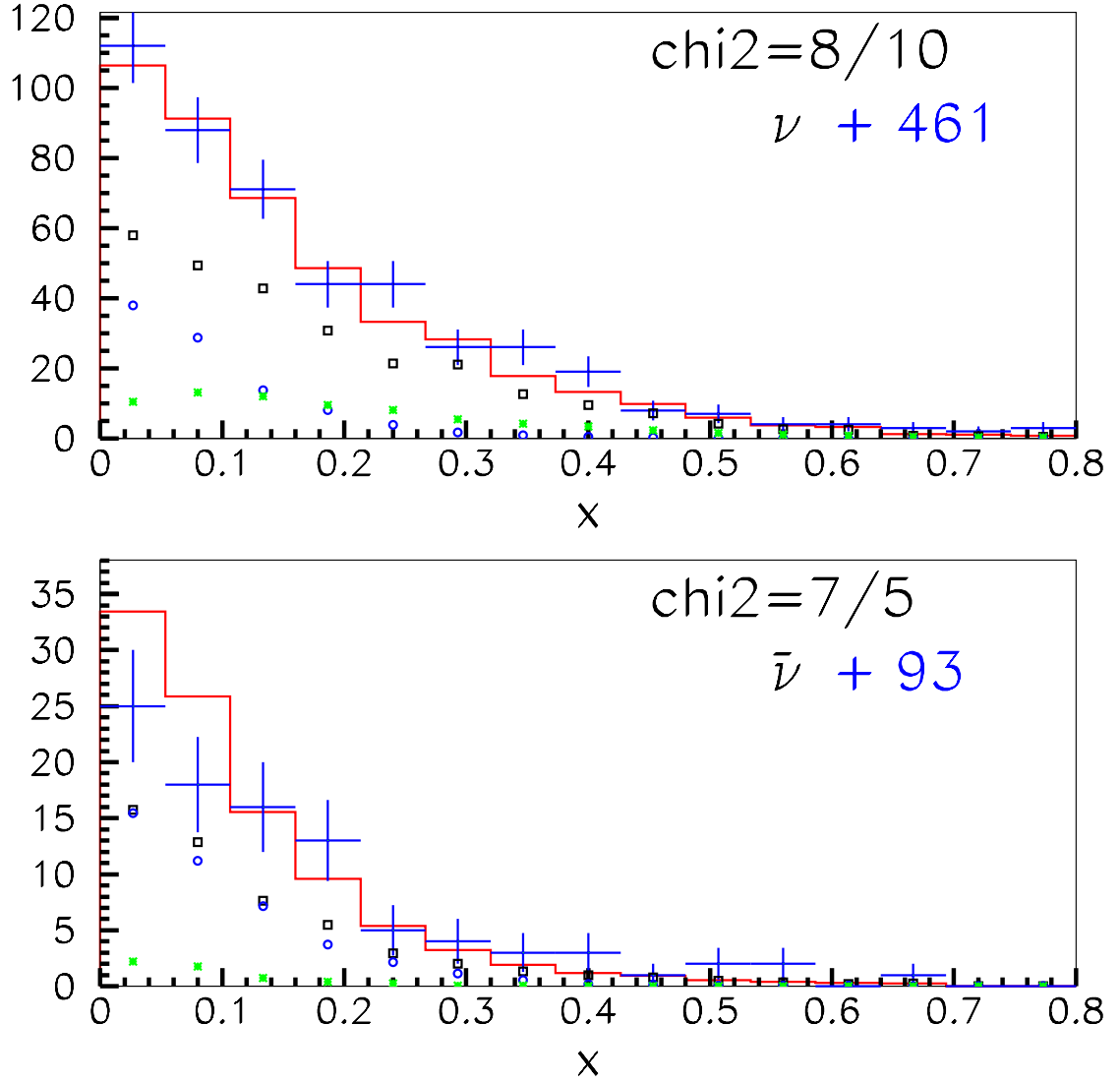


Figure 6.14: NuTeV same sign dimuons, toroid-toroid sample. Neutrino mode is on the top, anti-neutrino mode is on the bottom. Crosses represent the data. Circles represent strange sea contribution, stars -  $d$  quark contribution, and boxes -  $\pi K$  background. The histogram is the sum of all model contributions.  $\chi^2$  for total degrees of freedom is shown for each plot.

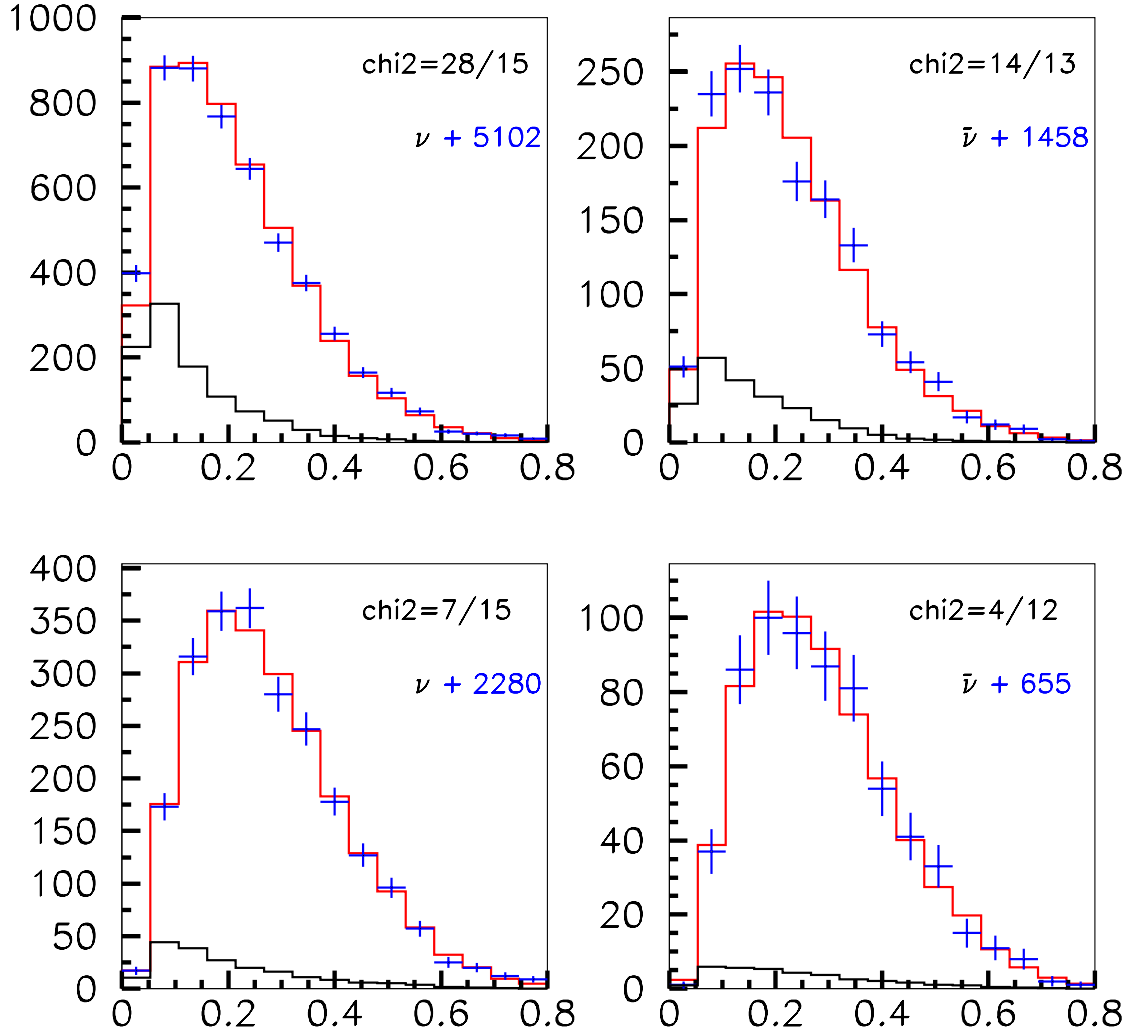


Figure 6.15: NuTeV  $z_{vis}$  distributions. Top - full sample, Bottom - only toroid-toroid events.  $\nu$ s are on the left,  $\bar{\nu}$ s are on the right.

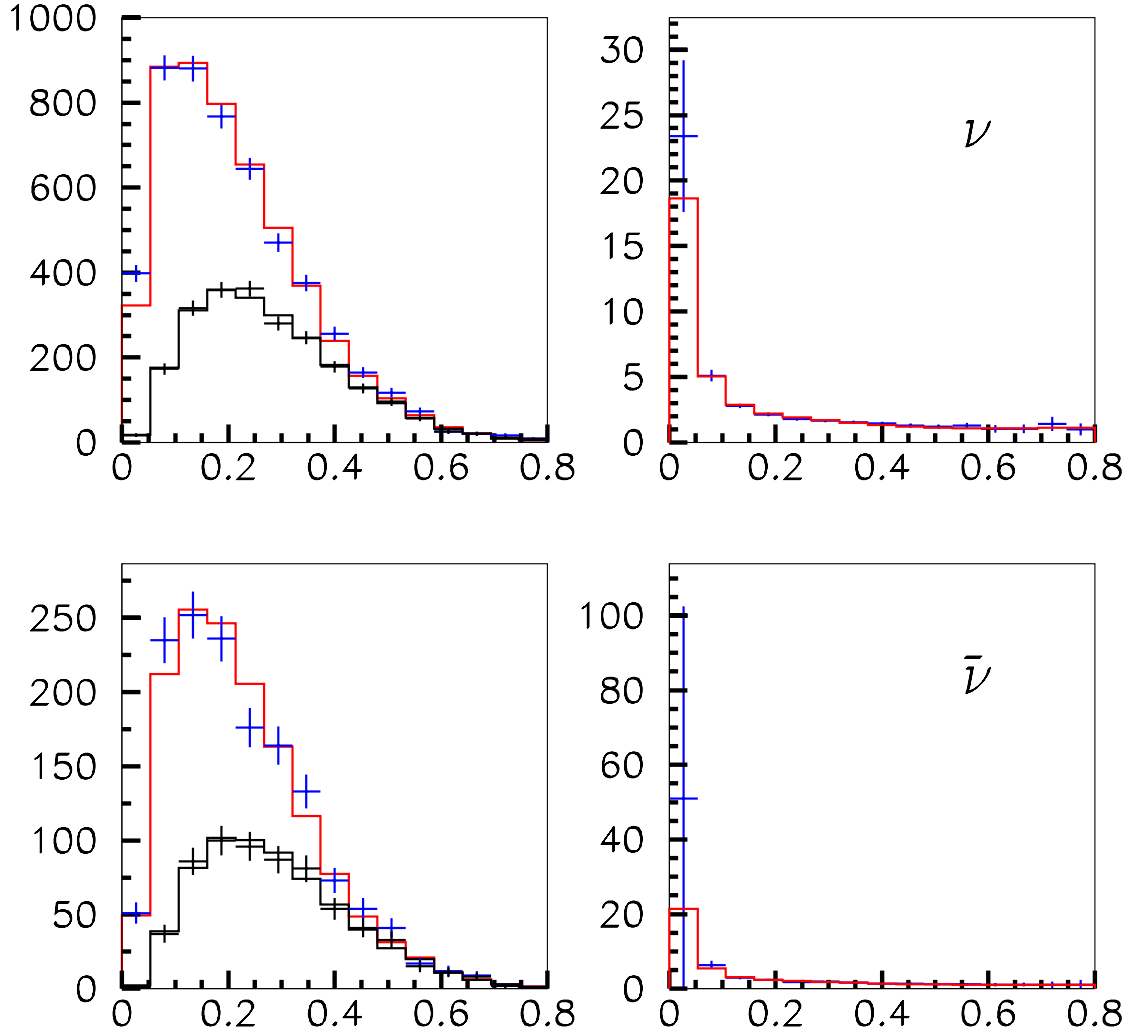


Figure 6.16: NuTeV  $z_{vis}$  distributions. Left - full sample vs. only toroid-toroid events. Right - the ratio of the histograms on the left side. Top -  $\nu$  mode, bottom -  $\bar{\nu}$  mode.

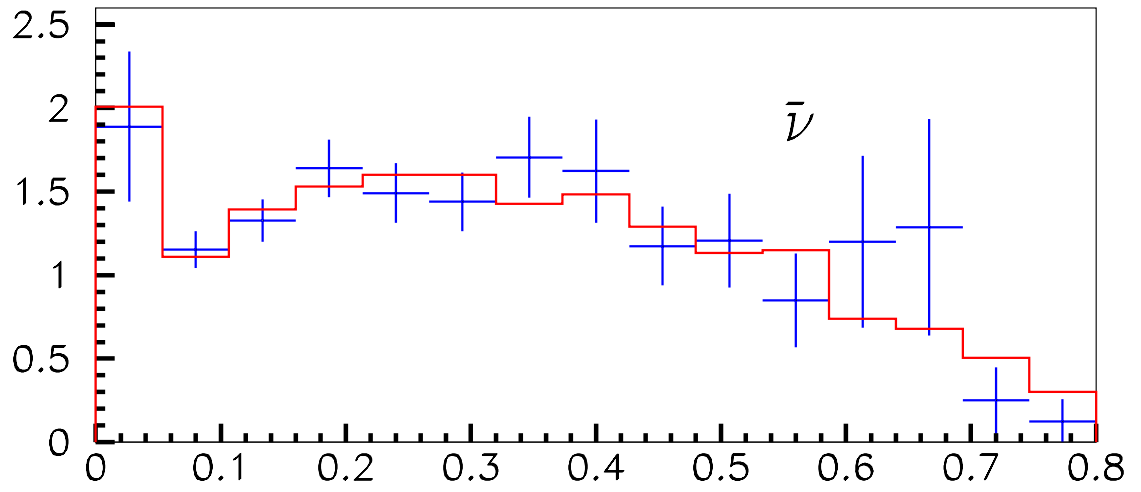
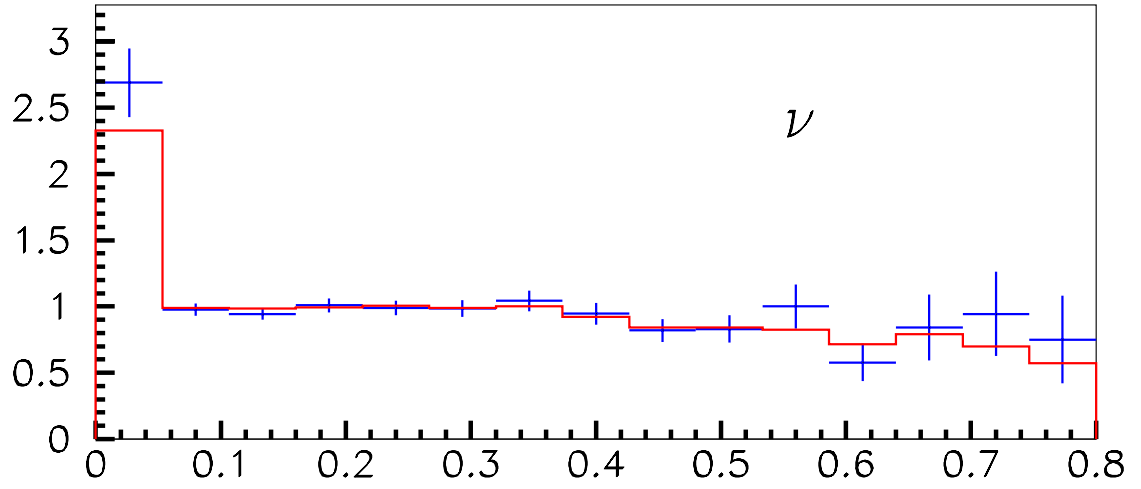


Figure 6.17: NuTeV and CCFR  $z_{vis}$  distributions. Top - NuTeV vs. CCFR. Bottom - the ratio of the histograms on the left side.

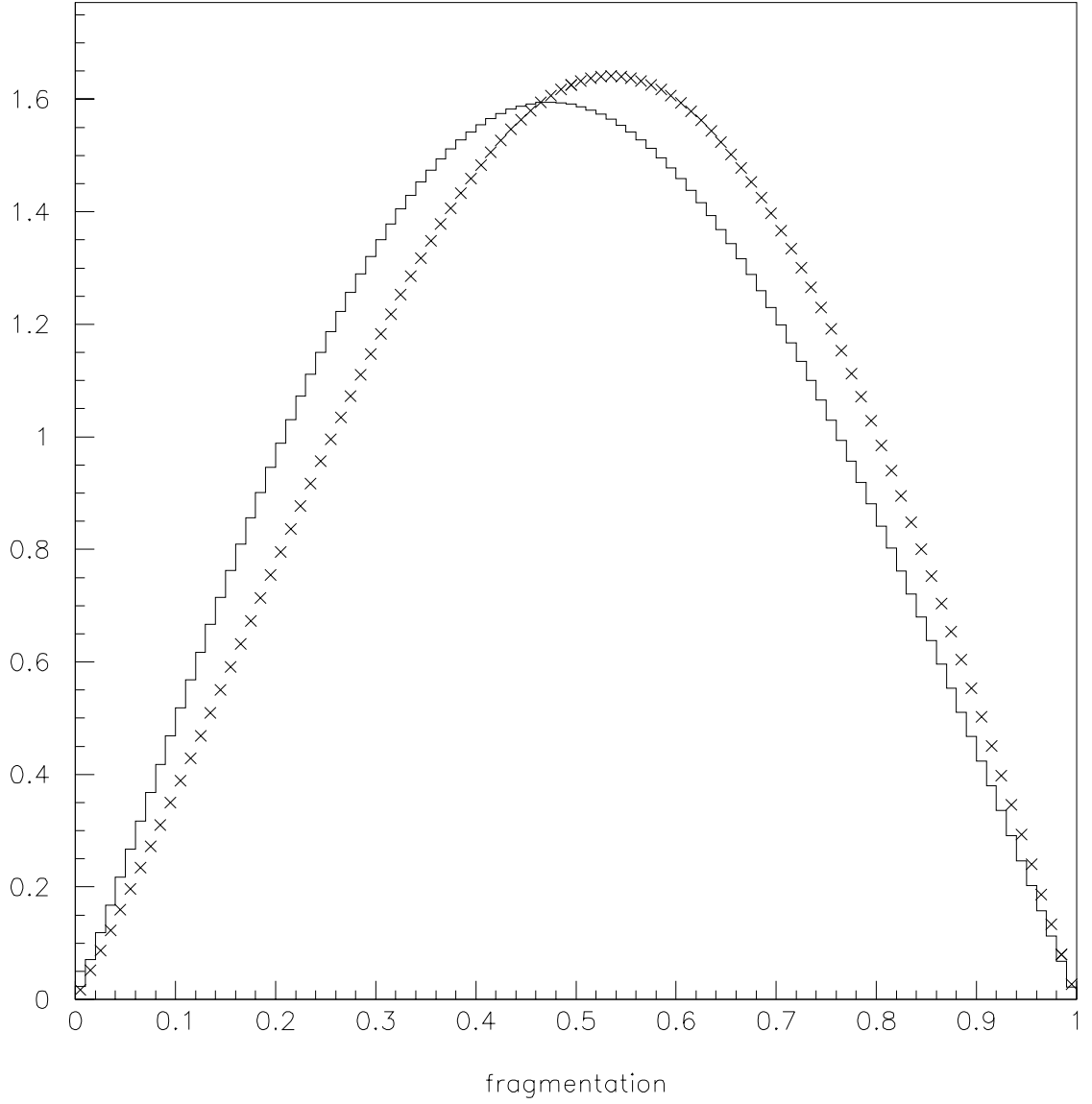


Figure 6.18: Fragmentation function for different  $\epsilon$ s. The higher the  $\epsilon$ , the more the function's peak is shifted to the left. Histogram represents NuTeV full sample, and crosses - NuTeV toroid-toroid sample.

## Chapter 7

# Dimuon Cross-Section Tables

As shown in the previous section, charm cross-section parameters depend on the details of the charm production model used in the fit. In addition, a fragmentation and decay model must be used to extract the charm production cross-section from the observed dimuon rate, introducing further model dependences. These model dependencies are exacerbated by the experimental smearing correction, due to the missing neutrino energy of the charmed hadron decay and the detector resolution, and the substantial acceptance correction for low energy muons. In order to minimize model dependencies, we choose to present our result in the form of a dimuon production cross-section.

It was shown in the previous chapter that we can obtain very good description of our dimuon data, independent of the charm production model assumptions in our Monte Carlo. We thus limit the use of the Monte Carlo to correct experimental effects to the measured dimuon rate, and we limit the measurement of this rate to regions of phase space where the acceptance of the experiment is high. In this case, the only model dependence comes from potential smearing effects close to our acceptance cuts, i.e., the uncertainty on production of events produced with kinematic variables outside our cuts that smeared to reconstructed values within the cuts. The prediction for this kind of smearing depends on the underlying

physics model, which is not well constrained by our data, since it involves phase space not accessed by our data. However, this model dependence is a second order effect.

The dimuon cross-section extraction procedure depends on the ability of our Monte Carlo to describe the data. The “true” three-dimensional phase space  $(x, y, E)$  is divided into a number of bins. The grid of bins is set up so that there is the same number of Monte Carlo events in each bin for any projection into one dimension. The cross-section for dimuon production with  $E_{\mu 2} \geq 5$  GeV is calculated according to Eq. 7.2 at the center of gravity of each bin. The size of the bins in “visible” phase space  $(x_{vis}, y_{vis}, E_{vis})$  is defined in such a way so that there is a correspondence between a visible bin  $j_i$  and a generated  $i$  established by the condition that bin  $j_i$  contains at least 60% of the events from bin  $i$ . The relative error on the cross-section is taken to be proportional to  $\delta_{\sigma_2}/\sigma_{2\mu} = \sigma_{2\mu}/\sqrt{D(j_i)}$ , with an adjustment factor added to take into account systematic errors. Cross-section tables were produced using BGPART, GRV, and CTEQ models; Fig.7.4-7.4 demonstrate the insensitivity of the cross-section to PDF choice. Further details of the binning procedure are defined in Section 7.2.

## 7.1 Dimuon Cross-Section

The analysis proceeds based on the observation that the *dimuon data* is well described by the LO fit. Whether the LO fit parameters have any useful meaning is, in fact, not of great importance; our goal is to use the fit parameters to help construct a cross-section. This task is performed by forming a grid of  $x, y$ , and  $E$  in the generated space. The dimuon cross-section is computed at the weighted center of each  $(x, y, E)_i$  bin  $i$  as

$$\frac{d^2\sigma_{\mu\mu}(\nu_\mu N \rightarrow \mu^- \mu^+ X)}{dx dy}(x, y, E)_i = \frac{D_i}{MC'_{iLOfit}} \int_{E_{\mu 2} > E_{\mu 2 \min}} dz d\Omega \times \left\{ \frac{d^3\sigma_{\mu\mu}(\nu_\mu N \rightarrow \mu^- \mu^+ X)}{dx dy dz} \right\}_{(x,y,E)_i - LOfit}. \quad (7.1)$$

In this expression the left hand side represents the measured cross-section for dimuon production as a function of  $x$ ,  $y$ , and  $E$  in bin  $i$  with the requirement that the second muon in the event exceeds the threshold used in the experiment,  $E_{\mu 2} > E_{\mu 2 \text{ min}}$ . On the right hand side,  $D_i$  is the number of data events in bin  $i$  that has to be evaluated from Monte Carlo,  $N'_{i \text{ LO fit}}$  is the number of events predicted in bin  $i$  by the LO fit. In the integrand  $d^3\sigma_{\mu\mu}(\nu_\mu N \rightarrow \mu^- \mu^+ X)/dx dy dz$  is from equation 6.1 and the integral over the fragmentation variable  $z$  and charmed hadron decay variables  $\Omega$  maintains the condition  $E_{\mu 2} > E_{\mu 2 \text{ min}}$ . The end result is two tables, one each for  $\nu_\mu$  and  $\bar{\nu}_\mu$  mode, of the “forward” dimuon cross-section, which is closest to what the experiment actually measures. It will be shown later that these tables can be used to re-extract the LO fit parameters and can be combined with similar tables from the CCFR experiment.

## 7.2 Data Unfolding

The integral on the right-hand side of equation 7.2 represents the leading order dimuon cross-section calculation using LO parameters that are obtained by fitting Monte Carlo to data. Figures A.1 show the calculated cross-section curves using three different different models. All curves lie close to each other which supports the claim that since best-fit Monte Carlo describes data equally well for all models the calculated cross-section in each case should be the same. The problem with just publishing these theoretical curves is that any physical measurement involves measuring central value as well as the error. Theoretical curves in our case represent just the central values with no errors attached to them. Another danger in just publishing these curves is that one might end up making the prediction in the region outside the phase space covered by the experiment.

In this analysis we report the differential cross-sections

$$d^2\sigma\left(\nu_\mu/\bar{\nu}_\mu Fe \rightarrow \mu^\mp \mu^\pm X\right)/dxdy$$

for forward secondary muons tabulated in bins of neutrino energy  $E$ , Bjorken



scaling variable  $x$ , and inelasticity  $y$ . The measurement is obtained by using a LO Monte Carlo fit to the data to find the correspondence (mapping) between the “true” (unsmeared) and reconstructed (smeared) phase space, as discussed in previous section. This procedure maps the statistical fluctuations of the observed event rate to the “true” phase space bins where the cross-section is reported. The consistency of the procedure is checked by comparing fits of various models to the extracted cross-section tables to fits of the same models performed directly to the data. The criterion for the check is that the obtained central values and the errors on the model parameters are the same in both cases. In order to meet these criteria the binning of the smeared and the unsmeared phase space has to be appropriately selected.

Usually in cross-section measurements, the procedure followed is to bin both the “true” and the reconstructed variables using the same grid, and select the bin size empirically so that for each bin the purity is maximized and the smearing contribution from other bins is minimized. Purity is defined here as the fraction of events which have both their unsmeared and smeared variables belonging to the same bin. In such a method the correspondence between smeared and unsmeared bins is trivial since the same grid of bins is used. In the case of the dimuon cross-section measurement, a complication arises from the large smearing effects due to the missing neutrino energy in the reconstructed dimuon final state. Unlike detector resolution effects, this smearing is not a symmetric function of the “true,” unsmeared variables, but rather an asymmetric mapping similar to an electroweak radiative correction. Because of this effect, we have followed a more elaborate procedure to map the visible phase space bins to those of the “true” phase space. This procedure allows us to obtain the desired high purity for each bin and also achieve stability of the result independently of the binning choice. In addition to mapping, our procedure allows us to take into account the significant bin-to-bin correlations which arise from the large smearing corrections without having to construct a full error matrix. This correlation matrix can be calculated, but it is too unwieldy to be useful. It is also difficult to incorporate effects of correlated

systematic errors in a meaningful way. In our treatment, we estimate an effective number of degrees of freedom which allows us to obtain from an *uncorrelated* fit to the cross-section tables the same fit parameter errors as the ones obtained by directly fitting to the data, using the usual  $\Delta\chi^2 = 1$  definition.

We begin the description of the technique by defining more precisely the factors  $D_i$  and  $\mathcal{N}'_{i,LOfit}$  from Eq. 7.2. In this equation, the expression on the left hand side represents the measured cross-section for dimuon production as a function of  $x$ ,  $y$ , and  $E$  in bin  $i$  of the true phase space (with the requirement  $E_{\mu 2} > E_{\mu 2 \min}$ ). On the right hand side,  $D_i$  is the number of data events in bin  $i$  (which has to be determined using the Monte Carlo mapping procedure), and  $N'_{i,LOfit}$  is the number of events predicted in bin  $i$  by the LO fit. To estimate the number of data events associated with bin  $i$ , we start by selecting bins in generated phase space  $(x, y, E)_i$ , requiring equal number of Monte Carlo events in each projection of the true (generated) phase space, so the number of events in each  $(x, y, E)_i$  bin is approximately the same. The visible phase space is divided using the same algorithm but with a much finer grid than used in generated space. The mapping matrix  $\mathcal{M}_{ij}$  makes the correspondence between visible and generated phase spaces:

$$\mathcal{M}_{ij} = \mathcal{N}_{ij} / \mathcal{N}_j,$$

where  $\mathcal{N}_{ij}$  is the number of Monte Carlo events generated in bin  $i$  which end up in visible bin  $j$  and  $\mathcal{N}_j$  is the total number of Monte Carlo events in visible bin  $j$ . The coverage fraction  $\mathcal{C}$  in visible space is defined as

$$\mathcal{C} = \sum_j^{N(\mathcal{C})} \mathcal{N}_{ij} / \mathcal{N}_i, \quad (7.2)$$

where  $\mathcal{N}_i$  is the number of Monte Carlo events in generated bin  $i$ . In the case of  $\mathcal{C} = 1$  the sum is performed over all visible bins; otherwise, the summation goes over the bins with the highest  $\mathcal{N}_{ij} / \mathcal{N}_i$  ratios until the desired fractional coverage is obtained. Using the above definitions, and for a given coverage  $\mathcal{C}$ , we can define the number of data events which belong to a given true phase space bin  $i$  (where

the cross-section is reported) as

$$D_i = \sum_{j \in \mathcal{C}} \mathcal{M}_{ij} \cdot D_j. \quad (7.3)$$

The number of Monte Carlo events in this generated bin, for a given coverage  $\mathcal{C}$ , is redefined as

$$\mathcal{N}'_i = \sum_{j \in \mathcal{C}} \mathcal{M}_{ij} \mathcal{N}_j. \quad (7.4)$$

The cross-section error for each bin  $i$  should be proportional to the visible events “mapped” in that bin, so the following expression is used to assign it:

$$\delta_i = \frac{d^2 \sigma_{\mu\mu}(\nu_\mu N \rightarrow \mu^- \mu^+ X)_i}{dx dy} / \sqrt{\mathcal{N}'_i}. \quad (7.5)$$

Note that the Monte Carlo statistics contribution comes from the total number of Monte Carlo events generated in bin  $i$ . The multiplicative factor  $D_i/\mathcal{N}'_i$  in Eq. 7.2 cancels out to first order the model dependence of the extracted cross-section and approximately transfers the statistical fluctuation in the visible phase space to the true phase space.

The procedure as described above is incomplete, since the true bins  $i$  are not statistically independent. As we stated in the introduction to this section, we do not calculate the full error matrix, but rather estimate an effective (independent) number of degrees of freedom. It is possible to estimate the number of independent degrees of freedom by calculating the contribution to the total number of degrees of freedom from each bin

$$DOF_i = \frac{\sum_{i \in \mathcal{C}} \mathcal{M}_{ij} \mathcal{N}_i}{\sum_{j \in \mathcal{C}} \mathcal{N}_j}. \quad (7.6)$$

It is obvious that the effective number of degrees of freedom depends on the selected coverage fraction  $\mathcal{C}$ , and should decrease as  $\mathcal{C}$  increases. Figure 7.1 shows the number of effective degrees of freedom (DOF) as a function of the coverage area  $\mathcal{C}$  (solid curve). The dotted curve in Fig. 7.1 shows the  $\chi^2$  obtained as a result of the fit to the table. We conclude that our method produces the correct number for  $\chi^2/DOF$ , if the effective number of degrees of freedom is used, for a coverage fraction between 55% and 90%.

The coverage area percentage used for our reported cross-section result is based on a Monte Carlo study. In this study a Monte Carlo sample is used to produce “cross-section” tables and then fits are performed to the tables and directly to the sample. Using as guidelines the criteria that there should be no pull on fit parameters in a fit to the cross-section table versus a direct fit, and that an *uncorrelated* fit to the tables should yield the same fit parameter errors as the ones obtained by a direct fit, we selected a coverage area  $\mathcal{C} = 60\%$ . The effective number of degrees of freedom which corresponds to this value should be used with all fits performed on the cross-section tables presented in this thesis.

### 7.3 Using The Table

Using the cross-section tables involves similar steps as used in the direct data analysis, but with all detector and flux dependent effects removed. One must provide a model for charm production, fragmentation, and decay; construct the dimuon cross-section number for each entry in the table; and perform a  $\chi^2$  fit. The  $\chi^2$  function should employ the statistical and systematic errors in each bin added in quadrature.

One must also account for correlations between the various table entries. These correlations derive from our use of the LO fit to parameterize the data and from our method of binning; they are an inherent consequence of the incomplete kinematic reconstruction of the dimuon final state. We have adopted a pragmatic approach towards handling this issue. Rather than compute a large correlation matrix, we inflate the cross-section errors in each bin by a factor that is typically 1.4. This factor is chosen so that an *uncorrelated*  $\chi^2$  fit to the tables returns the same parameter errors as a direct fit to the data.

We tested this fitting procedure on the tables using the same BGPARG, fragmentation, and decay models used to obtain the table; Table 7.1 summarizes this study. Both the parameter values and their uncertainties obtained from fitting

to the cross-section table agree with the corresponding values obtained by fitting directly to the data. It has also been verified that GRV94 parameters, for example, can be extracted from a cross-section table constructed with either the CTEQ or BGPART model so as to agree with parameters obtained by fitting directly to the data.

While our cross-checks in fitting the cross-section tables entail using the same physics model used in generating the tables, we emphasize that the table presents a set of physical observable which may be used to test *any* dimuon production model. For the most interesting case of dimuon production through charm, a typical model test would consist of the following steps <sup>1</sup>:

- For each bin, generate a (large) ensemble of  $N_{GEN}$  events with  $x$ ,  $y$ , and  $\vec{p}_c$ , where  $\vec{p}_c$  denotes the lab momentum of the produced charm quark, according to the model charm production differential cross-section  $d\sigma_{c-\text{mod}}/dx dy d\vec{p}_c$
- Fragment the charm quarks into hadrons and decay the charmed hadrons (using, for example, PYTHIA), and determine  $N_{PASS}$  the number of events which have a charm decay muon with  $E_{\mu 2} \geq 5$  GeV.
- The cross-section to compare to the table value is then  $d\sigma_{\mu\mu-\text{mod}}/dx dy = (N_{PASS}/N_{GEN}) \times \int d\vec{p}_c d\sigma_{c-\text{mod}}/dx dy d\vec{p}_c$ .
- A fit should then be performed to minimize

$$\chi^2 = \sum_{\text{table-bins}} \frac{\left(d^2\sigma_{\mu\mu-\text{mod}}/dx dy - d^2\sigma_{\mu\mu-\text{data}}^+/dx dy\right)^2}{\sigma_{\text{stat}}^2 + \sigma_{\text{sys}}^2} \quad (7.7)$$

in each beam mode with respect to the desired parameters in  $d\sigma_{c-\text{mod}}/dx dy d\vec{p}_c$ .

- The confidence level for the fit may be obtained by comparing the  $\chi^2$  to the sum of effective DOF for table bins used in the fit.

---

<sup>1</sup>A simple PYTHIA implementation of the first three steps may be obtained at [www-e815.fnal.gov](http://www-e815.fnal.gov), or by contacting the authors.

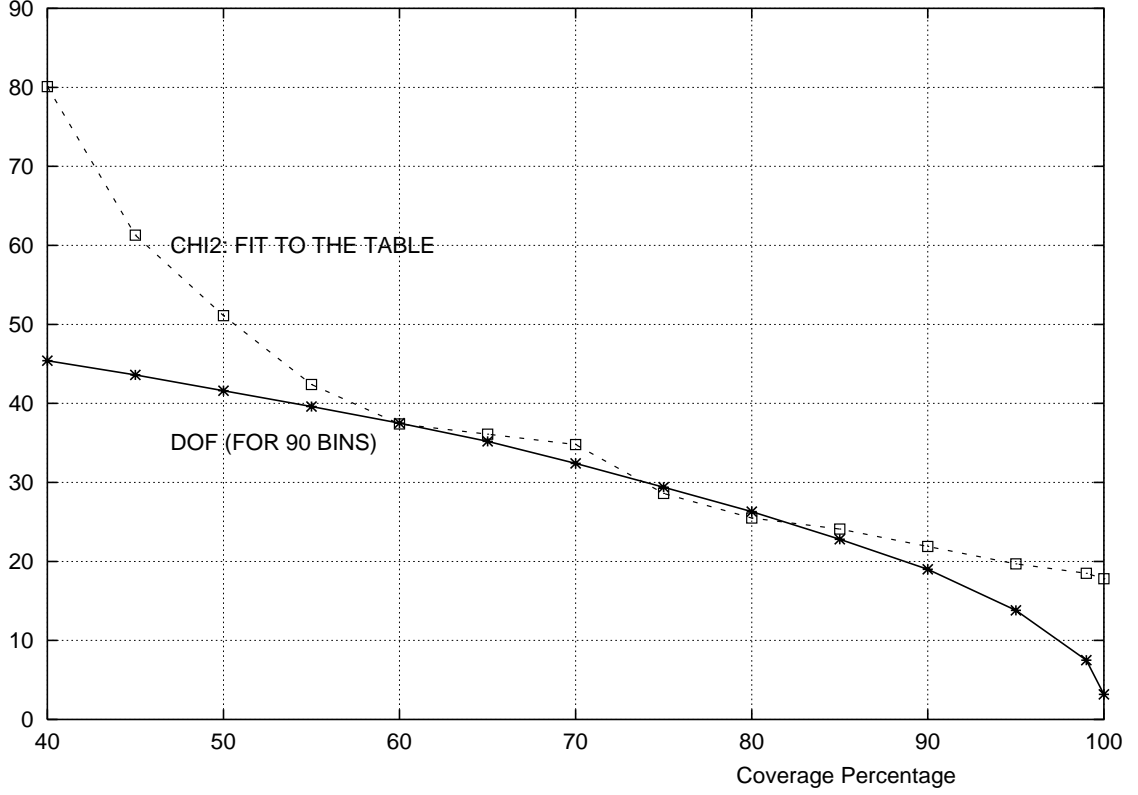


Figure 7.1: DOF and  $\chi^2$  as a function of coverage area

To provide further experimental information for model testing, the following kinematic quantities are given along with the cross-section in each bin:  $\langle E_{HAD} \rangle$ , the mean visible hadronic energy;  $\langle E_{\mu 2} \rangle$ , the mean energy of the secondary muon;  $\langle p_{T2in}^2 \rangle$ , the mean square of the secondary muon's transverse momentum in the event scattering plane; and  $\langle p_{T2out}^2 \rangle$ , the mean square of the secondary muons transverse momentum perpendicular to the event scattering plane. These quantities are computed from the dimuon data, with the LO fit used only for acceptance and smearing corrections. Tables A.1-A.12 contain the measurements<sup>2</sup>.

Summarizing, one can use the cross-section table to test model predictions. The  $\chi^2$  can be constructed assuming point to be statistically independent. The fit will produce the  $\chi^2$  that should be compared to the number of degrees of freedom that we provide.

---

<sup>2</sup>These data may also be obtained electronically at [www-e815.fnal.gov](http://www-e815.fnal.gov).

SET	$\mathbf{m}_c \text{ (GeV}/c^2\text{)}$	$\mathbf{B}_c \text{ (\%)}$	$\kappa$	$\bar{\kappa}$	$\alpha$	$\bar{\alpha}$
NuTeV	$1.30 \pm 0.22$	$10.22 \pm 1.11$	$0.38 \pm 0.08$	$0.39 \pm 0.06$	$-2.07 \pm 0.96$	$-2.42 \pm 0.45$
CCFR	$1.56 \pm 0.24$	$12.08 \pm 0.99$	$0.28 \pm 0.05$	$0.33 \pm 0.05$	$3.85 \pm 1.17$	$3.30 \pm 0.83$
NuTeV+	$1.40 \pm 0.16$	$11.00 \pm 0.71$	$0.36 \pm 0.05$	$0.38 \pm 0.04$	$-1.12 \pm 0.73$	$-2.07 \pm 0.39$

Table 7.1: Results of LO fits to the cross-section tables extracted from the NuTeV, CCFR, and combined data sets.

## 7.4 Validation of Cross Section Tables

A study using fake data is performed in order to ensure that the fit procedure is unbiased and to show that the cross section table construction does not introduce further significant biases. Forty fake data samples were generated using LO BG-PAR cross section parameters that were obtained from the fit to the real data. The fit is performed to each of those fake data samples. Figure 7.2 shows the result. The solid line represents the parameter used to produce the fake data sample. The result of the fit to this sample is denoted by the point with errorbar (40 total). The dashed line is the average over all 40 fake data sample. There are no significant pulls in any of the parameters. At the end of each fit to the fake sample the cross section table is constructed and the  $\chi^2$  fit is performed to this table. The result is shown on Fig.7.3. The fit to the table produces very high correlation between semi-muonic branching ratio and strange (anti-strange) size parameter. In reality one would fix the branching ratio to the world average. In this case there is no additional bias introduced in the tables.

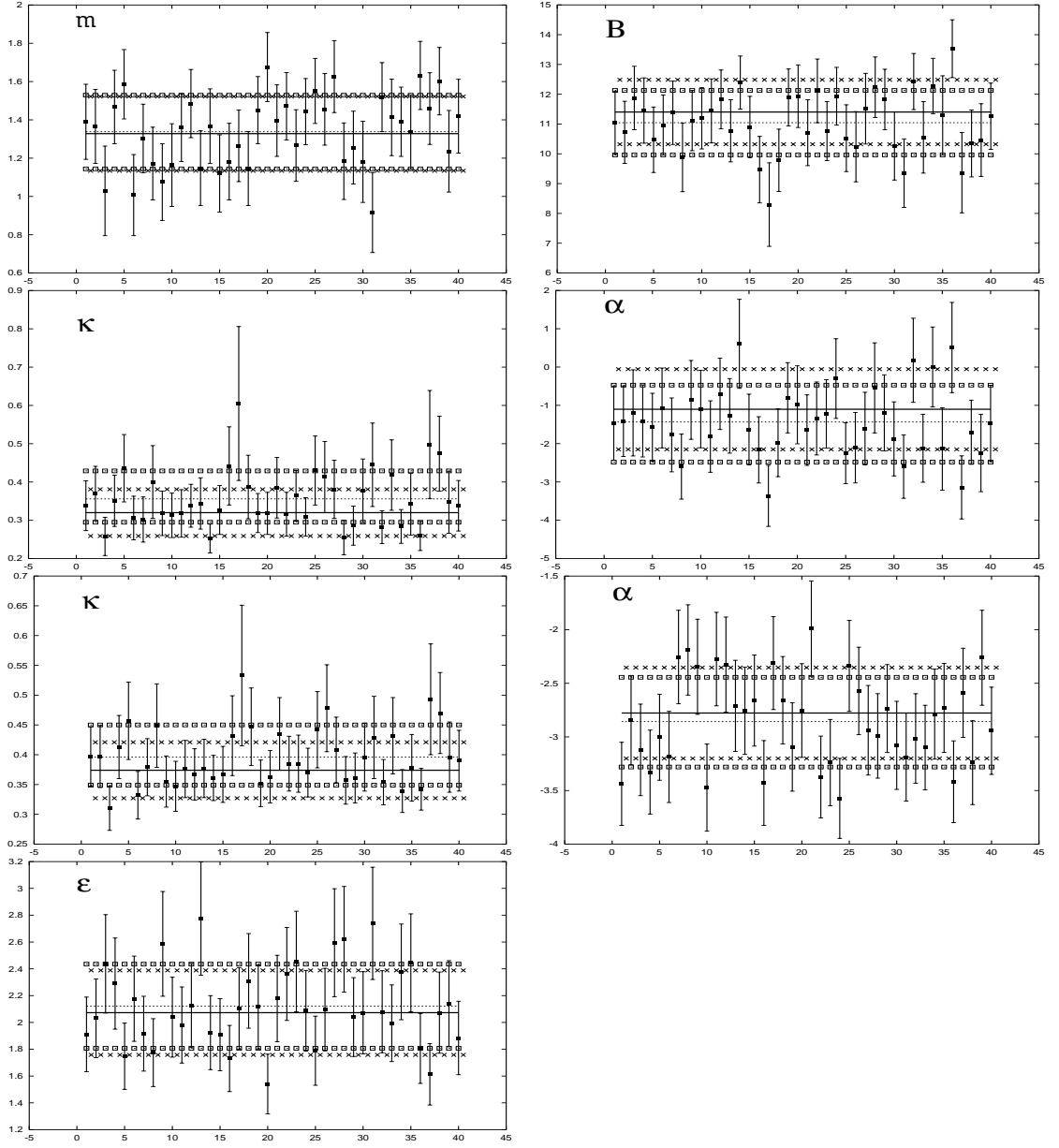


Figure 7.2: Pulls. Solid line - input parameter, dashed - average over fake data fits, crosses - errors on input parameters, squares - average error on fake data parameters. Points with errorbars represent the result of the fit to each fake data sample.



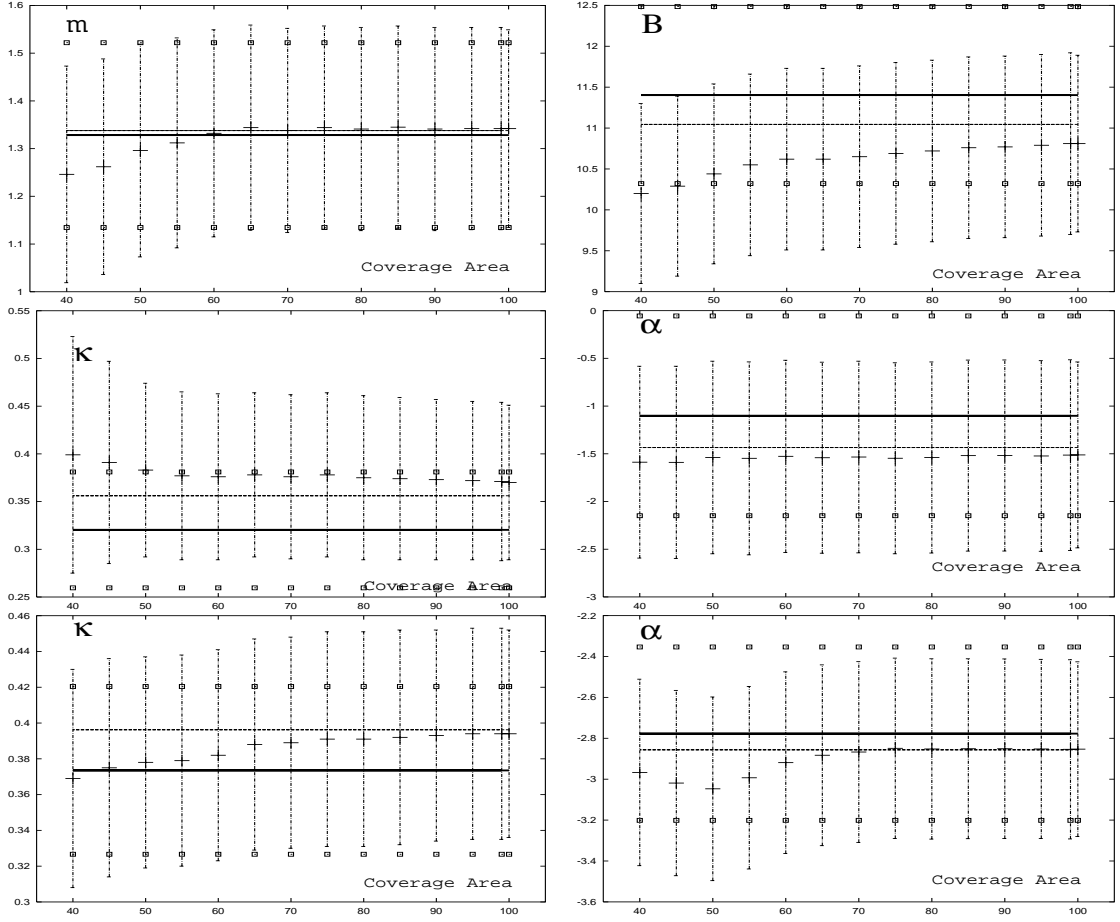


Figure 7.3: Pulls. Solid line - input parameter, dashed - average over fake data fits, squares - average error on input parameters (same as in Fig.7.2). Points with errorbars represent the average over all fits to the fake data tables. The result is shown as the function of the coverage area for each of the parameters.

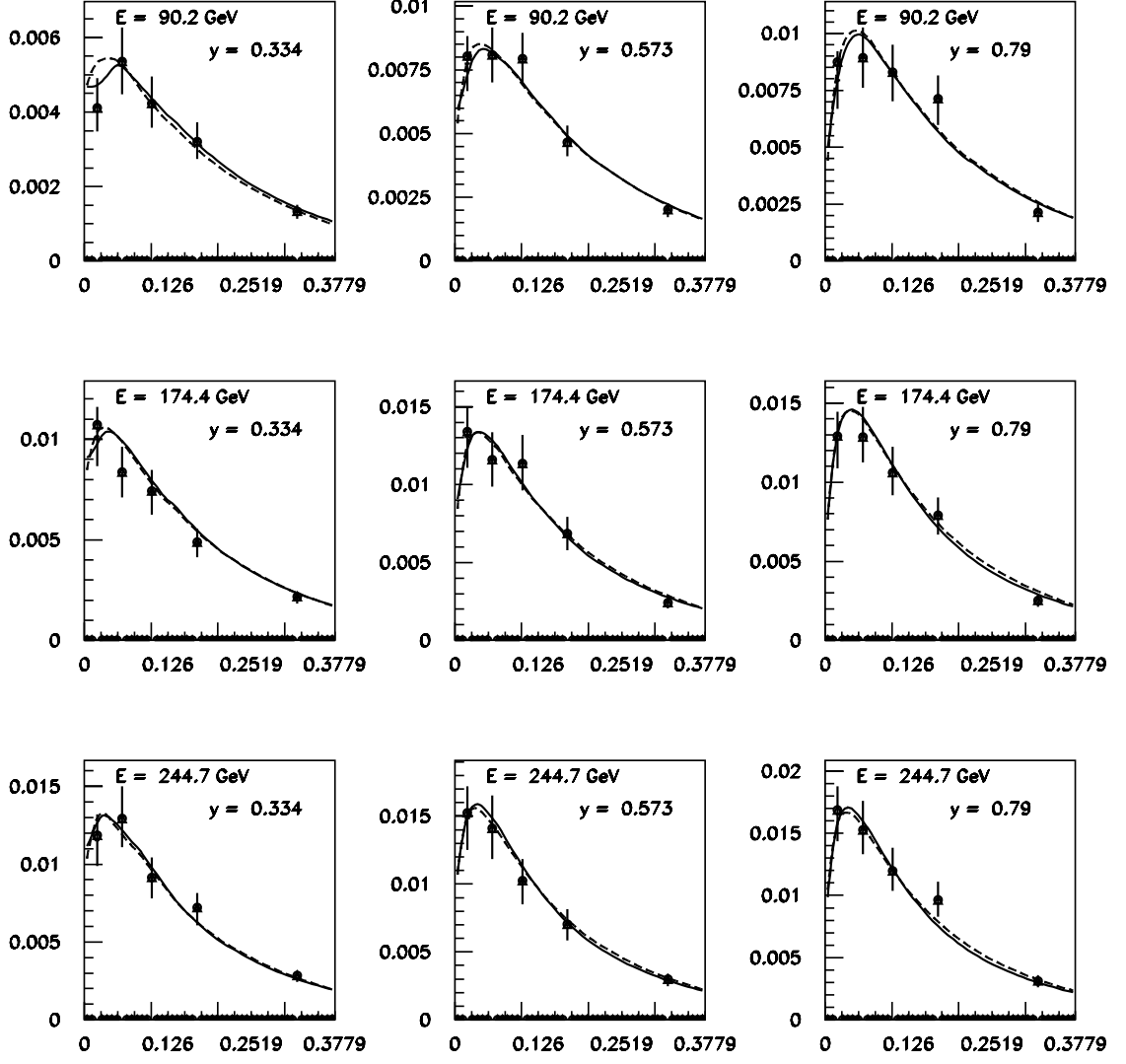


Figure 7.4:  $\sigma_{2\mu}(x)$  from NuTeV neutrinos, for various  $E_\nu - y$  bins in units of charged-current  $\sigma$ . The cross-section extracted using the BGPART model in the Monte Carlo is shown in squares, the circles correspond to extraction using the CTEQ model, and the triangles to the GRV model. The curves show the model prediction for GRV (dashed), CTEQ (dotted), and BGPART (solid) after the models have been fit to the data.

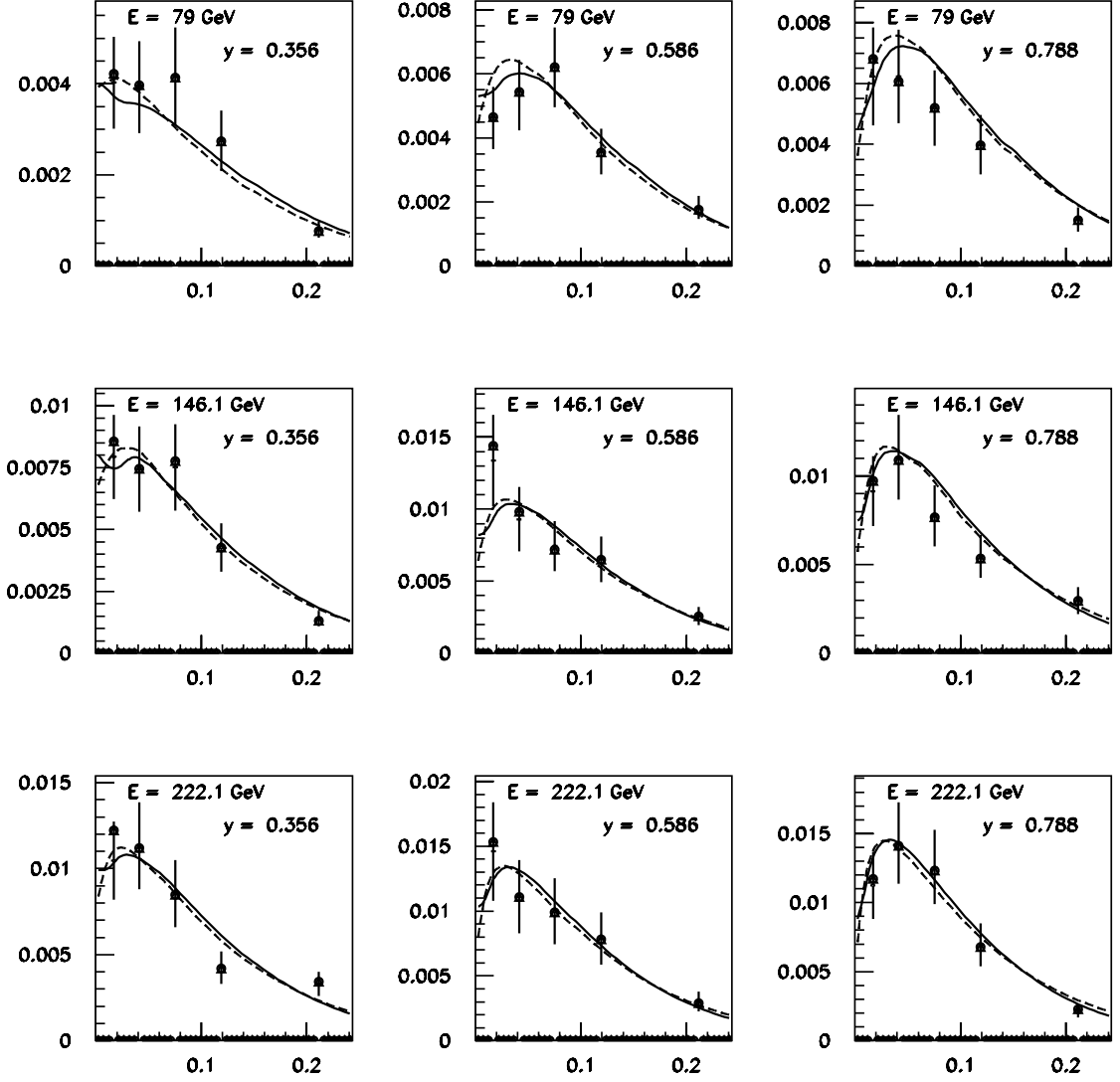


Figure 7.5:  $\sigma_{2\mu}(x)$  from NuTeV anti-neutrinos, for various  $E_\nu - y$  bins in units of charged-current  $\sigma$ . The cross-section extracted using the BGPAR model in the Monte Carlo is shown in squares, the circles correspond to extraction using the CTEQ model, and the triangles to the GRV model. The curves show the model prediction for GRV (dashed), CTEQ (dotted), and BGPAR (solid) after the models have been fit to the data.

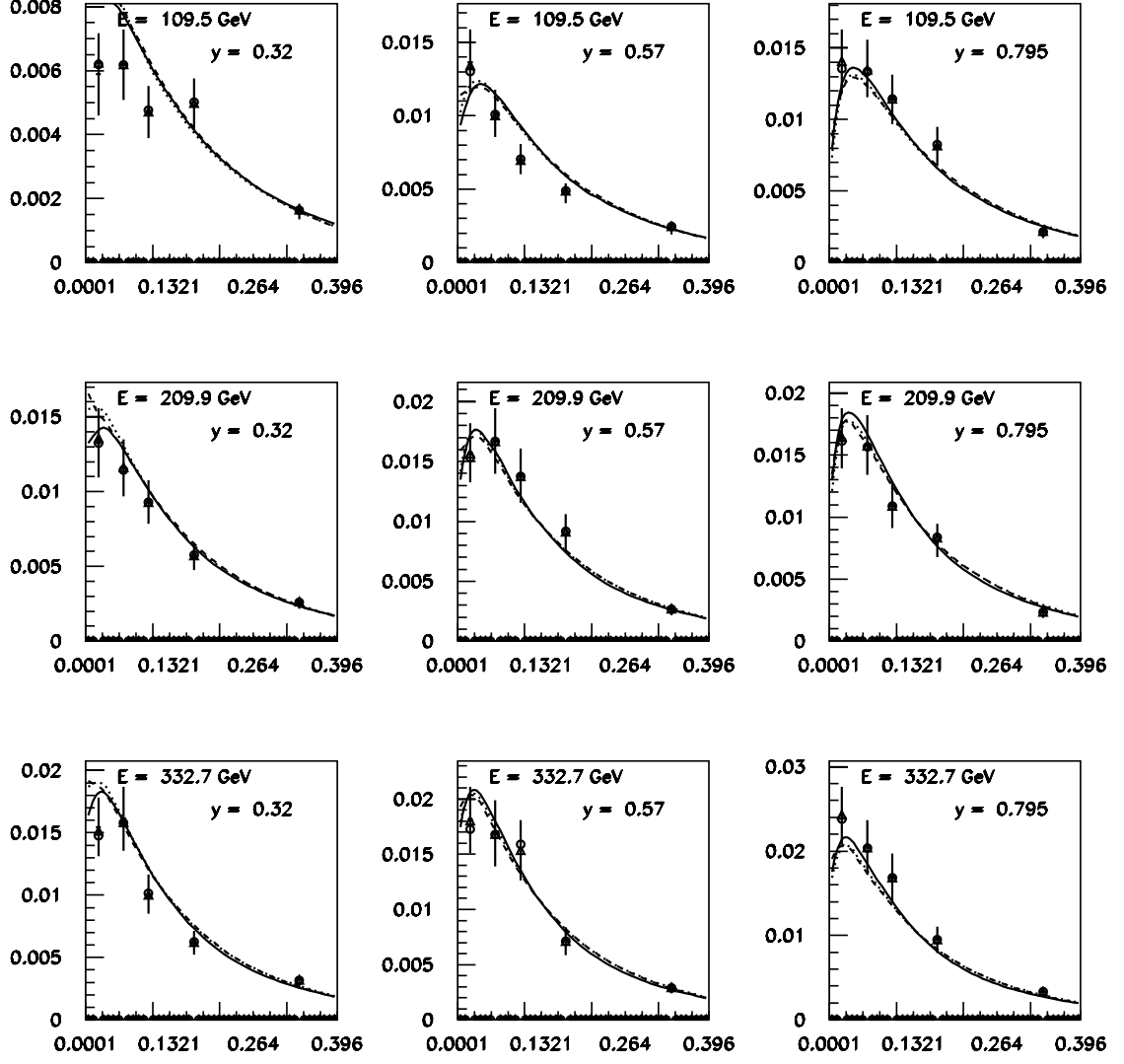


Figure 7.6:  $\sigma_{2\mu}(x)$  from CCFR neutrinos, for various  $E_\nu - y$  bins in units of charged-current  $\sigma$ . The cross-section extracted using the BGP model in the Monte Carlo is shown in squares, the circles correspond to extraction using the CTEQ model, and the triangles to the GRV model. The curves show the model prediction for GRV (dashed), CTEQ (dotted), and BGP (solid) after the models have been fit to the data.

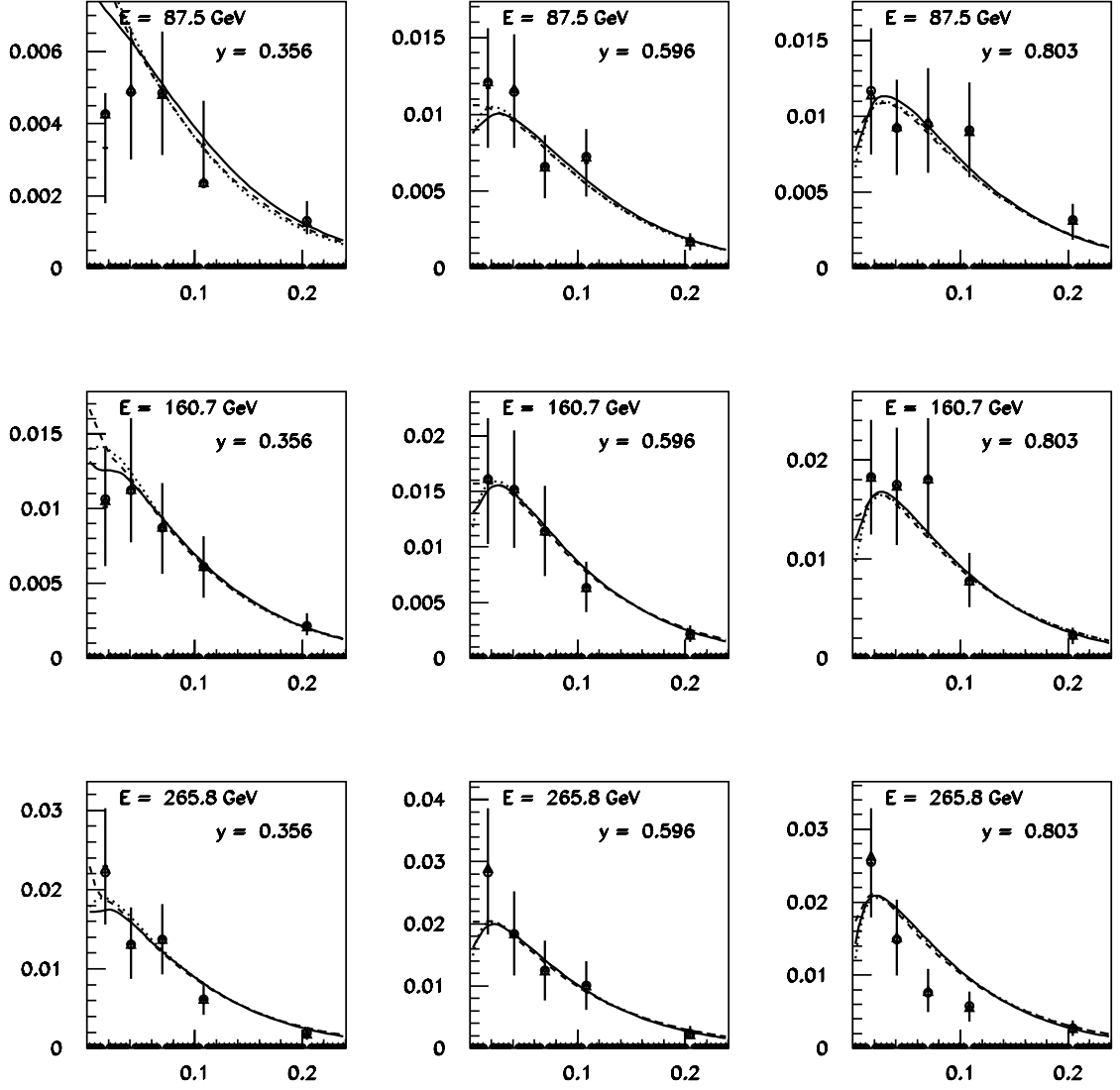


Figure 7.7:  $\sigma_{2\mu}(x)$  from CCFR anti-neutrinos, for various  $E_\nu - y$  bins in units of charged-current  $\sigma$ . The cross-section extracted using the BGPART model in the Monte Carlo is shown in squares, the circles correspond to extraction using the CTEQ model, and the triangles to the GRV model. The curves show the model prediction for GRV (dashed), CTEQ (dotted), and BGPART (solid) after the models have been fit to the data.

## Chapter 8

### Summary

This thesis presents for the first time a measurement of the dimuon production cross-section from an analysis of the data of the NuTeV neutrino DIS experiment at the Tevatron. NuTeV data are combined with an earlier measurement from the CCFR experiment that used the same detector but a different beamline. A leading order QCD analysis of charm production performed on the combined data yields the smallest errors to date on model parameters describing the charm mass, the size and shape of the strange sea, and the mean semi-muonic branching fraction of charm. The leading order QCD model describes NuTeV and CCFR data very well, but charm production model parameters extracted vary depending on the particular choice of model. The extracted dimuon production cross-section, by contrast, is insensitive to the choice of leading order QCD model and should be of most use to the community of phenomenologists. In LO QCD, all models predict strange (anti-strange) sea to be  $\sim 40\%$  of non-strange sea. There is no strange - anti-strange asymmetry in  $x$  region accessible by our data. NuTeV directly measures  $V_{cd}$  matrix element to be

$$V_{cd} = 0.244 \pm 0.017 \pm 0.017.$$

This is in good agreement with previous CCFR measurement. Combining NuTeV  $V_{cd}$  with CCFR, we present the most precise measurement of

$$V_{cd} = 0.242 \pm 0.011 \pm 0.017.$$

This thesis provides all necessary information to make predictions about potential strange - anti-strange sea asymmetry in high  $x$  region.

Future neutrino studies at MUon RIng Neutrino Experiment (MURINE) [42] will be much cleaner theoretically due to much superior statistics available and due to improvements in the detector. A muon collider at the center-of-mass energies between 100-1000 TeV would produce a neutrino beam to study deep inelastic scattering processes with center-of-mass energies of 300-1000 GeV. A neutrino beam from the muon storage ring would be several orders of magnitude more intense than NuTeV's or CCFR's beams. Neutrinos would be produced as the result of muon decays, emanating tangentially out the muon ring in a very focused beam. Therefor, the target can be very small, and a silicon detector can be used to tag the charm hadron by its lifetime. This makes the charm production analysis much easier since there is no need for fragmentation and decay model assumptions.

# Appendix A

## Cross Section Tables

$\chi^2$	<b>x</b>	<b>y</b>	$\frac{d\sigma(\nu_\mu N \rightarrow \mu^- \mu^+ X)}{dx dy} \big _+$	$\langle E_{HAD} \rangle$	$\langle E_{\mu^+} \rangle$	$\langle p_{T\mu^+ in}^2 \rangle$	$\langle p_{T\mu^+ out}^2 \rangle$
0.64	0.021	0.334	$0.419 \pm 0.071 \pm 0.003$	$18.3 \pm 1.0$	$7.9 \pm 0.5$	$0.40 \pm 0.55$	$0.14 \pm 0.24$
0.45	0.058	0.334	$0.538 \pm 0.090 \pm 0.022$	$18.6 \pm 1.2$	$9.0 \pm 0.6$	$1.08 \pm 1.14$	$0.76 \pm 1.49$
0.44	0.102	0.334	$0.427 \pm 0.069 \pm 0.007$	$17.9 \pm 1.2$	$8.3 \pm 0.7$	$1.19 \pm 0.78$	$0.26 \pm 0.48$
0.46	0.168	0.334	$0.323 \pm 0.049 \pm 0.008$	$18.7 \pm 1.2$	$8.2 \pm 0.5$	$0.74 \pm 0.28$	$0.14 \pm 0.25$
0.67	0.324	0.334	$0.132 \pm 0.019 \pm 0.003$	$19.4 \pm 0.9$	$8.5 \pm 0.4$	$0.95 \pm 0.09$	$0.07 \pm 0.04$
0.64	0.021	0.573	$0.774 \pm 0.107 \pm 0.015$	$36.3 \pm 1.4$	$10.9 \pm 0.8$	$0.19 \pm 0.09$	$0.09 \pm 0.03$
0.46	0.058	0.573	$0.808 \pm 0.108 \pm 0.027$	$34.3 \pm 1.5$	$10.9 \pm 0.7$	$0.29 \pm 0.14$	$0.11 \pm 0.07$
0.47	0.102	0.573	$0.792 \pm 0.103 \pm 0.012$	$36.5 \pm 1.5$	$10.0 \pm 0.6$	$1.08 \pm 0.97$	$0.44 \pm 0.96$
0.50	0.168	0.573	$0.471 \pm 0.060 \pm 0.017$	$34.8 \pm 1.6$	$10.6 \pm 0.7$	$0.85 \pm 0.72$	$0.25 \pm 0.43$
0.62	0.324	0.573	$0.198 \pm 0.027 \pm 0.003$	$34.6 \pm 1.6$	$11.1 \pm 0.7$	$0.75 \pm 0.11$	$0.07 \pm 0.03$
0.58	0.021	0.790	$0.795 \pm 0.126 \pm 0.096$	$49.6 \pm 3.0$	$14.6 \pm 1.4$	$0.26 \pm 0.35$	$0.10 \pm 0.05$
0.43	0.058	0.790	$0.894 \pm 0.133 \pm 0.029$	$52.8 \pm 2.5$	$13.5 \pm 1.5$	$0.34 \pm 0.35$	$0.24 \pm 0.44$
0.41	0.102	0.790	$0.826 \pm 0.123 \pm 0.027$	$52.1 \pm 2.5$	$11.2 \pm 1.0$	$0.24 \pm 0.21$	$0.09 \pm 0.08$
0.52	0.168	0.790	$0.706 \pm 0.108 \pm 0.005$	$53.0 \pm 2.5$	$12.6 \pm 1.2$	$0.30 \pm 0.15$	$0.10 \pm 0.08$
0.58	0.324	0.790	$0.210 \pm 0.038 \pm 0.004$	$49.0 \pm 2.9$	$12.8 \pm 1.2$	$0.52 \pm 0.18$	$0.09 \pm 0.04$

Table A.1: NuTeV forward differential cross-section for  $\nu_\mu N \rightarrow \mu^- \mu^+ X$  at  $E \sim 90.18$  GeV. The forward cross-section requires  $E_{\mu^+} \geq 5$  GeV, and the cross-section values should be multiplied by  $\frac{1}{100} \times G_F^2 M E / \pi$ . The first error given for the cross-sections is statistical and the second systematic. Units are in GeV or  $\text{GeV}^2$ , where appropriate, for the averages of the kinematic quantities.



$\chi^2$	$\mathbf{x}$	$\mathbf{y}$	$\frac{d\sigma(\nu_\mu N \rightarrow \mu^- \mu^+ X)}{dx dy} _+$	$\langle E_{HAD} \rangle$	$\langle E_{\mu^+} \rangle$	$\langle p_{T\mu^+ in}^2 \rangle$	$\langle p_{T\mu^+ out}^2 \rangle$
0.66	0.021	0.334	$1.013 \pm 0.148 \pm 0.022$	$39.1 \pm 1.8$	$12.1 \pm 1.0$	$0.57 \pm 1.32$	$0.24 \pm 0.49$
0.45	0.058	0.334	$0.837 \pm 0.127 \pm 0.018$	$39.6 \pm 2.1$	$12.2 \pm 1.1$	$0.33 \pm 0.09$	$0.09 \pm 0.04$
0.40	0.102	0.334	$0.737 \pm 0.111 \pm 0.009$	$39.8 \pm 2.3$	$12.2 \pm 1.1$	$0.57 \pm 0.17$	$0.08 \pm 0.03$
0.39	0.168	0.334	$0.484 \pm 0.071 \pm 0.010$	$38.4 \pm 2.2$	$11.3 \pm 0.9$	$0.69 \pm 0.15$	$0.11 \pm 0.10$
0.57	0.324	0.334	$0.212 \pm 0.028 \pm 0.005$	$39.4 \pm 1.8$	$12.7 \pm 0.8$	$1.44 \pm 0.20$	$0.08 \pm 0.03$
0.57	0.021	0.573	$1.304 \pm 0.196 \pm 0.015$	$69.0 \pm 2.3$	$18.1 \pm 1.8$	$0.19 \pm 0.07$	$0.11 \pm 0.06$
0.43	0.058	0.573	$1.161 \pm 0.176 \pm 0.021$	$71.0 \pm 2.5$	$16.7 \pm 1.5$	$0.25 \pm 0.08$	$0.08 \pm 0.04$
0.35	0.102	0.573	$1.140 \pm 0.178 \pm 0.019$	$72.9 \pm 3.2$	$19.2 \pm 2.1$	$0.63 \pm 0.24$	$0.26 \pm 0.78$
0.42	0.168	0.573	$0.685 \pm 0.107 \pm 0.007$	$75.0 \pm 3.2$	$14.8 \pm 1.6$	$1.35 \pm 1.26$	$0.15 \pm 0.27$
0.52	0.324	0.573	$0.242 \pm 0.038 \pm 0.004$	$76.8 \pm 3.3$	$13.6 \pm 1.6$	$0.74 \pm 0.24$	$0.07 \pm 0.04$
0.43	0.021	0.790	$1.267 \pm 0.179 \pm 0.025$	$101.8 \pm 3.6$	$22.0 \pm 2.8$	$0.20 \pm 0.09$	$0.11 \pm 0.05$
0.34	0.058	0.790	$1.301 \pm 0.176 \pm 0.031$	$101.5 \pm 3.2$	$21.1 \pm 2.4$	$0.29 \pm 0.11$	$0.09 \pm 0.04$
0.32	0.102	0.790	$1.072 \pm 0.153 \pm 0.023$	$98.7 \pm 3.6$	$21.9 \pm 3.1$	$0.37 \pm 0.17$	$0.09 \pm 0.05$
0.37	0.168	0.790	$0.788 \pm 0.118 \pm 0.020$	$101.9 \pm 4.3$	$20.4 \pm 3.3$	$0.72 \pm 0.65$	$0.09 \pm 0.06$
0.41	0.324	0.790	$0.251 \pm 0.040 \pm 0.005$	$100.4 \pm 4.2$	$20.2 \pm 3.1$	$0.69 \pm 0.40$	$0.08 \pm 0.07$

Table A.2: NuTeV forward differential cross-section for  $\nu_\mu N \rightarrow \mu^- \mu^+ X$  at  $E \sim 174.37$  GeV. The forward cross-section requires  $E_{\mu^+} \geq 5$  GeV, and the cross-section values should be multiplied by  $\frac{1}{100} \times G_F^2 M E / \pi$ . The first error given for the cross-sections is statistical and the second systematic. Units are in GeV or  $\text{GeV}^2$ , where appropriate, for the averages of the kinematic quantities.

$\chi^2$	$\mathbf{x}$	$\mathbf{y}$	$\frac{d\sigma(\nu_\mu N \rightarrow \mu^- \mu^+ X)}{dx dy} _+$	$\langle E_{HAD} \rangle$	$\langle E_{\mu^+} \rangle$	$\langle p_{T\mu^+ in}^2 \rangle$	$\langle p_{T\mu^+ out}^2 \rangle$
0.79	0.021	0.334	$1.154 \pm 0.167 \pm 0.015$	$54.7 \pm 2.9$	$15.1 \pm 1.5$	$0.82 \pm 1.29$	$0.09 \pm 0.05$
0.54	0.058	0.334	$1.306 \pm 0.196 \pm 0.034$	$59.2 \pm 3.1$	$14.2 \pm 1.3$	$0.31 \pm 0.10$	$0.29 \pm 0.40$
0.46	0.102	0.334	$0.913 \pm 0.132 \pm 0.017$	$61.1 \pm 4.5$	$13.2 \pm 1.6$	$0.40 \pm 0.11$	$0.11 \pm 0.14$
0.41	0.168	0.334	$0.712 \pm 0.103 \pm 0.013$	$65.6 \pm 3.3$	$14.1 \pm 1.4$	$0.82 \pm 0.18$	$0.09 \pm 0.03$
0.63	0.324	0.334	$0.278 \pm 0.036 \pm 0.003$	$69.7 \pm 3.5$	$13.8 \pm 1.2$	$1.29 \pm 0.30$	$0.11 \pm 0.10$
0.68	0.021	0.573	$1.487 \pm 0.234 \pm 0.010$	$97.7 \pm 3.8$	$20.1 \pm 3.0$	$0.19 \pm 0.09$	$0.14 \pm 0.16$
0.47	0.058	0.573	$1.419 \pm 0.235 \pm 0.016$	$105.7 \pm 3.9$	$19.7 \pm 2.6$	$0.84 \pm 0.98$	$0.10 \pm 0.09$
0.46	0.102	0.573	$1.018 \pm 0.166 \pm 0.011$	$105.5 \pm 6.1$	$21.2 \pm 3.9$	$0.85 \pm 0.62$	$0.13 \pm 0.52$
0.42	0.168	0.573	$0.700 \pm 0.116 \pm 0.005$	$108.1 \pm 4.9$	$17.5 \pm 3.4$	$0.78 \pm 0.34$	$0.10 \pm 0.07$
0.60	0.324	0.573	$0.294 \pm 0.046 \pm 0.003$	$109.6 \pm 4.5$	$18.6 \pm 2.7$	$0.86 \pm 0.27$	$0.08 \pm 0.04$
0.56	0.021	0.790	$1.656 \pm 0.222 \pm 0.060$	$148.9 \pm 4.9$	$22.6 \pm 3.3$	$0.19 \pm 0.11$	$0.16 \pm 0.20$
0.43	0.058	0.790	$1.546 \pm 0.216 \pm 0.013$	$144.3 \pm 5.5$	$27.6 \pm 4.5$	$0.40 \pm 0.20$	$0.13 \pm 0.17$
0.40	0.102	0.790	$1.211 \pm 0.174 \pm 0.046$	$149.9 \pm 7.2$	$25.4 \pm 4.4$	$1.25 \pm 1.19$	$0.26 \pm 0.51$
0.36	0.168	0.790	$0.968 \pm 0.141 \pm 0.011$	$150.4 \pm 6.9$	$22.2 \pm 3.5$	$0.52 \pm 0.32$	$0.48 \pm 1.98$
0.37	0.324	0.790	$0.311 \pm 0.047 \pm 0.005$	$154.6 \pm 6.3$	$19.2 \pm 3.6$	$0.50 \pm 0.26$	$0.07 \pm 0.04$

Table A.3: NuTeV forward differential cross-section for  $\nu_\mu N \rightarrow \mu^- \mu^+ X$  at  $E \sim 244.72$  GeV. The forward cross-section requires  $E_{\mu^+} \geq 5$  GeV, and the cross-section values should be multiplied by  $\frac{1}{100} \times G_F^2 M E / \pi$ . The first error given for the cross-sections is statistical and the second systematic. Units are in GeV or  $\text{GeV}^2$ , where appropriate, for the averages of the kinematic quantities.

$\chi^2$	$\mathbf{x}$	$\mathbf{y}$	$\frac{d\sigma(\bar{\nu}_\mu N \rightarrow \mu^+ \mu^- X)}{dx dy} _+$	$\langle E_{HAD} \rangle$	$\langle E_{\mu^-} \rangle$	$\langle p_{T\mu^-}^2 \rangle$	$\langle p_{T\mu^-}^2 \rangle_{out}$
0.61	0.016	0.356	$0.403 \pm 0.101 \pm 0.004$	$16.9 \pm 1.3$	$7.5 \pm 0.8$	$0.11 \pm 0.07$	$0.06 \pm 0.06$
0.39	0.044	0.356	$0.393 \pm 0.101 \pm 0.019$	$15.9 \pm 1.9$	$8.2 \pm 1.0$	$1.34 \pm 1.80$	$0.59 \pm 1.57$
0.34	0.075	0.356	$0.417 \pm 0.107 \pm 0.007$	$16.5 \pm 1.6$	$7.9 \pm 1.1$	$0.42 \pm 0.33$	$0.11 \pm 0.13$
0.37	0.117	0.356	$0.275 \pm 0.067 \pm 0.025$	$16.5 \pm 1.5$	$8.4 \pm 0.7$	$0.37 \pm 0.19$	$0.12 \pm 0.13$
0.63	0.211	0.356	$0.080 \pm 0.018 \pm 0.003$	$18.5 \pm 1.9$	$8.0 \pm 0.9$	$0.74 \pm 0.23$	$0.08 \pm 0.06$
0.61	0.016	0.586	$0.463 \pm 0.097 \pm 0.030$	$30.5 \pm 2.2$	$13.0 \pm 1.9$	$0.19 \pm 0.09$	$0.05 \pm 0.04$
0.39	0.044	0.586	$0.533 \pm 0.110 \pm 0.007$	$31.1 \pm 2.5$	$10.3 \pm 1.4$	$0.17 \pm 0.08$	$0.11 \pm 0.05$
0.42	0.075	0.586	$0.621 \pm 0.125 \pm 0.026$	$33.5 \pm 2.2$	$10.7 \pm 1.4$	$0.32 \pm 0.17$	$0.05 \pm 0.05$
0.44	0.117	0.586	$0.357 \pm 0.071 \pm 0.008$	$31.5 \pm 2.4$	$11.1 \pm 1.3$	$0.35 \pm 0.13$	$0.09 \pm 0.06$
0.63	0.211	0.586	$0.183 \pm 0.036 \pm 0.003$	$32.2 \pm 2.3$	$10.7 \pm 1.2$	$0.94 \pm 0.39$	$0.07 \pm 0.04$
0.53	0.016	0.788	$0.623 \pm 0.161 \pm 0.009$	$43.7 \pm 3.8$	$12.1 \pm 1.6$	$0.14 \pm 0.13$	$0.13 \pm 0.20$
0.39	0.044	0.788	$0.623 \pm 0.154 \pm 0.016$	$44.8 \pm 4.3$	$10.1 \pm 1.8$	$0.10 \pm 0.08$	$0.04 \pm 0.03$
0.42	0.075	0.788	$0.520 \pm 0.124 \pm 0.004$	$43.4 \pm 3.7$	$13.4 \pm 3.3$	$0.19 \pm 0.11$	$0.10 \pm 0.09$
0.41	0.117	0.788	$0.399 \pm 0.098 \pm 0.016$	$41.1 \pm 5.2$	$11.9 \pm 2.7$	$0.30 \pm 0.21$	$0.09 \pm 0.10$
0.64	0.211	0.788	$0.153 \pm 0.039 \pm 0.004$	$46.8 \pm 5.1$	$10.0 \pm 2.4$	$0.30 \pm 0.26$	$0.07 \pm 0.06$

Table A.4: NuTeV forward differential cross-section for  $\bar{\nu}_\mu N \rightarrow \mu^+ \mu^- X$  at  $E \sim 78.97$  GeV. The forward cross-section requires  $E_{\mu^-} \geq 5$  GeV, and the cross-section values should be multiplied by  $G_F^2 M E / \pi$ . The first error given for the cross-sections is statistical and the second systematic. Units are in GeV or  $\text{GeV}^2$ , where appropriate, for the averages of the kinematic quantities.

$\chi^2$	$\mathbf{x}$	$\mathbf{y}$	$\frac{d\sigma(\bar{\nu}_\mu N \rightarrow \mu^+ \mu^- X)}{dx dy} _+$	$\langle E_{HAD} \rangle$	$\langle E_{\mu^-} \rangle$	$\langle p_{T\mu^-}^2 \rangle$	$\langle p_{T\mu^-}^2 \rangle_{out}$
0.68	0.016	0.356	$0.793 \pm 0.171 \pm 0.017$	$32.7 \pm 2.5$	$12.7 \pm 2.0$	$0.50 \pm 0.62$	$0.78 \pm 1.84$
0.42	0.044	0.356	$0.744 \pm 0.172 \pm 0.024$	$36.0 \pm 3.3$	$12.2 \pm 2.0$	$0.23 \pm 0.12$	$0.08 \pm 0.06$
0.37	0.075	0.356	$0.752 \pm 0.174 \pm 0.013$	$33.5 \pm 2.9$	$11.2 \pm 1.6$	$0.33 \pm 0.11$	$0.21 \pm 0.36$
0.38	0.117	0.356	$0.427 \pm 0.097 \pm 0.009$	$36.7 \pm 3.7$	$10.2 \pm 1.4$	$0.73 \pm 0.27$	$0.07 \pm 0.06$
0.56	0.211	0.356	$0.140 \pm 0.030 \pm 0.003$	$38.4 \pm 4.1$	$8.8 \pm 0.8$	$0.61 \pm 0.22$	$0.06 \pm 0.05$
0.53	0.016	0.586	$1.338 \pm 0.317 \pm 0.025$	$58.5 \pm 3.0$	$16.4 \pm 2.2$	$0.09 \pm 0.07$	$0.07 \pm 0.04$
0.37	0.044	0.586	$0.930 \pm 0.223 \pm 0.048$	$66.3 \pm 4.4$	$13.2 \pm 2.5$	$0.12 \pm 0.09$	$0.09 \pm 0.12$
0.36	0.075	0.586	$0.744 \pm 0.173 \pm 0.017$	$60.1 \pm 4.5$	$16.7 \pm 2.5$	$0.27 \pm 0.13$	$0.08 \pm 0.08$
0.34	0.117	0.586	$0.653 \pm 0.159 \pm 0.005$	$64.0 \pm 3.9$	$14.7 \pm 2.9$	$0.38 \pm 0.18$	$0.08 \pm 0.07$
0.50	0.211	0.586	$0.257 \pm 0.063 \pm 0.006$	$59.8 \pm 4.6$	$14.4 \pm 3.2$	$0.69 \pm 0.32$	$0.05 \pm 0.04$
0.46	0.016	0.788	$0.915 \pm 0.198 \pm 0.013$	$82.9 \pm 5.1$	$18.0 \pm 3.4$	$0.12 \pm 0.09$	$0.09 \pm 0.14$
0.37	0.044	0.788	$1.106 \pm 0.240 \pm 0.042$	$84.3 \pm 6.4$	$22.0 \pm 4.1$	$0.30 \pm 0.18$	$0.09 \pm 0.07$
0.33	0.075	0.788	$0.775 \pm 0.172 \pm 0.041$	$87.2 \pm 5.8$	$18.4 \pm 4.6$	$0.23 \pm 0.31$	$0.07 \pm 0.05$
0.36	0.117	0.788	$0.547 \pm 0.121 \pm 0.015$	$88.1 \pm 6.5$	$15.7 \pm 4.6$	$0.17 \pm 0.11$	$0.06 \pm 0.06$
0.44	0.211	0.788	$0.297 \pm 0.075 \pm 0.004$	$78.7 \pm 5.6$	$17.3 \pm 3.6$	$0.31 \pm 0.13$	$0.07 \pm 0.04$

Table A.5: NuTeV forward differential cross-section for  $\bar{\nu}_\mu N \rightarrow \mu^+ \mu^- X$  at  $E \sim 146.06$  GeV. The forward cross-section requires  $E_{\mu^-} \geq 5$  GeV, and the cross-section values should be multiplied by  $G_F^2 M E / \pi$ . The first error given for the cross-sections is statistical and the second systematic. Units are in GeV or  $\text{GeV}^2$ , where appropriate, for the averages of the kinematic quantities.

$\chi^2$	$\mathbf{x}$	$\mathbf{y}$	$\frac{d\sigma(\bar{\nu}_\mu N \rightarrow \mu^+ \mu^- X)}{dx dy} _+$	$\langle E_{HAD} \rangle$	$\langle E_{\mu^-} \rangle$	$\langle p_{T\mu^-}^2 \rangle$	$\langle p_{T\mu^-}^2 \rangle$
0.80	0.016	0.356	$1.046 \pm 0.228 \pm 0.015$	$53.2 \pm 3.3$	$14.3 \pm 2.4$	$0.16 \pm 0.10$	$0.10 \pm 0.05$
0.51	0.044	0.356	$1.133 \pm 0.254 \pm 0.017$	$54.9 \pm 4.4$	$15.9 \pm 2.4$	$0.37 \pm 0.23$	$0.08 \pm 0.04$
0.41	0.075	0.356	$0.855 \pm 0.195 \pm 0.010$	$57.2 \pm 6.4$	$16.2 \pm 3.5$	$0.52 \pm 0.19$	$0.09 \pm 0.07$
0.44	0.117	0.356	$0.426 \pm 0.094 \pm 0.030$	$57.0 \pm 7.0$	$13.6 \pm 2.8$	$0.58 \pm 0.37$	$0.07 \pm 0.05$
0.60	0.211	0.356	$0.331 \pm 0.070 \pm 0.029$	$61.8 \pm 6.9$	$11.8 \pm 2.6$	$1.47 \pm 0.92$	$0.08 \pm 0.04$
0.60	0.016	0.586	$1.459 \pm 0.380 \pm 0.012$	$95.0 \pm 6.7$	$17.2 \pm 3.3$	$0.14 \pm 0.11$	$0.04 \pm 0.04$
0.45	0.044	0.586	$1.111 \pm 0.281 \pm 0.011$	$95.0 \pm 5.4$	$19.5 \pm 3.9$	$0.27 \pm 0.21$	$0.07 \pm 0.05$
0.41	0.075	0.586	$0.998 \pm 0.253 \pm 0.037$	$89.2 \pm 7.4$	$25.3 \pm 5.2$	$0.39 \pm 0.22$	$0.15 \pm 0.16$
0.42	0.117	0.586	$0.787 \pm 0.202 \pm 0.011$	$97.8 \pm 10.3$	$24.9 \pm 7.9$	$1.24 \pm 1.16$	$0.08 \pm 0.10$
0.56	0.211	0.586	$0.303 \pm 0.077 \pm 0.007$	$101.4 \pm 6.3$	$18.6 \pm 5.8$	$1.18 \pm 0.58$	$0.16 \pm 0.33$
0.59	0.016	0.788	$1.125 \pm 0.243 \pm 0.018$	$135.3 \pm 12.9$	$26.4 \pm 6.1$	$0.15 \pm 0.13$	$0.09 \pm 0.09$
0.46	0.044	0.788	$1.433 \pm 0.295 \pm 0.012$	$132.8 \pm 10.2$	$25.2 \pm 6.0$	$0.17 \pm 0.15$	$0.08 \pm 0.11$
0.41	0.075	0.788	$1.258 \pm 0.268 \pm 0.033$	$129.6 \pm 9.7$	$26.3 \pm 7.3$	$0.52 \pm 0.54$	$0.08 \pm 0.09$
0.44	0.117	0.788	$0.693 \pm 0.154 \pm 0.022$	$134.1 \pm 14.4$	$25.8 \pm 7.4$	$0.70 \pm 0.62$	$0.06 \pm 0.07$
0.58	0.211	0.788	$0.219 \pm 0.050 \pm 0.010$	$132.4 \pm 18.0$	$20.5 \pm 5.3$	$0.68 \pm 0.35$	$0.15 \pm 0.17$

Table A.6: NuTeV forward differential cross-section for  $\bar{\nu}_\mu N \rightarrow \mu^+ \mu^- X$  at  $E \sim 222.14$  GeV. The forward cross-section requires  $E_{\mu^-} \geq 5$  GeV, and the cross-section values should be multiplied by  $G_F^2 M E / \pi$ . The first error given for the cross-sections is statistical and the second systematic. Units are in GeV or  $\text{GeV}^2$ , where appropriate, for the averages of the kinematic quantities.

$\chi^2$	$\mathbf{x}$	$\mathbf{y}$	$\frac{d\sigma(\nu_\mu N \rightarrow \mu^- \mu^+ X)}{dx dy} _+$
0.53	0.023	0.320	$0.589 \pm 0.129 \pm 0.018$
0.47	0.057	0.320	$0.619 \pm 0.110 \pm 0.004$
0.44	0.100	0.320	$0.470 \pm 0.082 \pm 0.004$
0.46	0.167	0.320	$0.495 \pm 0.081 \pm 0.003$
0.69	0.336	0.320	$0.159 \pm 0.024 \pm 0.001$
0.59	0.023	0.570	$1.366 \pm 0.223 \pm 0.018$
0.43	0.057	0.570	$1.015 \pm 0.160 \pm 0.008$
0.50	0.100	0.570	$0.706 \pm 0.103 \pm 0.023$
0.52	0.167	0.570	$0.473 \pm 0.067 \pm 0.010$
0.61	0.336	0.570	$0.226 \pm 0.034 \pm 0.003$
0.42	0.023	0.795	$1.407 \pm 0.223 \pm 0.044$
0.39	0.057	0.795	$1.356 \pm 0.202 \pm 0.016$
0.46	0.100	0.795	$1.142 \pm 0.172 \pm 0.014$
0.48	0.167	0.795	$0.812 \pm 0.136 \pm 0.018$
0.49	0.336	0.795	$0.211 \pm 0.040 \pm 0.003$

Table A.7: CCFR E744/E770 forward differential cross-section for  $\nu_\mu N \rightarrow \mu^- \mu^+ X$  at  $E \sim 109.46$  GeV. The forward cross-section requires  $E_{\mu^+} \geq 5$  GeV, and the cross-section values should be multiplied by  $G_F^2 ME/\pi$ . The first error given for the cross-sections is statistical and the second systematic. Units are in GeV or GeV<sup>2</sup>, where appropriate, for the averages of the kinematic quantities.

$\chi^2$	<b>x</b>	<b>y</b>	$\frac{d\sigma(\nu_\mu N \rightarrow \mu^- \mu^+ X)}{dx dy} _+$
0.58	0.023	0.320	$1.327 \pm 0.233 \pm 0.005$
0.45	0.057	0.320	$1.160 \pm 0.192 \pm 0.036$
0.46	0.100	0.320	$0.931 \pm 0.147 \pm 0.005$
0.41	0.167	0.320	$0.567 \pm 0.090 \pm 0.003$
0.68	0.336	0.320	$0.254 \pm 0.038 \pm 0.004$
0.57	0.023	0.570	$1.571 \pm 0.247 \pm 0.007$
0.43	0.057	0.570	$1.673 \pm 0.274 \pm 0.013$
0.42	0.100	0.570	$1.381 \pm 0.226 \pm 0.007$
0.43	0.167	0.570	$0.912 \pm 0.150 \pm 0.009$
0.55	0.336	0.570	$0.261 \pm 0.043 \pm 0.002$
0.46	0.023	0.795	$1.636 \pm 0.243 \pm 0.028$
0.45	0.057	0.795	$1.582 \pm 0.241 \pm 0.010$
0.38	0.100	0.795	$1.092 \pm 0.181 \pm 0.004$
0.45	0.167	0.795	$0.814 \pm 0.134 \pm 0.003$
0.54	0.336	0.795	$0.230 \pm 0.041 \pm 0.003$

Table A.8: CCFR E744/E770 forward differential cross-section for  $\nu_\mu N \rightarrow \mu^- \mu^+ X$  at  $E \sim 209.89$  GeV. The forward cross-section requires  $E_{\mu^+} \geq 5$  GeV, and the cross-section values should be multiplied by  $G_F^2 M E / \pi$ . The first error given for the cross-sections is statistical and the second systematic. Units are in GeV or GeV<sup>2</sup>, where appropriate, for the averages of the kinematic quantities.

$\chi^2$	$\mathbf{x}$	$\mathbf{y}$	$\frac{d\sigma(\nu_\mu N \rightarrow \mu^- \mu^+ X)}{dx dy} _+$
0.85	0.023	0.320	$1.546 \pm 0.234 \pm 0.005$
0.53	0.057	0.320	$1.613 \pm 0.256 \pm 0.011$
0.53	0.100	0.320	$1.007 \pm 0.157 \pm 0.017$
0.50	0.167	0.320	$0.619 \pm 0.095 \pm 0.004$
0.71	0.336	0.320	$0.292 \pm 0.041 \pm 0.003$
0.68	0.023	0.570	$1.812 \pm 0.300 \pm 0.015$
0.50	0.057	0.570	$1.691 \pm 0.299 \pm 0.006$
0.50	0.100	0.570	$1.536 \pm 0.272 \pm 0.081$
0.49	0.167	0.570	$0.712 \pm 0.126 \pm 0.004$
0.66	0.336	0.570	$0.285 \pm 0.048 \pm 0.016$
0.72	0.023	0.795	$2.421 \pm 0.342 \pm 0.024$
0.56	0.057	0.795	$2.046 \pm 0.320 \pm 0.004$
0.54	0.100	0.795	$1.688 \pm 0.285 \pm 0.005$
0.58	0.167	0.795	$0.948 \pm 0.159 \pm 0.002$
0.76	0.336	0.795	$0.328 \pm 0.060 \pm 0.002$

Table A.9: CCFR E744/E770 forward differential cross-section for  $\nu_\mu N \rightarrow \mu^- \mu^+ X$  at  $E \sim 332.70$  GeV. The forward cross-section requires  $E_{\mu^+} \geq 5$  GeV, and the cross-section values should be multiplied by  $G_F^2 ME/\pi$ . The first error given for the cross-sections is statistical and the second systematic. Units are in GeV or GeV<sup>2</sup>, where appropriate, for the averages of the kinematic quantities.



$\chi^2$	$\mathbf{x}$	$\mathbf{y}$	$\frac{d\sigma(\bar{\nu}_\mu N \rightarrow \mu^+ \mu^- X)}{dx dy} _+$
0.40	0.017	0.356	$0.332 \pm 0.153 \pm 0.073$
0.43	0.040	0.356	$0.483 \pm 0.182 \pm 0.027$
0.38	0.068	0.356	$0.484 \pm 0.171 \pm 0.009$
0.40	0.109	0.356	$0.342 \pm 0.121 \pm 0.150$
0.60	0.206	0.356	$0.140 \pm 0.047 \pm 0.001$
0.24	0.017	0.596	$1.171 \pm 0.390 \pm 0.062$
0.28	0.040	0.596	$1.152 \pm 0.369 \pm 0.032$
0.31	0.068	0.596	$0.660 \pm 0.206 \pm 0.021$
0.33	0.109	0.596	$0.684 \pm 0.219 \pm 0.065$
0.48	0.206	0.596	$0.173 \pm 0.056 \pm 0.004$
0.10	0.017	0.803	$1.165 \pm 0.416 \pm 0.117$
0.15	0.040	0.803	$0.928 \pm 0.313 \pm 0.073$
0.17	0.068	0.803	$0.974 \pm 0.344 \pm 0.055$
0.31	0.109	0.803	$0.912 \pm 0.311 \pm 0.033$
0.45	0.206	0.803	$0.305 \pm 0.118 \pm 0.005$

Table A.10: CCFR E744/E770 forward differential cross-section for  $\bar{\nu}_\mu N \rightarrow \mu^+ \mu^- X$  at  $E \sim 87.48$  GeV. The forward cross-section requires  $E_{\mu^-} \geq 5$  GeV, and the cross-section values should be multiplied by  $G_F^2 ME/\pi$ . The first error given for the cross-sections is statistical and the second systematic. Units are in GeV or  $\text{GeV}^2$ , where appropriate, for the averages of the kinematic quantities.

$\chi^2$	<b>x</b>	<b>y</b>	$\frac{d\sigma(\bar{\nu}_\mu N \rightarrow \mu^+ \mu^- X)}{dx dy} _+$
0.31	0.017	0.356	$1.010 \pm 0.396 \pm 0.031$
0.46	0.040	0.356	$1.190 \pm 0.415 \pm 0.076$
0.38	0.068	0.356	$0.867 \pm 0.304 \pm 0.030$
0.41	0.109	0.356	$0.609 \pm 0.206 \pm 0.004$
0.57	0.206	0.356	$0.228 \pm 0.074 \pm 0.013$
0.24	0.017	0.596	$1.592 \pm 0.566 \pm 0.092$
0.35	0.040	0.596	$1.521 \pm 0.529 \pm 0.085$
0.33	0.068	0.596	$1.144 \pm 0.406 \pm 0.053$
0.37	0.109	0.596	$0.640 \pm 0.227 \pm 0.007$
0.51	0.206	0.596	$0.219 \pm 0.075 \pm 0.001$
0.11	0.017	0.803	$1.827 \pm 0.577 \pm 0.186$
0.15	0.040	0.803	$1.734 \pm 0.594 \pm 0.131$
0.29	0.068	0.803	$1.819 \pm 0.604 \pm 0.064$
0.27	0.109	0.803	$0.789 \pm 0.275 \pm 0.025$
0.33	0.206	0.803	$0.225 \pm 0.082 \pm 0.004$

Table A.11: CCFR E744/E770 forward differential cross-section for  $\bar{\nu}_\mu N \rightarrow \mu^+ \mu^- X$  at  $E \sim 160.70$  GeV. The forward cross-section requires  $E_{\mu^-} \geq 5$  GeV, and the cross-section values should be multiplied by  $G_F^2 ME/\pi$ . The first error given for the cross-sections is statistical and the second systematic. Units are in GeV or GeV<sup>2</sup>, where appropriate, for the averages of the kinematic quantities.

$\chi^2$	$\mathbf{x}$	$\mathbf{y}$	$\frac{d\sigma(\bar{\nu}_\mu N \rightarrow \mu^+ \mu^- X)}{dx dy} _+$
0.69	0.017	0.356	$2.295 \pm 0.734 \pm 0.007$
0.55	0.040	0.356	$1.324 \pm 0.452 \pm 0.014$
0.54	0.068	0.356	$1.375 \pm 0.443 \pm 0.008$
0.47	0.109	0.356	$0.619 \pm 0.201 \pm 0.005$
0.68	0.206	0.356	$0.161 \pm 0.051 \pm 0.012$
0.44	0.017	0.596	$2.844 \pm 1.018 \pm 0.102$
0.44	0.040	0.596	$1.847 \pm 0.677 \pm 0.021$
0.40	0.068	0.596	$1.249 \pm 0.479 \pm 0.011$
0.44	0.109	0.596	$1.012 \pm 0.391 \pm 0.003$
0.60	0.206	0.596	$0.262 \pm 0.097 \pm 0.001$
0.16	0.017	0.803	$2.539 \pm 0.749 \pm 0.220$
0.26	0.040	0.803	$1.517 \pm 0.519 \pm 0.060$
0.38	0.068	0.803	$0.792 \pm 0.297 \pm 0.039$
0.49	0.109	0.803	$0.569 \pm 0.205 \pm 0.019$
0.68	0.206	0.803	$0.275 \pm 0.104 \pm 0.001$

Table A.12: CCFR E744/E770 forward differential cross-section for  $\bar{\nu}_\mu N \rightarrow \mu^+ \mu^- X$  at  $E \sim 265.82$  GeV. The forward cross-section requires  $E_{\mu^-} \geq 5$  GeV, and the cross-section values should be multiplied by  $G_F^2 M E / \pi$ . The first error given for the cross-sections is statistical and the second systematic. Units are in GeV or GeV<sup>2</sup>, where appropriate, for the averages of the kinematic quantities.

# Bibliography

- [1] D. Halzen and Martin, *Quarks & leptons: An Introductory Course in Modern Particle Physics*(New York: Wiley, 1984).
- [2] S.L. Glashow, J. Iliopoulos, L. Maiani, Phys. Rev. D**2**, 1285 (1970).
- [3] R. Brock *et al.* [CTEQ Collaboration], Rev. Mod. Phys. **67**, 157 (1995).
- [4] D. Griffiths, *Introducton to Elementary Particles*(New York: Wiley, 1987).
- [5] S. Weinberg, Phys. Rev. Lett. **19**, 1264 (1967).
- [6] S.L. Glashow, Nucl. Phys. **22**, 579 (1961).
- [7] C. Caso *et al.*, Eur. Phys. J. **C3**, 1 (1998).
- [8] J. M. Conrad, M. H. Shaevitz and T. Bolton, Rev. Mod. Phys. **70**, 1341 (1998).
- [9] M.A.G. Aivazis, F.I. Olness and W.-K. Tung, 1994, Phys. Rev. **D50**, 3085;  
M.A.G. Aivazis, J.C. Collins, F.I. Olness and W.-K. Tung, 1994, Phys. Rev. **D50** 3102.
- [10] M. Gluck, S. Kretzer, and E. Reya, Phys. Lett. B **380**, 171 (1997); *erratum*  
*ibid* B **405**, 391 (1997).
- [11] A.D. Martin, et al., Eur. Phys. J. C**2**, 287 (1998).
- [12] A. Chuvakin, J. Smith, and W.L. van Neerven, Phys. Rev. **D61**, 096004 (2000).

- [13] V. Barone, *et al.*, Phys. Lett. **B328**, 143 (1994).
- [14] V. Barone, C. Pascaud, and F. Zomer, Eur. Phys. J. C **12**, 243 (2000).
- [15] R. Demina, *et al.*, Phys. Rev. **D62**, 035011 (2000).
- [16] S. J. Brodsky and B. Ma, Phys. Lett. **B 381**, (317) (1996).
- [17] T. Sjostrand, Comput.Phys.Commun.**82**, 74 (1994).
- [18] N. Ushida, *et al.* (E531 Collab.), Phys. Lett. **B206**, 375; *ibid*, **B206**, 380.
- [19] T. Bolton, 1997, “Determining the CKM Parameters  $V_{cd}$  from  $\nu N$  Charm Production”, KSU-HEP-97-04, e-print hep-ex/9708014 (August, 1997).
- [20] D.E. Groom, *et al.*, Eur. Phys. Jour. **C 15**, 110 (2000).
- [21] A. O. Bazarko *et al.* (CCFR Collaboration), Z. Phys. **C 65**, 189 (1995).
- [22] S.A. Rabinowitz, *et al.* (CCFR Collaboration), Phys. Rev. Lett. **70**, 134 (1993).
- [23] H. Abramowicz, *et al.* (CDHS Collaboration), Z. Phys. **C15**, 19 (1982).
- [24] P. Vilain, *et al.* (CHARM II Collaboration), Eur.Phys.J.**C11**,19 (1999).
- [25] P. Astier, *et al.* (NOMAD Collaboration), Phys. Lett. **B 486**, 35 (2000).
- [26] P. Collins and T. Spiller, J. Phys. **G11**, 1289 (1985).
- [27] C. Peterson, *et al.* , Phys. Rev. **D27**, 105 (1983).
- [28] A. Alton, *et al.* (NuTeV Collaboration), “Search for Light-to-Heavy Quark Flavor Changing Neutral Currents in  $\nu_\mu N$  and  $\bar{\nu}_\mu N$  Scattering at the Tevatron”, Kansas State University Preprint KSU-HEP-00-001 , electronic e-print hep-ex/0007059, *to be published in Phys. Rev. D* (July 31, 2000).
- [29] D. A. Harris *et al.* (NuTeV Collaboration), Nucl. Instrum. Meth. **A447**, 377 (2000).

- [30] R. Brun, *et al.*, “GEANT Detector Description and Simulation Library” ,  
CERN computing document CERN CN/ASD(1998).
- [31] D. Yu. Bardin and O.M. Fedorenko, 1979, Sov. J. Nucl. Phys. **30**, 418.
- [32] G. Ingelman, A. Edin, and J. Rathsman, Comput.Phys.Commun.**101**, 108  
(1997).
- [33] P. Sandler, “Neutrino Production of Same-Sign Dimuons at the Fermilab  
Tevatron,” Ph.D. Thesis, Univ. of Wisconsin, 1992.
- [34] D. C. Carey, Karl L. Brown , and F.C. Iselin, “Decay Turtle...”, Fermilab  
Preprint FERMILAB-PM-31 (1982).
- [35] H. W. Atherton *et al.*, “Precise Measurements Of Particle Production By  
400-Gev/C Protons On Beryllium Targets,” CERN preprint CERN-80-07  
(1980).
- [36] A.J. Malensek, “Empirical Formula For Thick Target Particle Production,”  
Fermilab preprint FERMILAB-FN-0341.
- [37] M. Gluck, E. Reya and A. Vogt, Z. Phys. **C67**, 433 (1995).
- [38] H.L. Lai et al. (CTEQ Collaboration), Eur. Phys. J. **C12**, 375 (2000).
- [39] H. Plochow-Besch, Comput. Phys. Commun. **75**, 396 (1993).
- [40] A. J. Buras and K. J. F. Gaemers, Nucl. Phys. **B132**, 259 (1978).
- [41] L.W. Whitlow, *et al.*, Phys. Lett. **B282**, 475 (1992).
- [42] Published in In \*Montauk 1999, Colliders and collider physics at the highest  
energies\* 142-164, e-Print Archive: hep-ex/0005007.
- [43] M. Goncharov, *et al.* (NuTeV Collaboration), “Precise Measurement of  
Dimuon Production Cross-Sections in  $\nu_\mu$ Fe and  $\bar{\nu}_\mu$ Fe Deep Inelastic Scatter-  
ing at the Tevatron”, Kansas State University Preprint KSU-HEP-01-001,  
electronic e-print hep-ex/0102049, *to be published in Phys. Rev. D*.